

# Assessment of ocular aberrations at scaled pupil size and reduced Shack-Hartmann spot number

by

Abbas Ommani

A thesis  
presented to the University of Waterloo  
in fulfillment of the  
thesis requirement for the degree of  
Doctor of Philosophy  
in  
Vision Science

Waterloo, Ontario, Canada, 2019

© Abbas Ommani 2019

## Examining Committee Membership

The following served on the Examining Committee for this thesis. The decision of the Examining Committee is by majority vote.

External Examiner            Dr. A. R. Ganesan  
Professor, Indian Institute of Technology Madras

Supervisor(s)                Dr. Vasudevan Lakshminarayanan  
Professor, University of Waterloo

Dr. Natalie Hutchings  
Associate Professor, University of Waterloo

Internal Member             Dr. William Bobier  
Professor Emeritus, University of Waterloo

Dr. Kaamran Raahemifar  
Professor, Ryerson University

Internal-external Member    Dr. Simarjeet Saini  
Associate Professor, University of Waterloo

## **Author's Declaration**

I hereby declare that I am the sole author of this thesis. This is a true copy of the thesis, including any required final revisions, as accepted by my examiners.

I understand that my thesis may be made electronically available to the public.

## **Abstract**

Wavefront aberrations describe the optical imperfections of the eye by measuring the complete refractive elements of the eye. However, the reliability of ocular aberration is uncertain under some challenges and issues. Ocular aberration is generally described in terms of Zernike polynomials. However, the Zernike polynomials are pupil size dependent, therefore, the aberration measured at a fixed pupil size cannot be used for another pupil size. One solution to this problem is to use pupil size scaling technique to scale up or down the aberration to a required pupil size; however, the validity of these techniques for clinical data is not available. To tackle this issue, validation of mathematical pupil size scaling formula by comparing the estimates of the Zernike coefficients with corresponding clinical measurements obtained at different pupil sizes is performed. The results show that the estimation of ocular wavefront aberration coefficients either scaling down from large to smaller pupils or scaling up from smaller to large pupils provides estimates that are not significantly different from clinically measured values. However, when scaling up to a larger pupil size, the estimates are more variable. These findings have implications for pupil scaling on an individual basis, such as in cases of refractive surgery or when using pupil scaling to examine a clinical cohort. Another challenge of an ocular aberration for clinical uses is when the spots on the Shack-Hartmann (SH) are missed due to the opacity of eye parameters or some other disease conditions. This issue is addressed by randomly deleting the number of spots from the SH images and comparing the results with the aberration of the original SH image without the missing spots. The results indicate that as high as 50 % of the SH spots can be deleted without affecting the estimation of spherical defocus within typical

clinically acceptable limits of  $\pm 0.25D$ . The results are further examined with in vivo measurements of a human eye wearing a spectacle lens with various models of clustered missing spots to simulate loss that might occur with the disease. The findings of this study provide foundational data on measuring the ocular wavefront aberration when only a reduced number of SH spots are available.

## **Acknowledgments**

I wish to express my sincere gratitude to my supervisors; Prof. Vasudevan Lakshminarayanan and Dr. Natalie Hutchings for their support, guidance, encouragement and valuable suggestions that helped me in all aspects to complete this thesis work successfully.

I would like to thank my committee members Dr. William Bobier and Dr. Simarjeet Saini for their help and advice I would also like to thank Dr. Trefford Simpson and Dr. Chris Hudson and Dr. Jeff Hovis for their assistance and valuable comments.

I would like to thank Dr. Damber Thapa for providing precious suggestions and help whenever needed. Many thanks to Dr. Luis Diaz Santana for his kind and valuable help and Professor David Edgar for his support when I was at City University London and after that.

Special thanks to Rithambar Burman, Chandrahas Thatiparthi and Varadarajan Jayakumar for their help. I would also like to thanks all my friends for their help, motivation, and advice whenever desired. I would like to thank the graduate officers, graduate coordinators, staff and faculty of the School of Optometry & Vision Science, and all the graduate students for making my stay nice and enjoyable.

Many thanks to HOYA Canada Inc. for providing the iProfilor Zeiss. This study was partly funded by Canadian Optometric Education Trust Funds (COETF).

Last, but not least, I would like to express my deep sense of gratitude to my family, my parents all my family members especially my lovely daughter for her love and support.

## **Dedication**

To My Family

If someone feels that, they had never made a mistake in their life

then it means they had never tried a new thing in their life.

EINSTEIN

## Table of Contents

Examining Committee Membership .....	ii
Author's Declaration .....	iii
Abstract .....	iv
Acknowledgments .....	vi
Dedication .....	vii
Table of Contents .....	viii
List of Figures .....	x
List of Tables .....	xvii
List of Abbreviations .....	xviii
Chapter 1 Introduction .....	1
1.1 Optics of the human eye .....	1
1.2 Optical imperfections of the human eye .....	7
1.2.1 Ametropia .....	7
1.2.2 Higher-order aberrations .....	9
1.3 Higher-order aberration measurement .....	11
1.4 Contribution of the thesis .....	17
1.5 Organization of the thesis .....	19
Chapter 2 Construction and calibration of the custom-made Shack-Hartmann aberrometer .....	21
2.1 Introduction .....	21
2.2 Aberrometer design .....	21
2.3 Alignment procedure .....	24
2.4 Analysis software .....	26
2.5 Calibration .....	33
2.6 Safety .....	37
Chapter 3 Comparison of centroid estimation methods for wavefront aberration measurement .....	40
3.1 Introduction .....	40
3.2 Methods .....	41
3.2.1 Brightest spot center (BSC) .....	41
3.2.2 Center of mass/gravity .....	41
3.2.3 Weighted center of gravity (WCoG) .....	42
3.2.4 Intensity-weighted center of gravity (ICoG) .....	42



3.3 Shack-Hartmann image collections .....	43
3.4 Results.....	44
3.5 Conclusions.....	52
Chapter 4 Pupil scaling for the estimation of aberration in natural pupils .....	54
4.1 Introduction.....	54
4.2 Methods .....	55
4.3 Results.....	59
4.4 Discussion and conclusion.....	65
Chapter 5 Wavefront aberration with missing Shack-Hartmann Spots.....	69
5.1 Introduction.....	69
5.2 Methods .....	70
5.2.1 Missing spots in a model eye.....	70
5.2.2 Ocular aberrations with a cluster of missing spots in a human eye.....	72
5.3 Results.....	85
5.3.1 Missing spots in a model eye.....	85
5.3.2 Ocular aberrations with clusters of missing spots in a human eye .....	93
5.4 Conclusion .....	106
Chapter 6 Conclusion and future direction.....	110
6.1 Summary of the dissertation .....	110
6.2 Future directions .....	114
Appendix.....	116
Bibliography .....	122

## List of Figures

**Figure 1.1.** A schematic diagram of the human eye.

**Figure 1.2.** Illustration of the anatomy of the eye. Reproduced with permission from [20].

**Figure 1.3.** Absorption curves for the three cones types and rods. Adapted from [22].

**Figure 1.4.** Diagram showing refractive conditions (a) emmetropia (b) hyperopia and (a) myopia.

**Figure 1.5.** Distortions to a wavefront from a human eye.

**Figure 1.6.** SH wavefront sensor layout

**Figure 1.7.** Displacement caused by an aberrated wavefront. Orthogonal view (Left) and transverse view (right). Blue dots and red dots in the transverse view the centroids of the perfect and aberrated wavefront

**Figure 1.8.** Zernike polynomials up to 5th order plotted on a unit circle. Reproduced with permission from [35].

**Figure 2.1.** Figure 2.1. Schematic illustration of the optical setup: LD = laser diode; MO = microscope objective; PH = pinhole; L1, L2, and L3 = lenses; M1, M2, and M3 = mirrors; M4 = removable mirror used for calibration; BM = beam splitter; HM = hot mirror; SHS = SH system.

**Figure 2.2.** The SH wavefront aberrometer. The components, as described in the text, are: laser diode (LD), microscope objective (MO), pinhole (PH), beam splitter (BS), hot mirror (HM), relay lenses (L2+L3), mirror (M1, M2, M3, M4) and Shack-Hartmann sensor (SHS).

**Figure 2.3.** A flowchart illustrating the steps performed to calculate Zernike coefficients from raw SH images.

**Figure 2.4.** (a) Original RGB image obtained by the scanner (b) corresponding black and white image of (a). (c) Centroids of spots calculated from (b). (d) A circular image extracted from the geometrical center of the image.

**Figure 2.5.** SH spot pattern showing the adaptive window around each spot used to determine the centroid of the spot.

**Figure 2.6.** Snapshot of the results of the software showing Zernike coefficients from 1<sup>st</sup> to 5<sup>th</sup> order and spherical dioptric power calculated from the 5<sup>th</sup> Zernike term ( $Z_2^0$ ). A trial lens having power +2.0 D was placed in front of the model eye to record these data.

**Figure 2.7.** Setup of the model eye of calibration of the analysis software.

**Figure 2.8.** Plots of spherical power estimated from the SH image against the actual power of the trial lens inserted in front of the model eye.

**Figure 2.9.** The head of the spectrometer is held at the focal point of the retina of the model eye.

**Figure 2.10.** Screenshot showing the peak of the light source and measured absolute irradiance of  $452\mu\text{W}/\text{cm}^2$ .

**Figure 3.1.** Plots of the estimated spherical defocus with respect to the actual defocus calculated by using BSC, CoM, ICoG and WCoG centroid estimation methods, respectively, on raw images without applying pre-processing steps.

**Figure 3.2.** Linear plots between estimated spherical defocus and actual defocus calculated by using BSC, CoM, ICoG, and WCoG centroid estimation methods, respectively, on raw images without applying pre-processing steps. The dotted line shows the expected spherical defocus values with respect to the actual defocus values.

**Figure 3.3.** Plots of the estimated spherical defocus with respect to the actual defocus obtained from centroid estimation methods, BSC, CoM, ICoG, and WCoG, respectively, after applying pre-processing steps to raw images.

**Figure 3.4.** Linear plots between estimated spherical defocus and actual defocus calculated by using BSC, CoM, ICoG, and WCoG centroid estimation methods, respectively, after applying pre-processing methods to raw images. The dotted line shows the expected spherical defocus values with respect to the actual defocus.

**Figure 4.1.** The error between the measured and estimated 2<sup>nd</sup> order Zernike coefficients  $C_2^{-2}$  (top),  $C_2^2$  (middle) and  $C_2^0$  (bottom) for the pupil scaling procedures where data were scaled up from the measured 3mm data to the maximum pupil diameter (left panel) and scaled down from the maximum pupil size data to a 3mm pupil diameter (right panel). The dotted ellipse illustrates a robust 95% confidence interval for the data. Open symbols represent maximum pupil size <5.40mm and filled symbols represent pupil sizes >5.40mm. The dotted ellipse illustrates a robust 95% confidence interval for the data. Note the different scales for the ordinate axes of each panel and the abscissa for the bottom graphs.

**Figure 4.2.** The error between the measured and estimated 3<sup>rd</sup> order Zernike coefficients  $C_3^{-3}$  (top),  $C_3^{-1}$  (upper middle),  $C_3^1$  (lower middle) and  $C_3^3$  (bottom) for the pupil scaling procedures where data were scaled up from the measured 3mm data to the maximum pupil diameter (left panel) and scaled down from the maximum pupil size data to a 3mm pupil diameter (right panel). Other details are as for Figure 4.1.

**Figure 4.3.** The error between the measured and estimated 4<sup>th</sup> order Zernike coefficients  $C_4^{-4}$  (top),  $C_4^{-2}$  (2<sup>nd</sup> row),  $C_4^0$  (3<sup>rd</sup> row),  $C_4^2$  (4<sup>th</sup> row) and  $C_4^4$  (bottom) for the pupil scaling procedures where data

were scaled up from the measured 3mm data to the maximum pupil diameter (left panel) and scaled down from the maximum pupil size data to a 3mm pupil diameter (right panel). Other details are as for Figure 4.1.

**Figure 5.1.** Surface plot created from the aberration of the model eye when trial lenses of power -3.5D to 3.5D in the increment of 0.5D is inserted in front of the model eye.

**Figure 5.2.** Patches of transparent Sellotape<sup>TM</sup> on the Plano glass to create disease models.

**Figure 5.3.** A schematic of different visual fields of the right eye.

**Figure 5.4.** SH spot array pattern of the normal image, less than 1% of spots missing. It was taken with the spectacle glass and no tape.

**Figure 5.5.** SH spot array pattern of model 1 with 3% of SH spots missing. Tape position was on the temporal side.

**Figure 5.6.** SH spot array pattern of model 2 with 3.1 % of SH spots missing. The tape was positioned on the inferior side.

**Figure 5.7.** SH spot array pattern of model 3 with 3.16% of SH spots missing. The tape was positioned on the superior side.

**Figure 5.8.** SH spot array pattern of model 4 with 4.06% of SH spots missing. The tape was positioned on the superior side.

**Figure 5.9.** SH spot array pattern of model 5 with 5.55% of SH spots missing. The tape was position on the superior temporal side.

**Figure 5.10.** SH spot array pattern of model 6 with 6.17% of SH spots missing. The tape was position on the temporal side.

**Figure 5.11.** SH spot array pattern of model 7 with 8.5% of SH spots missing. The tape was positioned on the central superior side.

**Figure 5.12.** SH spot array pattern of model 8 with 8.66% of SH spots missing. The tape was position on the on the central inferior side.

**Figure 5.13.** SH spot array pattern of model 9 with 9.6% of SH spots missing. The tape was positioned on the central temporal side.

**Figure 5.14.** SH spot array pattern of model 10 with 14.9% of SH spots missing. The tape was positioned on the superior temporal side.

**Figure 5.15.** SH spot array pattern of model 11 with 16.54% of SH spots missing. The tape was position on the temporal and nasal sides.

**Figure 5.16.** SH spot array pattern of model 12 with 20.3% of SH spots missing. The tape was positioned on the central temporal side.

**Figure 5.17.** SH spot array pattern of model 13 with 23.32% of SH spots missing. The tape was positioned on the superior temporal side.

**Figure 5.18.** SH spot array pattern of model 14 with 31.5% of SH spots missing. The tape was positioned on the central inferior side.

**Figure 5.19.** Estimated defocus vs actual defocus at different percentage of data deletions from 0 to 60%. The red solid line is the reference line for estimated defocus.

**Figure 1.20.** Best fit lines between Trefoil  $Z_3^{-3}$  and percentage of SH spots deleted at a different level of data deletions from -3.0 D to + 3.0D in the interval of 1.0D.

**Figure 5.21.** Best fit lines between Coma and percentage of SH spots deleted at a different level of data deletions from -3.0 D to + 3.0D in the interval of 1.0D.

**Figure 5.22.** Best fit lines between Spherical aberration and percentage of SH spots deleted at a different level of data deletions from -3.0 D to + 3.0D in the interval of 1.0D.

**Figure 5.23.** Best fit lines between higher order aberration (3<sup>rd</sup> to 5<sup>th</sup> order) and percentage of SH spots deleted at a different level of data deletions from -3.0 D to + 3.0D in the interval of 1.0D.

**Figure 5.24.** Linear regression (red line) between the 2<sup>nd</sup> order Zernike coefficients  $Z_2^{-2}$  and percentage of SH spots deleted. The dotted blue lines illustrate 95% confidence interval for the data.

**Figure 5.25.** Linear regression (red line) between the 2<sup>nd</sup> order Zernike coefficients  $Z_2^0$  and percentage of SH spots deleted. The dotted blue lines illustrate 95% confidence interval for the data.

**Figure 5.26.** Linear regression (red line) between the 2<sup>nd</sup> order Zernike coefficients  $Z_2^2$  and percentage of SH spots deleted. The dotted blue lines illustrate 95% confidence interval for the data.

**Figure 5.27.** Linear regression (red line) between the 3<sup>rd</sup> order Zernike coefficients  $Z_3^{-3}$  (vertical trefoil) and percentage of SH spots deleted. The dotted blue lines illustrate 95% confidence interval for the data.

**Figure 5.28.** Linear regression (red line) between the 3<sup>rd</sup> order Zernike coefficients  $Z_3^3$  (horizontal trefoil) and percentage of SH spots deleted. The dotted blue lines illustrate 95% confidence interval for the data.

**Figure 5.29.** Linear regression (red line) between the 3<sup>rd</sup> order Zernike coefficients  $Z_3^{-1}$  (vertical coma) and percentage of SH spots deleted. The dotted blue lines illustrate 95% confidence interval for the data.

**Figure 5.30.** Linear regression (red line) between the 3<sup>rd</sup> order Zernike coefficients  $Z_3^1$  (horizontal coma) and percentage of SH spots deleted. The dotted blue lines illustrate 95% confidence interval for the data.

**Figure 5.31.** Linear regression (red line) between the 4<sup>th</sup> order Zernike coefficients  $Z_4^0$  (spherical aberration) and percentage of SH spots deleted. The dotted blue lines illustrate 95% confidence interval for the data.

**Figure 5.32.** Linear regression (red line) between the higher order aberration (HOA) from 3<sup>rd</sup> to 5<sup>th</sup> order and percentage of SH spots deleted. The dotted blue lines illustrate 95% confidence interval for the data.

**Figure 5.33.** Linear regression (red line) between the total aberration (TA) from 2<sup>nd</sup> to 5<sup>th</sup> order and percentage of SH spots deleted. The dotted blue lines illustrate 95% confidence interval for the data.



## List of Tables

**Table 1.1.** A list of Zernike polynomials up to 5<sup>th</sup> order (J=mode, n=order, m=frequency).

**Table 2.1.** Comparison of different centroid estimation method without the pre-processing methods. The absolute errors were calculated by subtracting the estimated defocus from the actual defocus.

**Table 3.2.** Comparison of different centroid estimation method with the pre-processing method. The absolute errors were calculated by subtracting the estimated defocus from the actual defocus.

**Table 3.3.** Parameters of the linear fits in figure 3.1.

**Table 3.4.** Parameters of the linear fits in figure 3.2.

**Table 4.1.** Mean error and limits of agreement for the difference between the estimated and measured coefficients for each pupil scaling procedure.

**Table 5.1.** Fourteen disease models created by putting a tape on the glass.

**Table 5.2.** Spherical defocus estimated from the SH images from 0 – 70% deletion at different defocus conditions from -3.5D to +3.5D, in 0.5D increments. The program randomly deleted the SH spots in 1000 times creating different patterns at each time. Average spherical defocus ( $\pm$  standard deviation) was calculated from the 1000 simulations.

**Table 5.3a.** Zernike coefficients from 2<sup>nd</sup> to 5<sup>th</sup> order aberrations extracted from the SH images of normal (without missing spots) and missing spot models 1 to 7.

**Table 5.3b.** Zernike coefficients from 2<sup>nd</sup> to 5<sup>th</sup> order aberrations extracted from the SH images of normal (without missing spots) and missing spot models 8 to 14.

## List of Abbreviations

D	Diopter
SH	Shack-Hartmann
CCD	Charged Coupled Device
RMS	Root-Mean-Square
HOA	Higher Order Aberrations
LD	Laser Diode
VDC	Volts Direct Current
MO	Microscope Objective
PH	Pinhole
ARB	Broadband Anti-Reflective
VIS	Visible Spectrum
I	Iris
OD	Oculus Dexter (Right Eye)
OS	Oculus Sinister (Left Eye)
SNR	Signal to Noise Ratio
BS	Beam Splitter
HM	Hot Mirror
RBG	Red, Blue, Green
CoM	Center of Mass
ICoG	Intensity Weighted Center of Gravity
WcoG	Weighted Center of Gravity
BSC	Brightest Spot Centroid
ANOVA	Analysis of Variance

# Chapter 1

## Introduction

### 1.1 Optics of the human eye

The human eye is an extremely complicated and interrelated system, composed of both optical and neural components. However, its unique autofocusing system and sensitivity to the low amount of light outperform the best man-made cameras so far. The optical parts of the eye consist of the cornea, the aqueous humour, the iris, the crystalline lens, the vitreous humour, and the retina and a simple schematic of the human eye is shown in Figure 1.1. Light incident on the eye is refracted mostly by the cornea and crystalline lens and forms an image on the retina. The cornea is a transparent, aspheric meniscus surface which has an average central thickness of  $\sim 500 \mu\text{m}$  [1]. The cornea is covered by the tear film that acts as a lubricant and is essential for maintaining the corneal integrity and transparency [2-3]. The tear film is the most immediate refractive element of the cornea encountered by the external rays of light [4-5] and its primary optical function is covering the cornea to create a smooth optical surface [6]. The tear film and cornea together contribute more than two-thirds of the total refractive power of the eye and hence is responsible for most of the refraction of light [2]. The cornea is not perfectly spherical, as it is flatter at the peripheral region as compared to the central region. Also, the horizontal and vertical curvatures of the cornea may not be equal giving rise to astigmatism.

The chamber located immediately behind the cornea, with a depth of approximately 3.0 mm, is called the anterior chamber. It is filled with a colorless liquid called the aqueous humour, which brings nutrients to the anterior ocular structures and takes away metabolic

waste. The refractive index of aqueous humour is 1.336, which is very similar to that of the cornea (1.376) [2]. The anterior chamber depth plays an important role in the optics of the eye, as it affects the total power of the eye's optical system. A reduction of 1 mm in the depth of the anterior chamber would increase the eye's total power by about 1.4 D [7-9]. The ciliary body is responsible for the formation of aqueous humour through a complex mechanism consisting of plasma filtration, active transport, and secretion. Secreted aqueous humour flows toward the anterior chamber passing through the pupil and finally drains in the Canal of Schlemm. The intraocular pressure and, accordingly, the shape of the eyes are dependent on the amount of aqueous humour present in the anterior chamber [6].

The iris of the eye creates a variable aperture for the ocular optics and can be easily identified by its characteristic colors such as blue, green, brown, etc. The pupil is the approximately circular aperture at the center of the iris, regulating the amount of light reaching the posterior sections of the eye. In the human eye, the pupil size can vary from about 2 mm to 8 mm and the size is modulated by two antagonistic muscles that are under reflex rather than voluntary control [6]. The pupils of both eyes directly respond to a change in luminance. If only one pupil is exposed to light, then the unexposed pupil will also react to the change through a consensual reflex. Moreover, the pupils respond to near fixation of a target with pupillary constriction [8]. Anomaly or failure of any of these reflexes can represent a primary or underlying disorder. The pupil can be artificially dilated with the installation of mydriatic medications, such as Tropicamide. A detailed discussion of the various factors affecting pupil size can be found in the literature [10]. The quality of the images obtained in the eye is associated with the pupil in two ways. First, the pupil helps to

exclude the peripheral incident rays on the cornea from forming part of the retinal image, thus reducing peripheral aberrations. Second, the pupil size influences the depth of field of the eye in which, for a fixed amount of accommodation, a clear image is formed on the retina for a range of object distances. A pupil size smaller than 2mm can adversely affect the quality of the image by increasing the amount of diffraction [11]. Visual acuity is limited by diffraction according to Rayleigh’s criterion, which mathematically describes the minimum distance between two spots in object space that would be detected as separate by the eye.

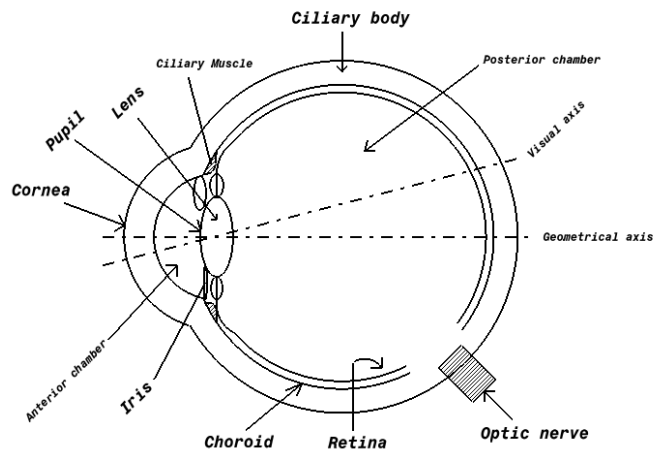


Figure 1.1. A schematic diagram of the human eye.

The crystalline lens is an “onion-like” multilayered structure confined to a capsule and is attached to the ciliary body of the eye by zonules. It is completely avascular. The average radius-of-curvature of the anterior surface of the lens is 12 mm and the radius of curvature of the posterior surface is 5 mm in the non-accommodated state [12]. In a young adult, the (non-accommodated) lens has an average thickness of 3.6 mm at the apex [13]. The lens also has a gradient refractive index where the refractive index of the nucleus (~1.41) is higher than that

of the outermost layers ( $\sim 1.38$ ) [7, 14-16]. The presence of the gradient refractive index together with the peripheral flattening of the lens is believed to increase the optical power of the lens and reduce the spherical aberration of the eye [17].

The main function of the lens is to make and maintain the best focus of the image on the retina for different object distances by adjusting the refractive power of the eye when there is a blurred image on the retina. This procedure is called accommodation and its effect is to change the radii of curvature of the lens surfaces. When the ciliary muscles contract there is a reduction in tension in the zonules attached to the lens, resulting in an increase in the surface curvatures of the lens. The increased surface curvatures of the lens change its power, and therefore the total eye power, allowing focus for near objects [6]. Typically, the lens has a total power of approximately +21D when not accommodating [18]. In young people, the lens has enough flexibility to focus for a variety of different distances (corresponding to  $\sim +15$ D of additional positive power) but after  $\sim 40$  years of age the flexibility of the crystalline lens decreases, resulting in an inability to focus near objects clearly; this is called presbyopia [19].

The retina receives the light refracted by the cornea and crystalline lens. The retina is located at the rear of the eye and is composed of several tissue layers, including one that contains the light-sensitive cells called the photoreceptors [20]. Figure 1.2a shows the anatomy of the eye. The incident light is focused on the retina and sensed by light-sensitive cells called the rods and cones (Figure 1.2b). These cells transform the light energy they receive into electrochemical activity, which then propagates through the retinal layers to the optic nerve, before passing along the visual pathway to the visual cortex. There are approximately 120 million rods and 5 million cones in the retina [18, 21]. Cones are

concentrated within the central 2 degrees of the retina (at the fovea) and their spatial density reduces rapidly with increased

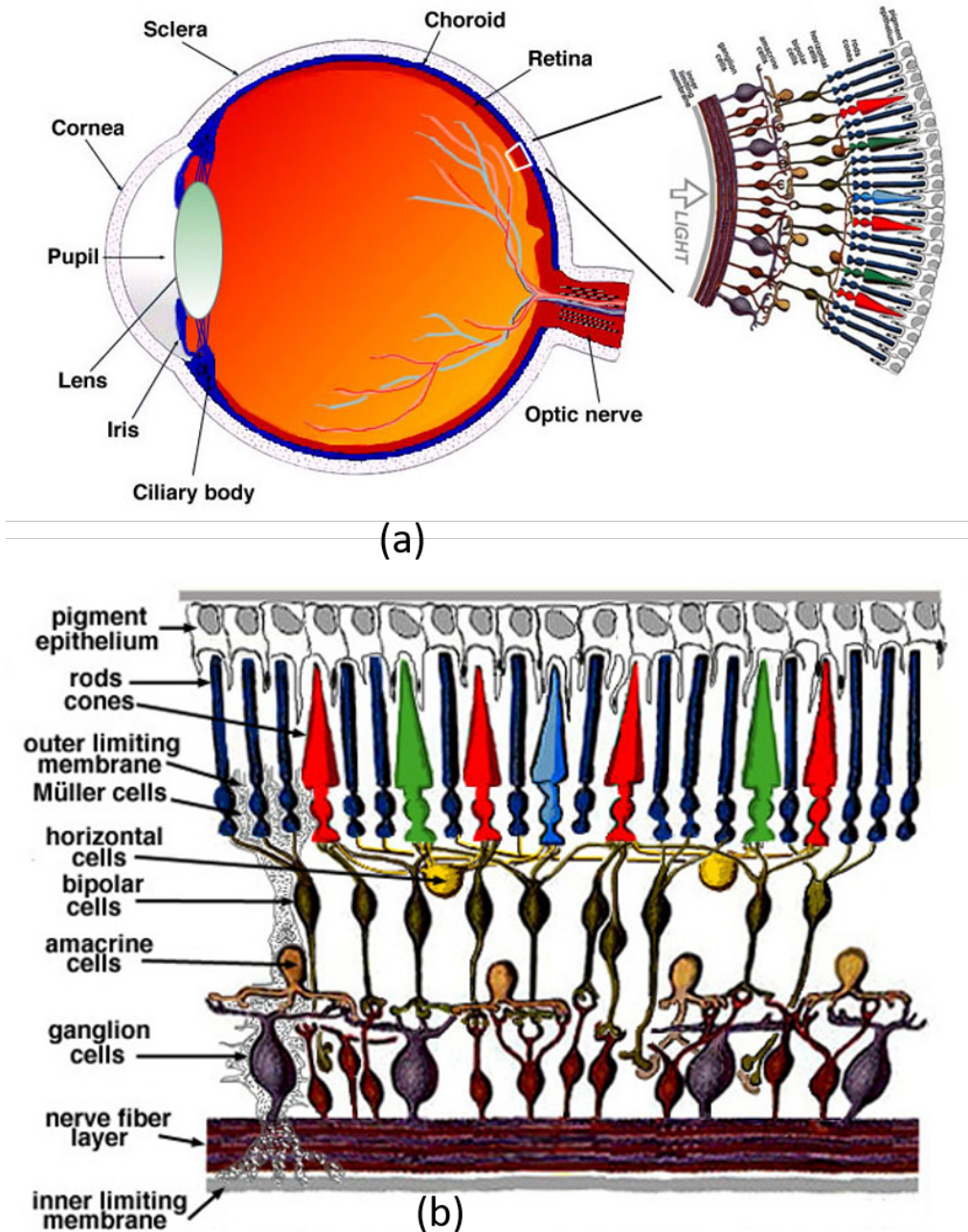


Figure 1.2. Illustration of the anatomy of the eye. Reproduced with permission from [20].

spatial eccentricity from the fovea. They are largely absent at >20 degrees eccentricity from the fovea. Rods are absent centrally and have their highest spatial density at about 20 degrees eccentric from the fovea. Outside of the fovea, the signals from rods and cones are bundled and summed in the bipolar cells and then transferred to the ganglion cells and then to the optic nerve [6].

The rod cells are extremely sensitive to light in very low illuminations but lack high spatial resolution and do not process color, thus separating optimally for scotopic vision. In comparison, the cone cells operate optimally in high illumination, process high spatial resolutions, as well as color (photopic vision) [6]. There are three types of cones: long, medium, and short wavelength sensitive cones that, respectively, describe their sensitivity to light in the visible spectrum. The absorption curves of rods and three different cones are shown in Figure 1.3. If both rods and cones contribute to vision, mesopic vision will be produced.



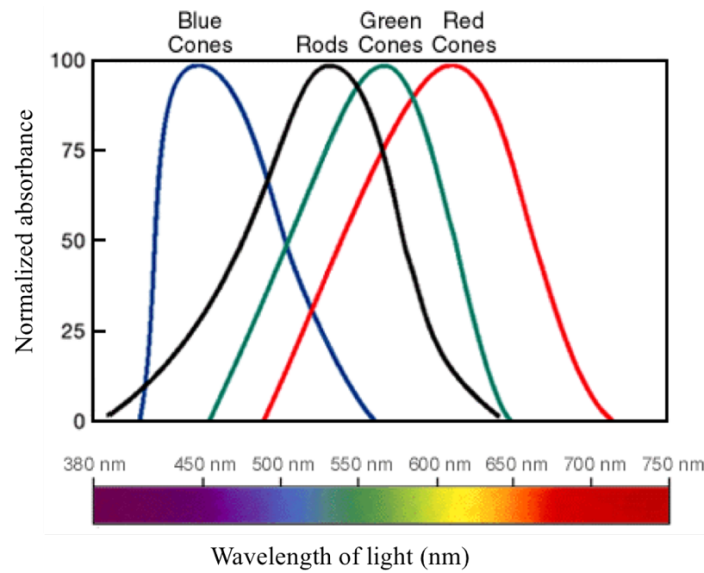


Figure 1.3. Absorption curves for the three cones types and rods. Adapted from [22].

## 1.2 Optical imperfections of the human eye

The human eye suffers from many optical imperfections, most of which correspond to refractive errors. Some refractive errors are very simple and are easily corrected with eyeglasses and contact lenses but some are very complex refractive errors and cannot be corrected by simple means. The simple ones are generally referred to as ametropia or lower order aberrations, and the more subtle and complex refractive errors are called higher order aberrations (HOA). In the human eye, a variety of aberrations present, from a simple spherical and cylindrical error (lower order aberrations) to the more complex HOAs.

### 1.2.1 Ametropia

When an image produced by the eye is located exactly on the retina, without the aid of accommodation or optical devices, then the eye is classified as emmetropic. Ametropia, one of the most common types of optical imperfection, means that some or all of the image is not

produced on the retina but, rather, is produced in front of or behind it. The effect is purely optical and can be corrected by simple means such as a spectacle lens, contact lenses, corneal laser ablation, or lenses implanted into the eye. Figure 1.4 shows a schematic diagram of a different refractive state of the eye.

Ametropia is common in the population who are otherwise healthy and is usually categorized into defocus and/or astigmatism. Defocus is the mismatch between the axial length and refractive power of the eye, resulting in a blurred image on the retina and therefore reduced vision. It is divided into two kinds: myopia and hypermetropia. If the power of the eye is too high or the axial length of the eye is too long, collimated light entering eye will focus in front of the retina and this error of refraction is called myopia. If the power of the eye is too low or the axial length of the eye is too short, collimated light entering the eye focuses beyond the retina and this error of refraction is called hypermetropia. Astigmatism is caused by asymmetry in the optics of the eye where the refractive powers between the two mutually perpendicular power meridians are different. If defocus is accompanied by astigmatism it further degrades the retinal image quality.

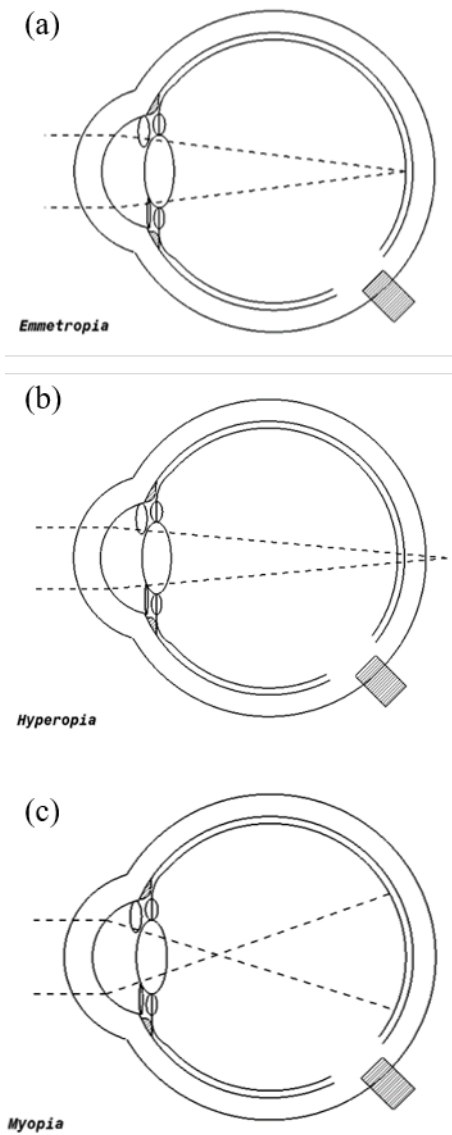


Figure 1.4. Diagram showing refractive conditions (a) emmetropia (b) hyperopia and (a) myopia.

### 1.2.2 Higher-order aberrations

HOAs are the more subtle and complex refractive errors than defocus and astigmatism. The HOA is the distortion acquired by a wavefront of light when it passes through the eye. A wavefront is a surface over which an optical wave has a constant phase. It has been found

that all eyes have at least some degree of HOAs which do not affect the general vision of the eye; however, some eyes contain a significantly high amount of HOAs that cause difficulty seeing at night, complaints of glare, halos, blurring and starburst patterns. Greater amounts of HOAs may occur due to the irregularities in the optical components of the eye such as curvature of the cornea and crystalline lens. It can also occur from scarring of the cornea from eye surgery, trauma or disease.

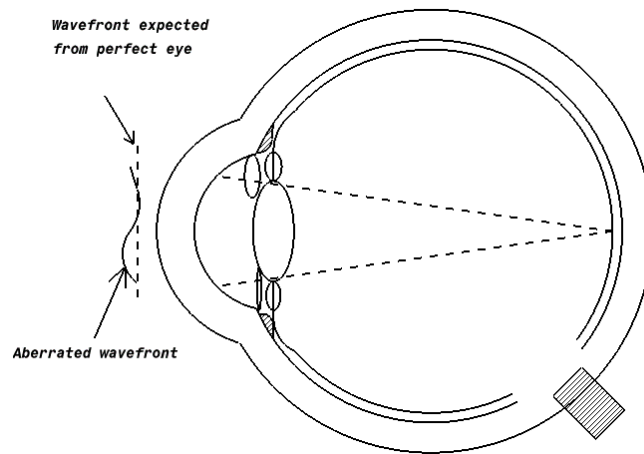


Figure 1.5. Distortions to a wavefront from a human eye.

In optics, a perfect image is formed if all rays of light from a point object after passing through all the optical system focus as a point image. However, the imperfections of the human eye's optical system do not allow a perfect point image to be formed on the retina. Light deviates from their actual positions during propagation when the optical system is not perfect. The deviation of the light from their main positions produces aberrations [23].

The aberrations of the eye can be described using a schematic of the human eye (Figure. 1.5). A laser light is used to create a point source of light on the retina. The divergent

wavefront produced from the point source of light emerges out from the eye after being refracted through the lens and cornea. For a perfect optical system, this wavefront would be flat (plane) at the pupil plane (dotted line in Figure. 1.5). Since the eye is an imperfect optical system, the outgoing wavefront always deviates from the plane wavefront and the amount of this deviation is called wavefront aberration.

There are different types of HOAs such as spherical aberration, coma, trefoil, secondary astigmatism [23-24], but many more of them are identified only by mathematical expansions (most commonly, Zernike polynomials). Higher the order of aberrations, the lower is its impact on vision [25]. These errors occur for many different reasons, such as 1: When the optical system is not perfectly in focus, 2: When refractive surfaces are not perfectly spherical, and 3: when the optical system and light source (object) are not perfectly aligned. HOAs are the most noticeable factor in reducing the quality of the retinal image when the pupil size is larger than 3.0mm in diameter [24-32].

### **1.3 Higher-order aberration measurement**

The Shack-Hartmann (SH) wavefront sensor [30] is a device designed to measure the aberrations of the eye. It measures the local slopes of the wavefront at various points at the exit pupil from which the total wavefront can be reconstructed. The deviation of the reconstructed wavefront from a reference plane wavefront allows the wavefront aberrations to be quantified. A schematic diagram of the SH wavefront sensor is shown in Figure. 1.6. A light source, usually a small laser beam, is first collimated by a lens. The collimated beam enters the eye through the beam splitter and is focused on the retina. The retina then reflects the beam back. The reflected wavefront emerges from the eye and is sampled by the lenslet

array. The lenslet array consists of hundreds of single microlenses with identical diameters and focal lengths. Each microlens spot forms an image, creating a grid of spots in the focal plane of the array of microlenses where a CCD camera is located. The wavefront is reconstructed to calculate the wavefront aberration of the optical system.

If the wavefront is completely perfect then the spots on the CCD would be equidistant from each other, forming a perfect reference image. However, the wavefront reflected back from the eye is distorted; the spots formed by each microlens are not located at the focal plane of the microlens but are displaced from their reference position as shown in Figure. 1.7. The local slope of the wavefront at each lenslet position is determined by the degree of displacement of the spot from its reference position, which enables the entire wavefront to be reconstructed.

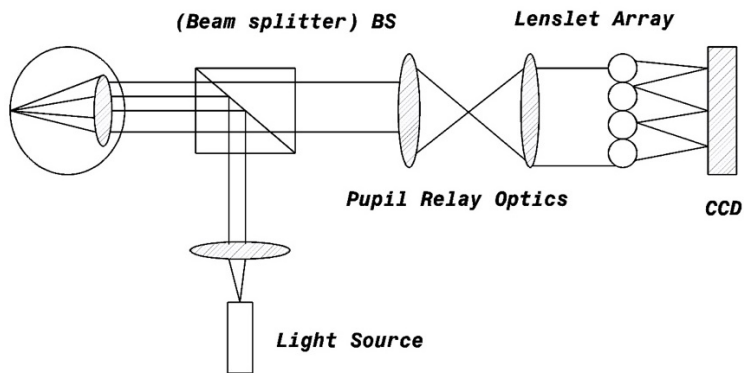


Figure 1.6. SH wavefront sensor layout.

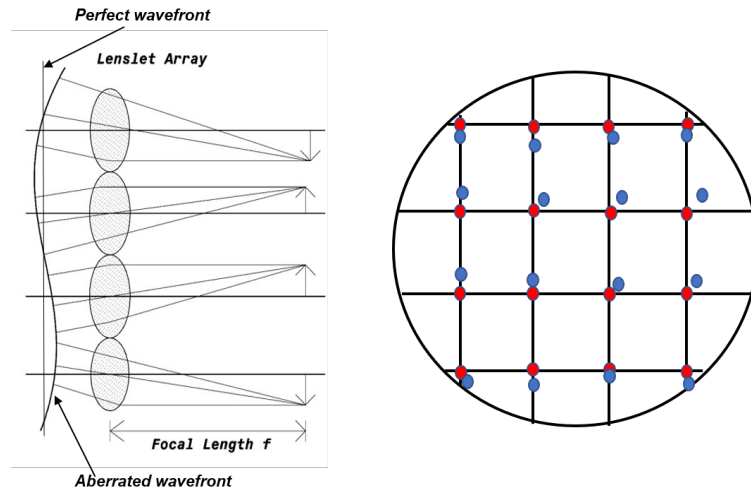


Figure 1.7. Displacement caused by an aberrated wavefront. Orthogonal view (Left) and transverse view (right). Blue dots and red dots in the transverse view the centroids of the perfect and aberrated wavefront.

Most clinical aberrometers use Zernike polynomials to report the wavefront aberrations of the eye [33-35]. The Zernike polynomials are a set of orthogonal basis functions over a circle of unit radius and are able to describe wavefront aberration of an optical system accurately [33]. Furthermore, the International Standards Organization ISO 24157 also recommends Zernike polynomials for reporting the optical aberrations of human eyes [34]. The Zernike polynomials have the following three advantages. First, they are mathematically independent (mutually orthogonal) to each other. It is possible to perform statistical analysis or even remove certain terms from the data without affecting the contribution of the other terms. Second, each Zernike polynomial term represents a different type of aberration with its unique shape. The coefficient of each term indicates the amount of particular aberration present in that eye. Third, when Zernike polynomials are normalized, the absolute value of

the coefficient is the RMS contribution of that term, and that enables a relative comparison of Zernike coefficients [35].

The Zernike Polynomials are defined as [33]:

$$\begin{aligned} Z_n^m(\rho, \theta) &= N_n^m R_n^{|m|}(\rho) \cos(m\theta) && \text{for } m \geq 0, 0 \leq \rho \leq 1, 0 \leq \theta \leq 2\pi \quad (1.1) \\ &= -N_n^m R_n^{|m|}(\rho) \sin(m\theta) && \text{for } m < 0, 0 \leq \rho \leq 1, 0 \leq \theta \leq 2\pi \end{aligned}$$

for a given  $n$ ,  $m$  can only take on values of  $-n, -n+2, -n+4, \dots, n$

$N_n^m$  is the normalization factor where

$$N_n^m = \sqrt{\frac{2(n+1)}{1+\delta_{m0}}} \quad \delta_{m0} = 1 \text{ for } m = 0 \quad (1.2)$$

And,  $R_n^{|m|}(\rho)$  is the radial polynomial where

$$R_n^{|m|}(\rho) = \sum_{s=0}^{(n-|m|)/2} \frac{(-1)^s (n-s)!}{s! [0.5(n-|m|)-s]! [0.5(n-|m|)+s]!} \rho^{n-2s} \quad (1.3)$$

Table 1.1 contains a list of Zernike polynomials up to the 5<sup>th</sup> order. Figure 1.8 shows graphic representations of the Zernike polynomials up to the 5<sup>th</sup> order in a pyramid arrangement. In general, the wavefront aberration  $W(\rho, \theta)$  is represented as a linear combination of the Zernike polynomials:

$$W(\rho, \theta) = \sum_{n,m} C_n^m Z_n^m(\rho, \theta) \quad (1.4)$$

Where  $Z_n^m$  are the Zernike polynomials and  $C_n^m$  are their corresponding coefficients [35]. The indices  $n$  and  $m$  represent the radial order and azimuthal frequency of the azimuthal component, respectively. Similarly,  $\rho$  and  $\theta$  are the variables of the polar coordinate system.



Table 1.1. A list of Zernike polynomials up to 5<sup>th</sup> order (J=mode, n=order, m=frequency).

J	n	m	$z_n^m$	Meaning
0	0	0	1	Constant term, or Piston
1	1	-1	$2\rho \sin(\theta)$	Tilt in the y-direction, Distortion
2	1	1	$2\rho \cos(\theta)$	Tilt in the x-direction, Distortion
3	2	-2	$\sqrt{6}\rho^2 \sin(2\theta)$	Astigmatism with axis at $\pm 45^\circ$
4	2	0	$\sqrt{3}(2\rho^2 - 1)$	Field curvature, Defocus
5	2	2	$\sqrt{6}\rho^2 \cos(2\theta)$	Astigmatism with axis at $0^\circ$ or $90^\circ$
6	3	-3	$\sqrt{8}\rho^3 \sin(3\theta)$	Trefoil along the y-axis
7	3	-1	$\sqrt{8}(3\rho^3 - 2\rho) \sin(\theta)$	Coma along the y-axis
8	3	1	$\sqrt{8}(3\rho^3 - 2\rho) \cos(\theta)$	Coma along the x-axis
9	3	3	$\sqrt{8}\rho^3 \cos(3\theta)$	Trefoil along the x-axis
10	4	-4	$\sqrt{10}\rho^4 \sin(4\theta)$	Quadrofoil along the y-axis
11	4	-2	$\sqrt{10}(4\rho^4 - 3\rho^2) \sin(2\theta)$	Secondary Astigmatism
12	4	0	$\sqrt{5}(6\rho^4 - 6\rho^2 + 1)$	Spherical Aberration, Defocus
13	4	2	$\sqrt{10}(4\rho^4 - 3\rho^2) \cos(2\theta)$	Secondary Astigmatism
14	4	4	$\sqrt{10}\rho^4 \cos(4\theta)$	Quadrofoil along the x-axis
15	5	-5	$\sqrt{12}\rho^5 \sin(5\theta)$	Pentafoil along the y-axis
16	5	-3	$\sqrt{12}(5\rho^5 - 4\rho^3) \sin(3\theta)$	Secondary trefoil along the y-axis
17	5	-1	$\sqrt{12}(10\rho^5 - 12\rho^3 + 3\rho) \sin(\theta)$	Secondary coma along the y-axis
18	5	1	$\sqrt{12}(10\rho^5 - 12\rho^3 + 3\rho) \cos(\theta)$	Secondary coma along the x-axis
19	5	3	$\sqrt{12}(5\rho^5 - 4\rho^3) \cos(3\theta)$	Secondary trefoil along the x-axis
20	5	5	$\sqrt{12}\rho^5 \cos(5\theta)$	Pentafoil along x-axis

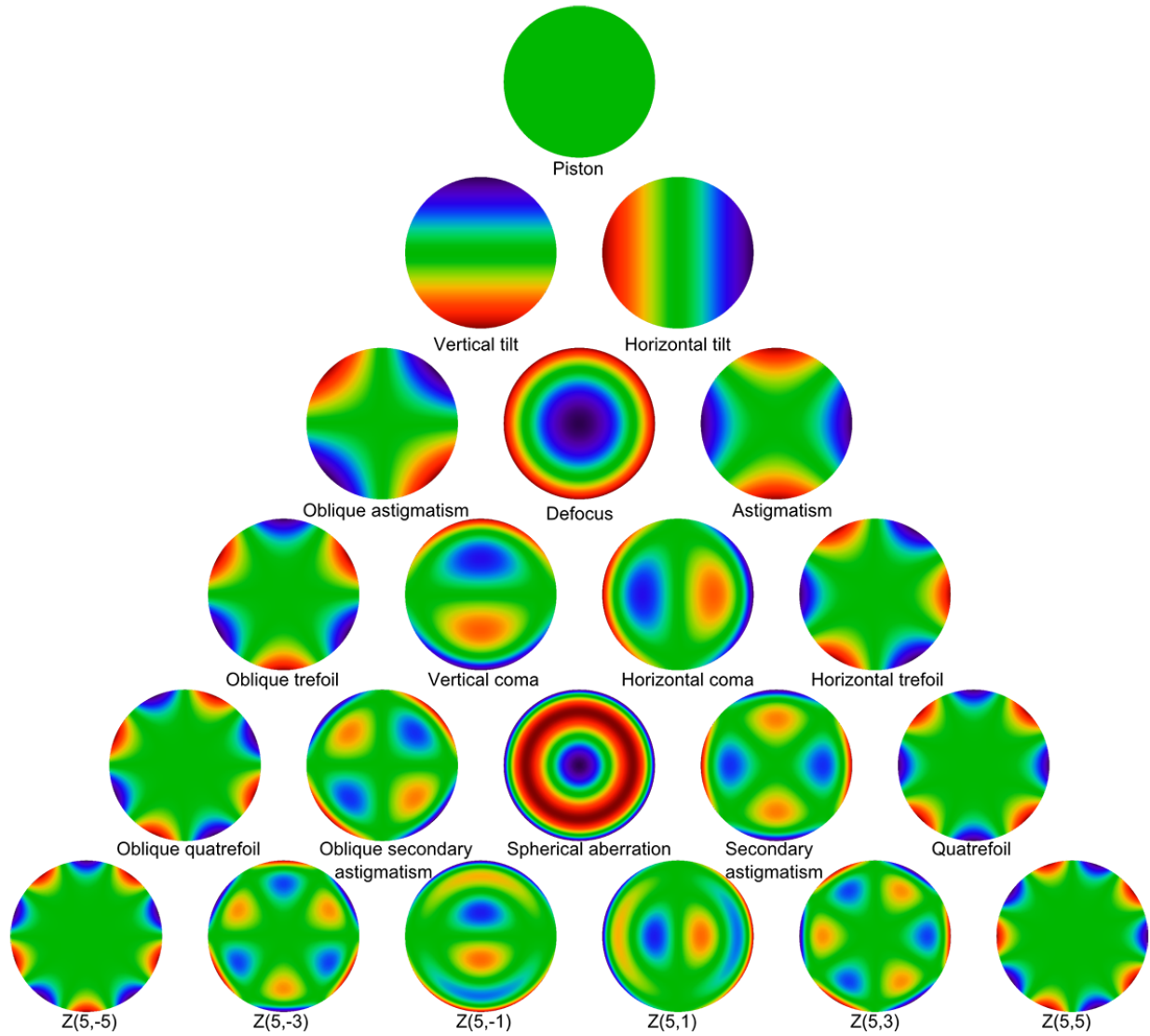


Figure 1.8. Zernike polynomials up to 5th order plotted on a unit circle. Reproduced with permission from [36].

Each Zernike coefficient determines the contribution of the corresponding term in the total wavefront. The level of deviation from the ideal wavefront and amount of the distortion of the system can be obtained by calculation of the RMS error of the wavefront [23], where

$$RMS = \sqrt{\sum(C_n^m)^2} \quad (1.5)$$

The second order aberrations are the simple, ametropic refractive errors of the eye. The 3<sup>rd</sup> order and above are called HOAs of the eye. The HOAs contribute little to the total monochromatic aberration of the eye. However, when there is no uncorrected lower order aberration, poor vision can be attributed to HOAs. The pupil size also affects the magnitude of the aberrations. For instance, in low light levels, the increase in pupil size results in an image with increased HOAs and poorer vision. The aberrations are expressed in terms of Zernike coefficients; however, the Zernike coefficients depend on many factors such as the pupil size, number of spots used to generate Zernike coefficients, centroid measurement techniques, and noise in the SH images. The main aim of this thesis is to examine the reliability of wavefront aberration measurement at scaled pupil size, and reduced SH spots number. I also examined the effect of many centroid measurement techniques before and after the noise suppression in the SH images.

#### **1.4 Contribution of the thesis**

The wavefront aberration is the deviation of an actual wavefront from the ideal wavefront. The actual wavefront is reconstructed from the focal spots, therefore the aberration is mainly dependent upon the measurement accuracy of the centroid of the focal spot. There are lots of centroid measurement techniques available in the literature, therefore a performance

comparison of these methods is worth pursuing through further experimental work. Also, the SH images are noisy, therefore a comparison of different centroid estimation methods after using some pre-processing steps (thresholding, Gaussian smoothing, and adaptive windowing) is also important. In this thesis, I examine the most commonly used centroid estimation methods, such as brightest spot centroid; first-moment centroid; the weighted center of gravity and intensity weighted center of gravity. This study examines whether these centroid estimation methods give meaningfully different results for spherical defocus ( $>0.25D$ ) when measuring the aberration of the human eye. It also provides an insight into the implication of noise suppression on the SH images before the Zernike coefficients calculation.

One challenging parameter in measuring the aberration of the human eye is the pupil size dependency of Zernike polynomials. Several recent studies have examined the relationship between refractive error and Zernike coefficients of HOA and have used pupil size scaling to scale the aberrations to a common pupil size, smaller than the natural pupil size [19]. However, their research questions were not intended to examine the pupil scaling technique itself. The scaling up approach uses a fewer set of sensor elements to extract Zernike coefficients than the Zernike coefficients derived from spots within the fixed pupil size. Similarly, the scaling down approach uses a larger set of sensor elements to extract Zernike coefficients than the Zernike coefficients derived from spots within the fixed pupil size. The literature lacks the validation of pupil scaling techniques by comparison with the measured clinical data. In this thesis, we validate the mathematical pupil size scaling formula by

comparing the estimates of the Zernike coefficients with corresponding clinical measurements obtained at different pupil sizes.

The other challenging parameter in measuring the aberration of the eye is that the reconstruction technique requires several SH spots for reliable estimation of the aberration. However, for some conditions, the spots can be extremely blurry and indistinct with the background or miss the spots. This can occur when any part of the optical path is blocked. In this thesis, I estimate wavefront aberrations from the missing spot data to test the reliability of the wavefront aberration measurements. In the first experiment, I randomly delete a fixed percentage of spots (up to 80%) from the SH image and calculate the Zernike coefficients from the reduced data set. The aberration calculated from the reduced set of spots is compared with the original aberrations. In the second experiment, I examined the effect of clustered missing spots by creating various missing spot models using tape on a spectacle lens. These deletions of spots model the possible reduction in the number of lenslets providing data when imaging an eye ocular disease, such as cataract. The aberration obtained from SH images with these different models are compared with an image without the missing spots. The findings of this study will provide insight into whether the ocular aberration measurements obtained from eyes with clustered missing spots are significantly impacted or not.

## **1.5 Organization of the thesis**

The thesis is structured as follows. In Chapter 2, construction of custom-made SH wavefront sensor is described. This includes hardware construction to acquire SH image from the eye

and software development for extracting Zernike coefficients from the SH image. In Chapter 3, a performance comparison of different centroid estimation methods with and without pre-processing techniques is described. In Chapter 4, a validation of the mathematical pupil size scaling formula by comparing the estimates of the Zernike coefficients with corresponding clinical measurements obtained at different pupil sizes is presented. In Chapter 5, I present the estimation of wavefront aberration data from several methods giving a reduced number of SH spots. Chapter 6 concludes the thesis and describes some future directions.

## **Chapter 2**

### **Construction and calibration of the custom-made Shack-Hartmann aberrometer**

#### **2.1 Introduction**

The custom-made aberrometer constructed in our lab was based on the design developed by Dr. Luis Diaz Santana, at City University, London, UK [37]. It allows for free binocular viewing of a target while data is collected. This feature better replicates natural viewing conditions, thus providing a more realistic picture of the state of ocular aberrations over time. A distant target is placed in front of participants in a dimly lit room so that their accommodation effect is minimized, and the natural pupil size is maximized without the need for intervention with therapeutic agents (i.e. mydriatic eye drops). The measurement normally requires less than a few seconds for each eye plus a few minutes for the adjustment; however, there is variability depending upon subject cooperation. The aberrometer records data at a rate of 24 frames per second. These frames are then averaged to substantially improve the accuracy of the system by minimizing the noise [37]. Examining sequences of images and averaging the outputs further minimize the random fluctuations in the aberration [38].

#### **2.2 Aberrometer design**

A schematic illustration of the optical setup of the custom-made aberrometer is shown in Figure 2.1. It was built using Qioptiq Microbench optical system mounts (Qioptiq, Waltham, MA, USA) and all optical components were purchased from LINOS Photonics (LINOS

Qioptiq, USA). The light source is a focusable circular beam laser diode (LD) with a wavelength of 780nm, a maximum output of 5mW, a maximum beam diameter of 5mm. The source is converged by a 25X microscope objective (MO) to its focal point where a pinhole (PH) is located. This procedure spatially filters the beam to a beam width of 1mm or less, effectively limiting the proportion of the maximum power of the light source allowed to enter the instrument and, therefore, acts to ensure ocular safety [39-40]. A +25D lens, L1, (Achromatic,  $f=40\text{mm}$ , diameter = 18mm with ARB2-VIS coating is positioned 40mm from the PH; as this distance corresponds to the anterior focal point of L1, it collimates the beam emergent from the PH. An adjustable iris is positioned beyond L1 to adjust the diameter of the beam. The size of the beam is adjusted in such a way that diffraction on the retina is limited and the SH spots will have a higher signal-to-noise ratio (SNR), thus improving the image quality. Beyond L1, an adjustable flat mirror (M1) that diverts the beam towards beam splitter (BS) is positioned. A plane hot mirror (HM), angled precisely at  $45^\circ$ , is placed in the path of the light emerging from the beam splitter, that allows the light to deviate from the subject's eye while they view the distant target. The HM (200mm $\times$ 130mm) serves a double purpose as it reflects the infrared light scattered from the retina into the wavefront sensing system whilst permitting visible light from the stimulus to pass through the mirror and be seen binocularly by the subject [37]. The light reflected by the retina is returned to BS and passed through a series of relay lenses (L2 & L3) and focused on the sensor through an array of lenslets (pitch=150 $\mu\text{m}$ ,  $f=5.2\text{mm}$ ; Thorlabs Inc., Newton, NJ, USA). The lenslet array and CCD camera (CV-M50 IR; JAI Inc., San Jose, USA) were used for sensing the wavefront of the light coming out of the eye. The eye's pupil is made conjugate with the lenslet array by means of the relay lenses, which are positioned such that the posterior focal point of L2 ( $f_2=+250\text{mm}$ ) is coincident with the anterior focal



point of L3 ( $f_3=200\text{mm}$ ), amounting to an afocal telescope set-up, whereby collimated light enters L2 and emerges from L3. The lenslet array has a focal length of 5.2mm and the telescopic system has a magnification of 1.25X,  $\left(\frac{f_2'}{f_3'} = \frac{250\text{ mm}}{200\text{ mm}}\right)$ . The mirror, M4, is used for collecting reference data. To do this, the iris, I, is kept fully open and a one-second period of data (24 images) is collected. The system is mounted on a modified Bausch and Lomb slit lamp base (with the optical components of the slit lamp removed) and has a custom-made chinrest (Figure 2.2).

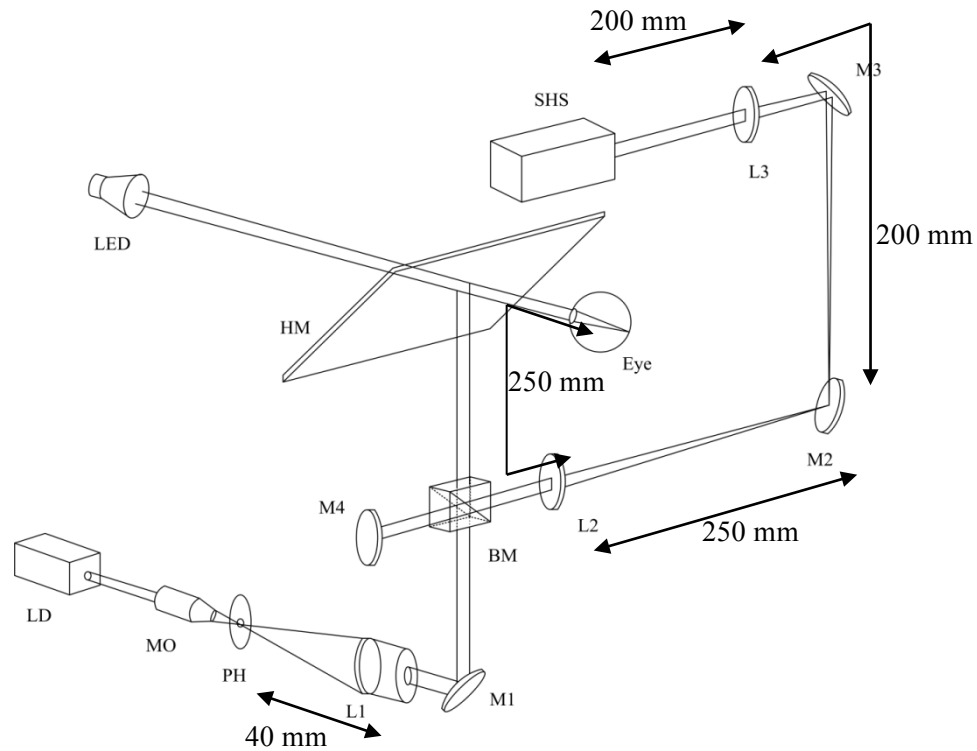


Figure 2.1. Schematic illustration of the optical setup: LD = laser diode; MO = microscope objective; PH = pinhole; L1, L2, and L3 = lenses; M1, M2, and M3 = mirrors; M4 = removable mirror used for calibration; BM = beam splitter; HM = hot mirror; SHS = SH system.

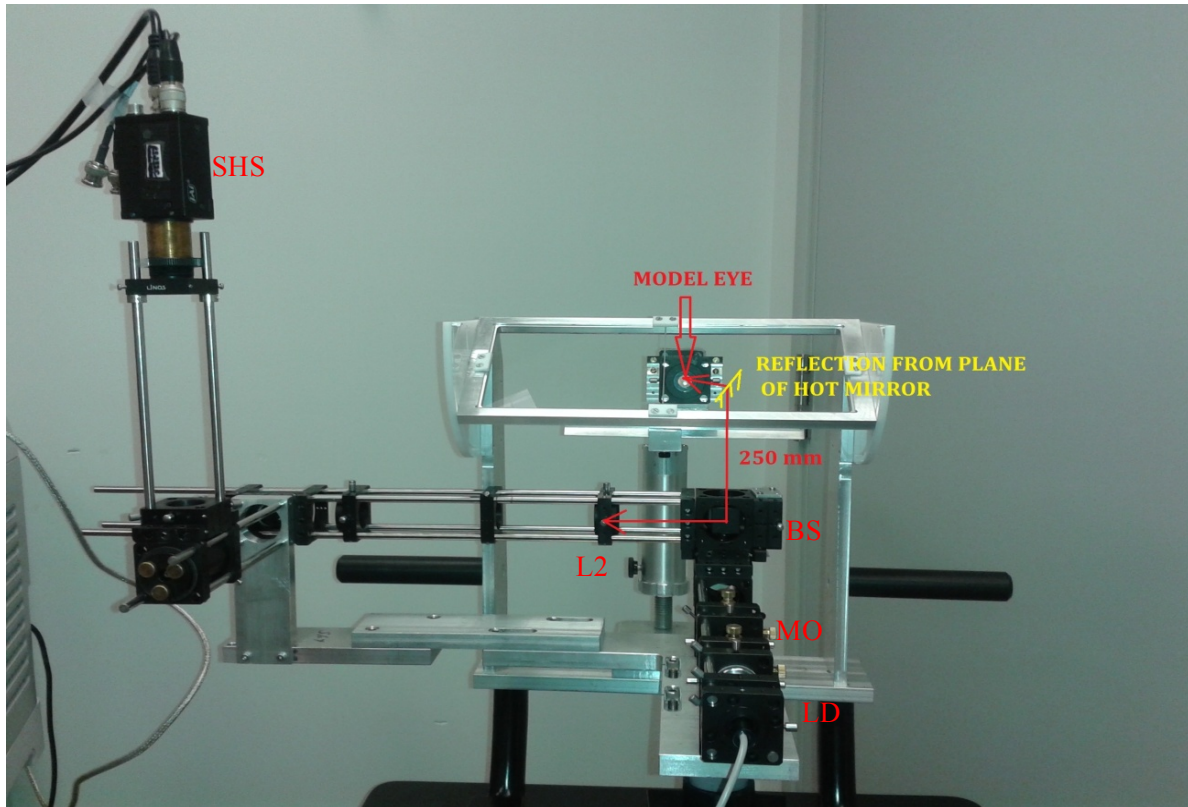


Figure 2.2. The SH wavefront aberrometer. The components, as described in the text, are: laser diode (LD), microscope objective (MO), pinhole (PH), beam splitter (BS), hot mirror (HM), relay lenses (L2+L3), mirror (M1, M2, M3, M4) and shack-Hartmann sensor (SHS).

### 2.3 Alignment procedure

Optical alignment is very important in aberrometry in order to ensure that the planes of the lenslet array and the participant's pupil are conjugate. The following steps were taken to check the system settings and alignment.

**a. Light source collimation:** When a light source is collimated, the beam width should remain constant over, at least, the distance of the length of the path through the instrument. To check that the source was collimated after passing through L1, the width of the beam was measured at several distances from L1 by means of a small piece of white card with a

transparent graticule placed in a mount, coaxial with the laser source. The graticule had a central 1mm circle and 1mm spaced ticks beyond the central circle. The mount was placed at various distances (up to 1m in 10cm increments and then in meter increments to 5m) from the light source. The process was restarted if the beam became visibly smaller or larger than 1mm diameter at any distance from the laser source. If the beam width was not constant at 1mm for all distances, the laser focusing mechanism was adjusted and the measurements repeated systematically until a constant beam diameter was achieved across all distances. Also, the wavefront sensor was directly connected to the collimated beam and measured the wavefront. In this way, the quality of alignment can be checked. If the aberrations are small, the alignment can be improved by fine adjustment of the position of the lens with the help of the micrometer screw.

**b. Centration of the beam in the system:** After the laser beam is collimated, a transparent sheet is placed in front of the pinhole, and the center of the mounting plate is located and marked on the transparency. The pinhole has two adjustable screws by which the horizontal and vertical position of the pinhole in the mounting plate, perpendicular to the path of the beam, can be adjusted. The screws are adjusted so that the pinhole aperture is centered with the pinhole mount marked on the transparency. Since all the optical elements positioned after MO are in identical commercial mounting plates, the transparency could then be used to ensure that they were all similarly centered relative to each other. At the beam splitter, centration of the beam for the path from BS to HM is checked with the transparency positioned on the top side of the cube in which the beam splitter is mounted. To check the beam centration between BM and L2, mirror M4 was uncovered and the transparency is

positioned on the side of the cube nearest to L2. Flat mirrors M1, M2, and M3 have three adjustable screws that can be used to adjust the beam position if it was not correctly centered. A second adjustable iris is placed after L2 to help control the size of the surface reflection of the lens of the model eye. During adjustment, the monitor displaying the spot pattern of the SH lenslet array is monitored constantly to ensure that they were uniform, sharp and centered [41].

## **2.4 Analysis software**

The software was written in MATLAB and provides Zernike coefficients from the SH images. First, we collected reference data by opening mirror M4 and with all pupils fully opened. Six seconds of data were recorded and saved in the Reference folder. The code prompts for the file numbers from the series of reference images to be used in the analysis. After obtaining the reference images, mirror M4 was closed and the model eye was mounted in the chinrest and the data was collected. The aberrometer records images at a rate of 24 frames per second. These images were averaged to reduce random noise in the images. The following steps were performed to calculate Zernike coefficients from the SH images (Figure 2.3).

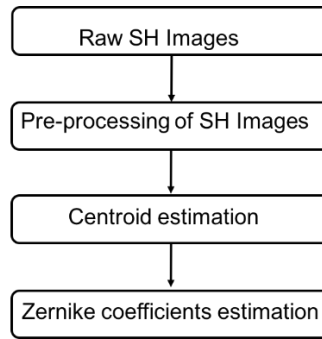


Figure 2.3. A flowchart illustrating the steps performed to calculate Zernike coefficients from raw SH images.

### **Step I: Pre-processing of SH images**

The SH sensor acquires a monochromatic image and in the process of transferring data from the sensor to the computer for analysis the converter box (from analog to digital) divides the image into RGB channels. To return the output to a single monochromatic image, the weighted means of red, green and blue channels were taken using formula 2.1.

$$V = 0.2989R + 0.5870G + 0.1140B \quad (2.1)$$

where  $R$ ,  $G$ , and  $B$  denote the red, green and blue channel intensity values of a pixel and  $V$  is the corresponding grayscale intensity value. Equation 2.1 is the standard grayscale conversion formula adopted by image processing software. Figure 2.4a shows the representation of an image taken by the scanner.

The grayscale images were subjected to thresholding to further remove the noise. Hard thresholding was used to keep the time complexity small without degrading the accuracy. The threshold depends on several factors, such as illumination, noise level and the quality of the image. If there are some reflections on the SH image such that the spots become blurry with slightly illuminated regions outside the SH spot edges, the threshold has to be modified

to be on the higher side. Similarly, the threshold value has to be lowered if the overall image illumination is low. The image is now rendered purely black and white, with each pixel having intensity either 0 or 255; 0 represents black, while 255 represents white. All pixels of the grayscale image having an intensity below  $T$  are assigned intensity value 0, while other pixels are assigned intensity value 255. Figure 2.4b illustrates the black and white version of the image shown in Figure 2.4a. Sometimes a small reflection of light may appear in the image and the software may misclassify the white reflection as a spot. However, if a spot is real, it consists of a cluster of a certain number of pixels and is greater than the number of pixels in a reflection. The number of pixels in a cluster can be obtained by using the connected components MATLAB function and a corresponding threshold with respect to the number of connected pixels forming the spot can be used to avoid noise being counted as a spot. A spot is considered real if it consisted of at least 10 connected pixels. After specifying the spots, the images were then filtered using a Gaussian filter to further reduce the noise level.

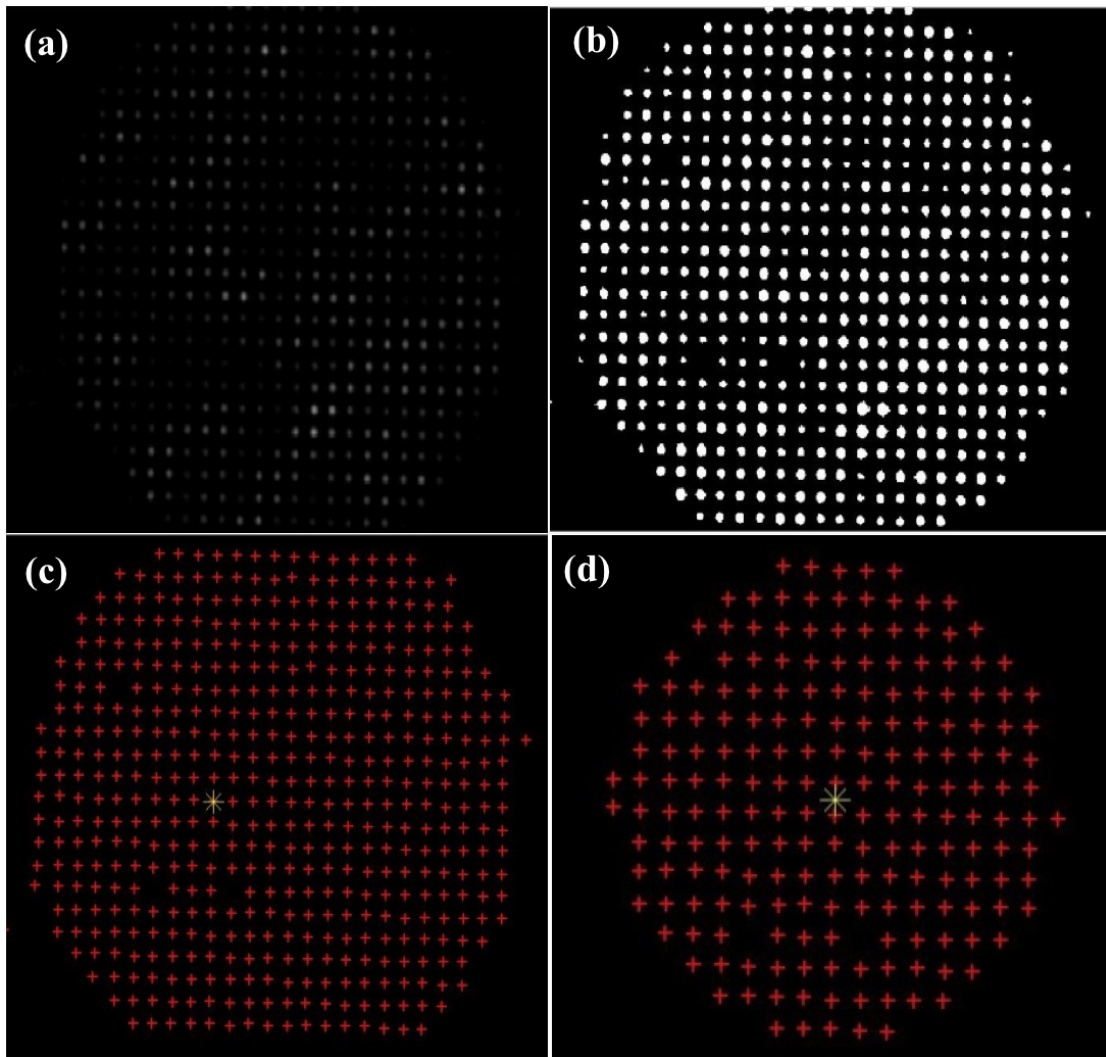


Figure 2.4. (a) Original image obtained by the scanner (b) corresponding black and white image of (a). (c) Centroids of spots calculated from (b). (d) A circular image extracted from the geometrical center of the image.

**Step II: Centroid estimation:** The accuracy of optical aberrations in SH wavefront sensor is highly dependent on the estimation of the centroid of the spot. Centroid estimation is influenced by reflection, scattering, and noise in the spot. In conventional methods, the whole sub-aperture of each lenslet is used as the detection window. When spots are far from their

reference position or the intensity of the noise in the spots is high, estimation of centroid accuracy is lowered. Instead of using the entire sub-aperture area of each lenslet for estimating the centroid of the spot, the boundaries of all individual spots classified through thresholding are evaluated and are used to define a dynamic rectangular boundary around each spot. The calculation of the centroid is then processed only within the window as shown in Figure 2.5. This also helps reduce the processing time required due to a smaller region of processing. The centroid of the SH spot can be estimated in several ways such as brightest spot center, first moment (center of mass/gravity), weight centroid of gravity, and intensity weighted center of gravity. The detailed descriptions of the various centroid estimation methods are described in Chapter 3. Figure 2.4c shows the centroid of the image shown in Figure 2.4b. After centroid calculation, a circular image is extracted from the geometrical center of the image (Figure 2.4d). The circular image is used for calculating the wavefront aberration.

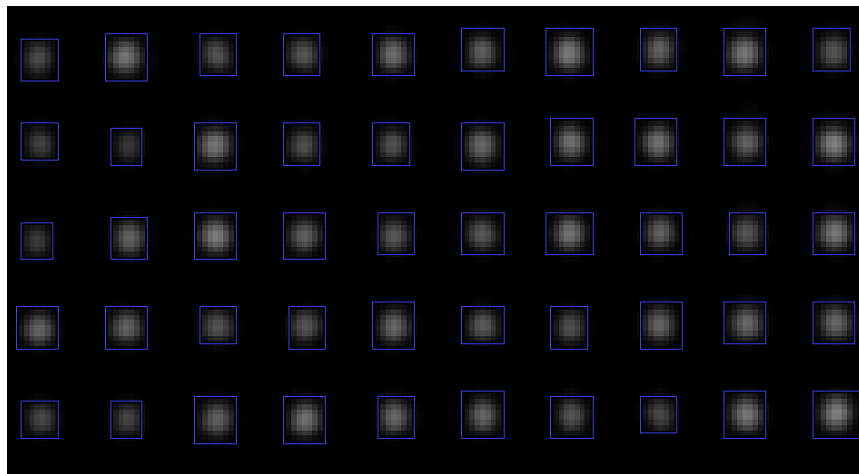


Figure 2.5. SH spot pattern showing the adaptive window around each spot used to determine the centroid of the spot.



### Step III: Wavefront aberrations calculation

The image taken from the model eye and reference image were compared and the deviation of spots of the real image from the reference image at each pixel location, in both the horizontal and vertical directions, was determined. The deviation was used to calculate the slope of the local wavefront at each position [35].

$$\begin{aligned}\frac{\partial W(x, y)}{\partial x} &= \frac{\Delta x}{f} \\ \frac{\partial W(x, y)}{\partial y} &= \frac{\Delta y}{f}\end{aligned}\quad (2.2)$$

where  $f$  denotes the focal length of the lenslet array,  $\Delta x$  and  $\Delta y$  are the respective shifts of each centroid along the x and y axis in Cartesian coordinates, respectively.

The wavefront aberration in terms of the Zernike polynomials is

$$W(x, y) = \sum_{j=0}^{\infty} C_j Z_j(x, y) \quad (2.3)$$

where  $C_j$  are coefficients of Zernike polynomials  $Z_j$  [35].

Taking the derivative of Eq. 2.3.

$$\begin{aligned}\frac{\partial W(x, y)}{\partial x} &= \sum_{n=0}^{\infty} C_j \frac{\partial Z_j(x, y)}{\partial x} \\ \frac{\partial W(x, y)}{\partial y} &= \sum_{n=0}^{\infty} C_j \frac{\partial Z_j(x, y)}{\partial y}\end{aligned}\quad (2.4)$$

And from equation 2.3 and 2.4.:

$$\begin{aligned}\frac{\Delta x(x, y)}{f} &= \sum_{n=0}^{\infty} C_j \frac{\partial Z_j(x, y)}{\partial y} \\ \frac{\Delta y(x, y)}{f} &= \sum_{n=0}^{\infty} C_j \frac{\partial Z_j(x, y)}{\partial y}\end{aligned}\quad (2.5)$$

In expanded form, equation (2.5) is written as [35]

$$\begin{bmatrix} \frac{\Delta x(x_1, y_1)}{f} \\ \frac{\Delta x(x_1, y_2)}{f} \\ \vdots \\ \frac{\Delta x(x_k, y_k)}{f} \\ \frac{\Delta y(x_1, y_1)}{f} \\ \frac{\Delta y(x_1, y_2)}{f} \\ \vdots \\ \frac{\Delta y(x_k, y_k)}{f} \end{bmatrix} = \begin{bmatrix} \frac{\partial Z_1(x_1, y_1)}{\partial x} & \frac{\partial Z_2(x_1, y_2)}{\partial x} & \cdots & \frac{\partial Z_p(x_1, y_1)}{\partial x} \\ \frac{\partial Z_1(x_1, y_2)}{\partial x} & \frac{\partial Z_2(x_1, y_2)}{\partial x} & \cdots & \frac{\partial Z_p(x_1, y_2)}{\partial x} \\ \vdots & \vdots & \ddots & \vdots \\ \frac{\partial Z_1(x_k, y_k)}{\partial x} & \frac{\partial Z_2(x_k, y_k)}{\partial x} & \cdots & \frac{\partial Z_p(x_k, y_k)}{\partial x} \\ \frac{\partial Z_1(x_1, y_1)}{\partial y} & \frac{\partial Z_2(x_1, y_1)}{\partial y} & \cdots & \frac{\partial Z_p(x_1, y_1)}{\partial y} \\ \frac{\partial Z_1(x_1, y_2)}{\partial y} & \frac{\partial Z_2(x_1, y_2)}{\partial y} & \cdots & \frac{\partial Z_p(x_1, y_2)}{\partial y} \\ \vdots & \vdots & \ddots & \vdots \\ \frac{\partial Z_1(x_k, y_k)}{\partial y} & \frac{\partial Z_2(x_k, y_k)}{\partial y} & \cdots & \frac{\partial Z_p(x_k, y_k)}{\partial y} \end{bmatrix} \begin{bmatrix} C_1 \\ C_2 \\ \vdots \\ C_p \end{bmatrix}\quad (2.6)$$

or alternately, as a matrix equation form

$$m = ZC \quad (2.7)$$

This equation can be solved by using a Least Square Fit (LSF) method [35]. Zernike coefficients  $C$  are estimated using the pseudo inverse of  $Z$ , given by equation (2.8)

$$C = (Z^T Z)^{-1} Z^T m \quad (2.8)$$

The Zernike coefficients calculated from one of the SH images is shown in Figure 2.6.

```

Zernike_coeff =
    0
    0
   -1.2484
   -9.9349
    2.9861
   -1.0643
    0.6750
   -0.0966
    0.6099
    1.4290
   -0.2206
   -0.0613
    0.1922
   -0.5739
   -0.3939
   -0.6762
    0.0784
    0.0382
    0.4166
   -1.3792

```

```
S =
```

```
2.1232
```

Figure 2.6. Snapshot of the results of the software showing Zernike coefficients from 1<sup>st</sup> to 5<sup>th</sup> order and spherical dioptric power calculated from the 5<sup>th</sup> Zernike term ( $Z_2^0$ ). A trial lens having power +2.0 D was placed in front of the model eye to record these data.

## 2.5 Calibration

A model eye (Figure 2.7) was constructed for the calibration of the wavefront sensor. It was a simple, reduced model eye comprising a lens (+7.69D, ARB 2 NIR) serving as the cornea, a pupil, and an image plane (retina). The lens of the model eye had a focal length of 130mm and the image plane was located at the focal point of the lens. Unmarked white printer paper served as the retina to provide a high degree of diffuse reflection. Similarly constructed

model eyes were used by Diaz-Santana et. al. [37] and Valdivieso-Gonzalez et. al. [42]. The model eye was mounted on the custom-made chinrest such that the centerline of the optics of the model eye was aligned with the center of the other part of the optical system (Figure 2.7). The system had the ability to adjust the position of the model eye in all directions (i.e. left and right, up and down, and back and forth). The diaphragm was positioned in front of the model eye to simulate an iris and the diameter of the diaphragm was fixed at 5mm for calibration.

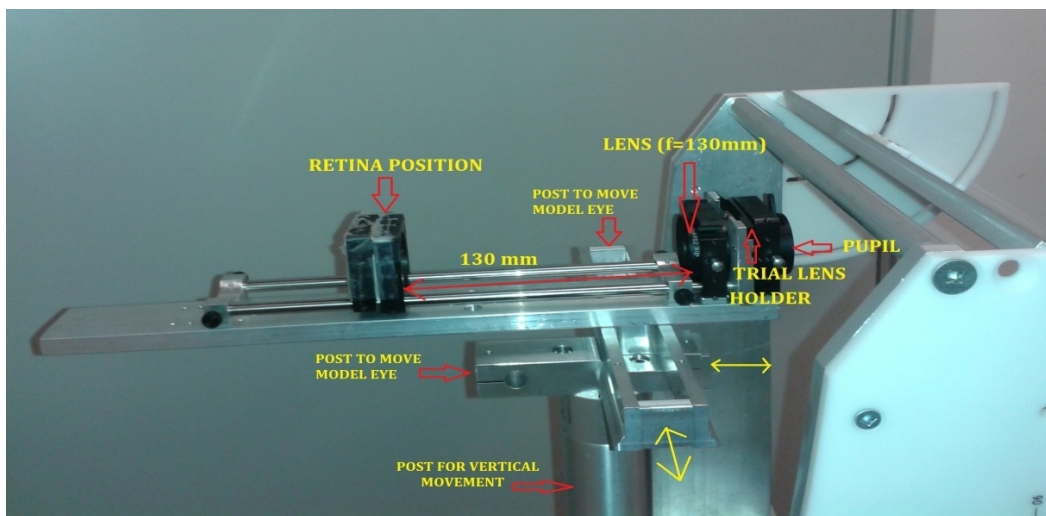


Figure 2.7. Setup of the model eye of calibration of the analysis software.

Test data were obtained for a variety of levels of defocus, which were induced by changing the spherical power of the lens in front of the model eye by inserting trial lenses. Dioptric defocus levels between -3.5D and +3.5D, in increments of 0.5D, were used. Three measurement trials were obtained at each level of defocus.

The M power vector, which is the same as the equivalent sphere, was determined from the following equation

$$M = (-4\sqrt{3})C_2^0/y^2 \quad (2.10)$$

where y is the pupil radius [43]. The M value was calculated for calibration with a pupil size of 5.0 mm.

Similarly, J0 and J45 [43] were calculated according to equations (2.11) and (2.12).

$$J_{45} = (-2\sqrt{3})C_2^{-2}/y^2 \quad (2.11)$$

$$J_0 = (-2\sqrt{3})C_2^{+2}/y^2 \quad (2.12)$$

Where  $C_2^0$ ,  $C_2^{-2}$  and  $C_2^{+2}$  were separately calculated from each trial.

$$S = \left( \sqrt{J_{45}^2 + J_0^2} \right) + M \quad (2.13)$$

The spherical power S produced by the analysis software was compared with the power of the trial lens. For each trial, a graph was plotted between the spherical power obtained from the software with respect to the power of the trial lens. The plot was linear which indicated that the system was calibrated. Figure 2.8 shows the linear fits for the three trials (Trials 1-3).

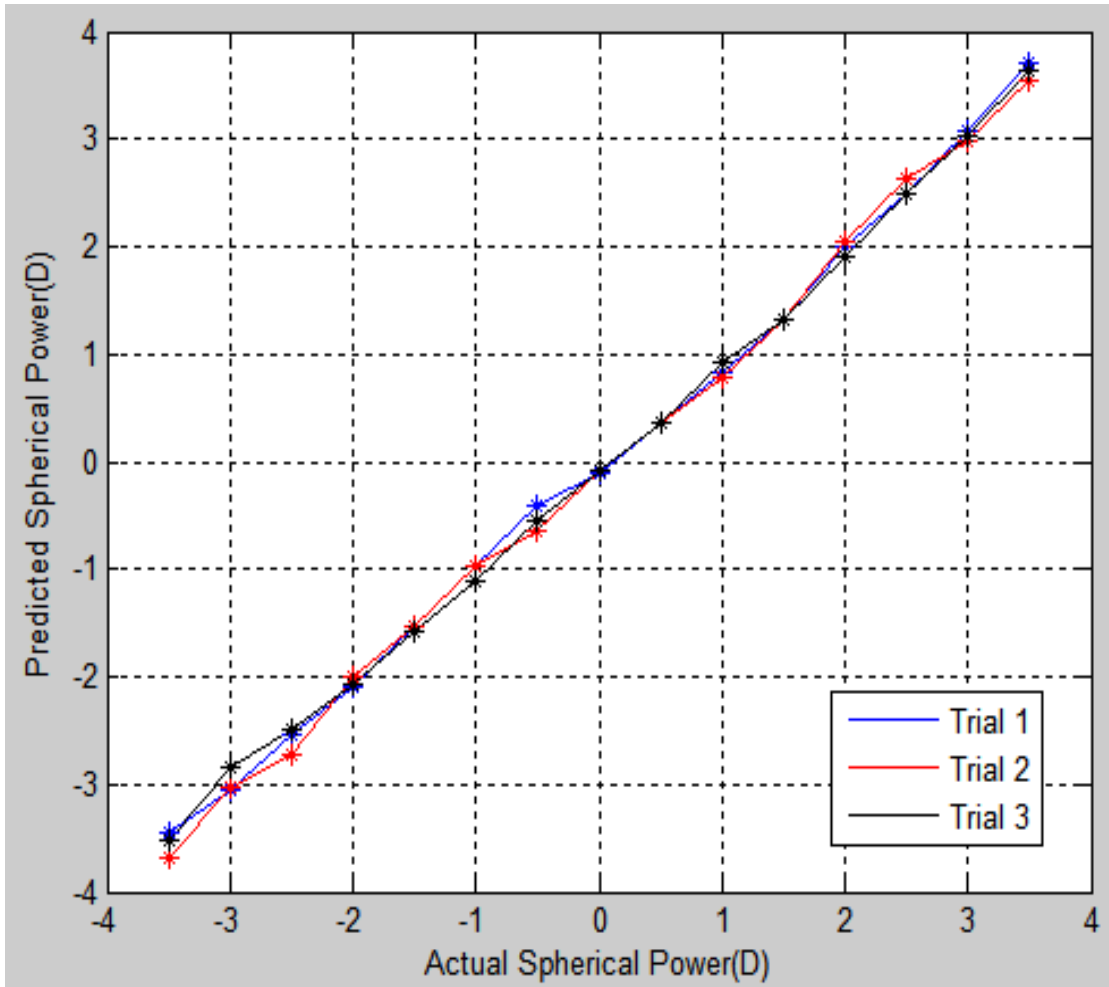


Figure 2.8. Plots of spherical power estimated from the SH image against the actual power of the trial lens inserted in front of the model eye.

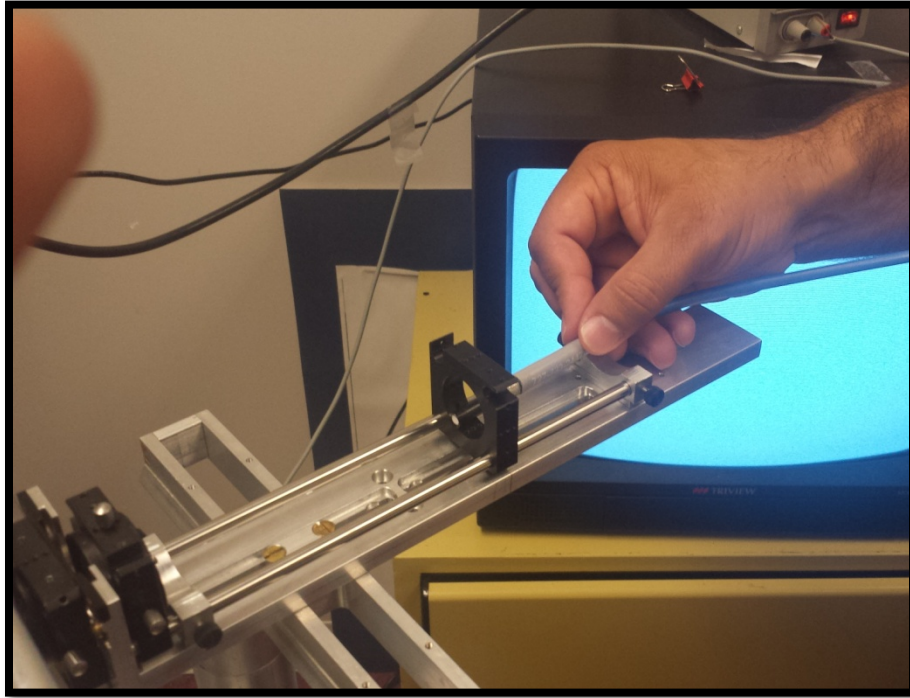


Figure 2.9. The head of the spectrometer is held at the focal point of the retina of the model eye.

## 2.6 Safety

Measurement of the peak absolute irradiance of the beam entering the model eye was done using the USB 2000 + XRI-ES spectrometer (Ocean Optics and Ocean View software interface). Firstly, a new file using the “Photometry, Photons, Power and Energy wizard” was started and a new absolute irradiance measurement process was initiated. Since the laser in this setup is 780nm, the integration region was specified as 760nm to 800nm and the measurement was set to be averaged over 3 trials. The spectroradiometer was calibrated in compliance with the National Institute of Standards and Technology recommended practices by Ocean Optics [44] (Dr. Jeff Hovis, Associate Professor of School of Optometry and Vision Science, University of Waterloo; Personal communication, [January 28, 2016]). Then, when all the parameters were set up, the head of the spectrometer was placed at a distance

equal to the focal length of the model eye (130mm) as shown in Figure 2.9. The precise position of the probe was located by observing a peak in the absolute irradiance spectrum at the 780nm wavelength (Figure 2.10), and the readings were taken while the spectrometer head was steadily held at that position.

Sufficient time was allocated for warming up the device before the readings were taken. Over several readings, we observed that the peak irradiance of our laser was, on average, 453  $\mu\text{W}/\text{cm}^2$ . The ANSI Z136.1 standard provides the maximum permissible exposure (MPE) that describes the level of irradiance, for a given wavelength/laser type and exposure time, beyond which damage to the eye is likely to occur [40]. The laser safety issue was addressed by ensuring that the corneal irradiance was under  $0.5 \text{ mW}/\text{cm}^2$ , which is far below the recommended ocular MPE limit of  $1.45 \text{ mW}/\text{cm}^2$  for exposure durations of 10s to  $3 \times 10^4$ s [40]. The measured absolute irradiance value of  $0.453 \text{ mW}/\text{cm}^2$  at the retina of the model eye indicates that the apparatus is well within the safety limits.



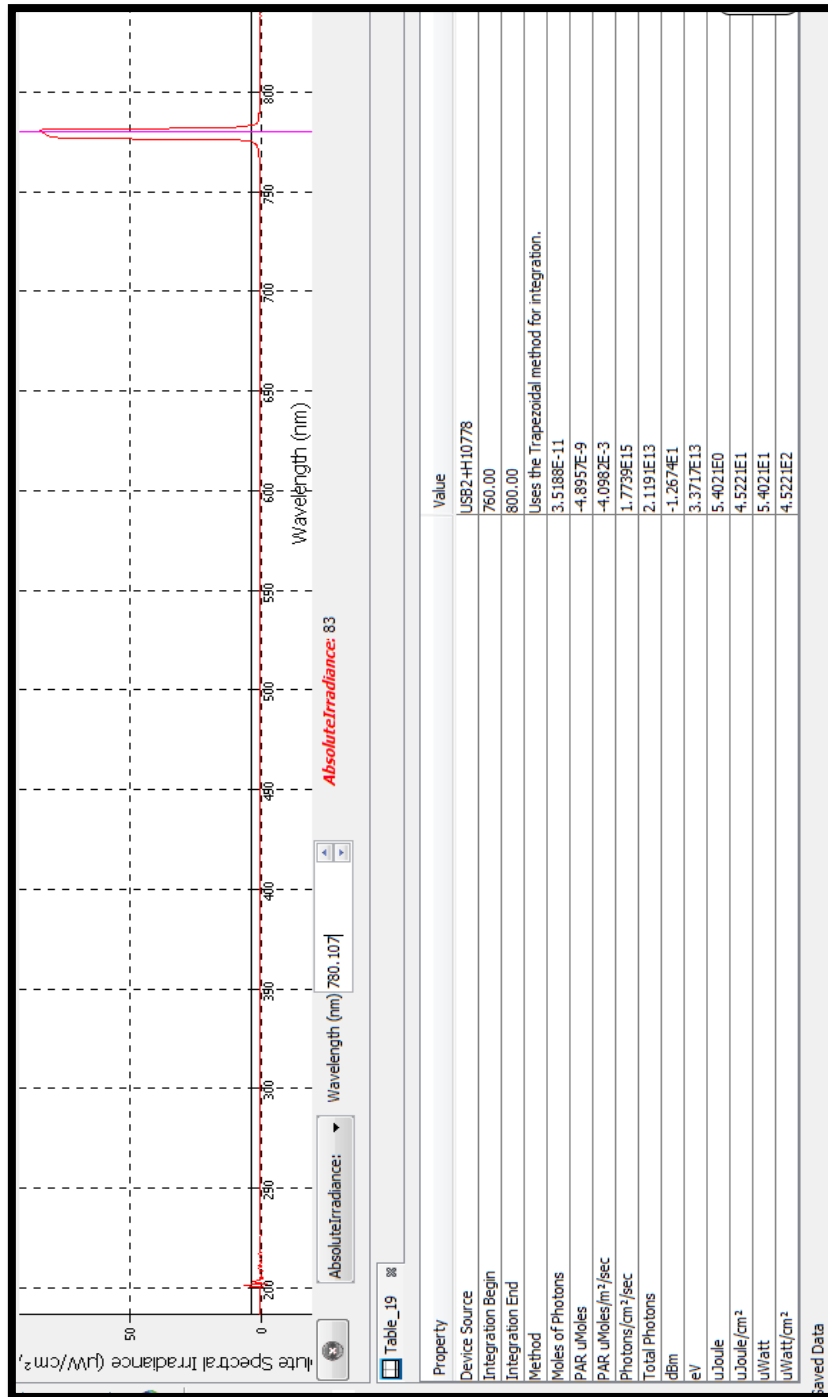


Figure 2.10. Screenshot showing the peak of the light source and measured absolute irradiance of  $452\mu\text{W}/\text{cm}^2$ .

## **Chapter 3**

### **Comparison of centroid estimation methods for wavefront aberration measurement**

#### **3.1 Introduction**

The accuracy of the estimation of optical aberrations by measuring the distorted wavefront using the SH wavefront sensor is mainly dependent upon the measurement accuracy of the centroid of the focal spot. The most commonly used methods for centroid estimation such as the brightest spot centroid; first-moment centroid; the weighted center of gravity and intensity weighted center of gravity, are generally applied on the entire individual sub-apertures of the lenslet array. However, these processes of centroid estimation are sensitive to the influence of reflections, scattered light, and noise in the SH image [45], especially in the case where the signal spot area is smaller compared to the whole sub-aperture area.

In this chapter, I give a performance comparison of the commonly used centroiding methods on the estimation of optical aberrations. A comparison of different centroid estimation methods with and without the use of some pre-processing steps (thresholding, Gaussian smoothing, and adaptive windowing) in a human eye mode is also discussed. We show that the use of any simple centroiding algorithm is sufficient in the case of ophthalmic applications for estimating aberrations within the typical clinically acceptable limits of quarter Diopter margins when certain pre-processing steps to reduce the impact of external factors are used. Some of the results were presented in the SPIE conference, San Francisco, California, United States (Ophthalmic Technologies XXVI, 2016) [46].

## **3.2 Methods**

Centroid estimation is a crucial step in the determination of wavefront aberration. The simplest way to estimate the centroid is by picking the brightest pixel of the spot [46]. The more popular way to find the centroid is to use the first moment or the center of mass for the entire sub-aperture of the individual microlenses. However, these processes of centroid estimation are sensitive to external factors such as reflections, scattered light, and noise, particularly in the case when the signal spot area is smaller compared to the whole sub-aperture area [47]. In this study, a human eye model was used for data collection, that emulated myopic and hypermetropic defocus values up to  $\pm 1.0\text{D}$  in steps  $0.5\text{D}$ , and the data was collected from our custom-made ophthalmic aberrometer (see Chapter 2).

### **3.2.1 Brightest spot center (BSC)**

This is an elementary way to estimate the centroid location in the focal spot. The brightest pixel or the pixel with the highest intensity in the focal spot corresponds to the centroid of the focal spot. Since in most cases the focal spot has a Gaussian-like intensity distribution around the centroid, this can be used to locate the centroid. This works best when the noise has a lower intensity profile and the peak noise intensity is less than the peak signal intensity.

### **3.2.2 Center of mass/gravity**

The first image moment method or the center of mass (CoM) calculates the centroid location as the weighted mean of the position coordinates  $(x_c, y_c)$ , the weight being the spot intensity as a function of position coordinates  $(x, y)$ . The centroid, of a single sub-aperture spot pattern, is evaluated using:

$$(x_c, y_c) = \left( \frac{\sum(I(x, y) * x)}{\sum(I(x, y))}, \frac{\sum(I(x, y) * y)}{\sum(I(x, y))} \right) \quad (3.1)$$

where  $x_c$  and  $y_c$  denote the centroid locations along the x and y coordinate axes, and  $I(x, y)$  denote the intensity of the pixel located at  $(x, y)$  and  $x$  and  $y$  denote the location of the pixel. This is one of the most widely used methods of centroid estimation and is best suited to situations where the light intensity levels are sufficiently high, and the SNR is good; however, this method is highly sensitive to noise.

### 3.2.3 Weighted center of gravity (WCoG)

The mathematical form that is assumed for the shape of the spot is called the weighting function  $W(x, y)$ , and is multiplied with the intensity function before applying the center of the mass algorithm as previously discussed. The estimated centroid location becomes:

$$(x_c, y_c) = \left( \frac{\sum(W(x, y) * I(x, y) * x)}{\sum(W(x, y) * I(x, y))}, \frac{\sum(W(x, y) * I(x, y) * y)}{\sum(W(x, y) * I(x, y))} \right) \quad (3.2)$$

In this case,  $W(x, y)$ , the weighting function is chosen to be a Gaussian kernel so that, the scattered noise around the peripheries has less effect on the estimation of the centroid position.

### 3.2.4 Intensity-weighted center of gravity (ICoG)

The intensity-weighted center of gravity (ICoG) is similar to WCoG with the difference being that the weighting function,  $W$ , is a power of the intensity distribution of the spot pattern,  $I$ . Hence, in ICoG, the estimated centroid position becomes:

$$(x_c, y_c) = \left( \frac{\sum(I(x, y)^\alpha * x)}{\sum(I(x, y)^\alpha)}, \frac{\sum(I(x, y)^\alpha * y)}{\sum(I(x, y)^\alpha)} \right) \quad (3.3)$$

Where  $\alpha$  determines the weighting given to intensity and a higher power of alpha implies greater importance to high-intensity pixels. A value of 3 for alpha is used in this analysis following the work by Baik et al. [48]. In comparison to the CoM method, this algorithm should perform better under low light level conditions, and low background and readout noise as it gives greater priority for high-intensity spots and is less sensitive to the low-intensity speckled noise due to reflections and diffraction prominent around the peripheries. The above statistical algorithm for centroid estimation tends to offer reasonable sub-pixel accuracy while being computationally less intensive [48].

### 3.3 Shack-Hartmann image collections

The SH images were obtained from the CCD sensor and stored in a Macintosh computer using iMovie 10.0 software and then processed, the methods used were those described in Chapter 2.4. The data collected for each set included the images of the SH spots captured for model eye defocused from  $-1.0\text{D}$  to  $+1.0\text{D}$  in intervals of  $0.5\text{D}$ . The aberrometer records data at a rate of 4 frames per second. These frames are then averaged to improve the accuracy of the system by reducing the speckle noise.

The images were processed following the outline mentioned. The spherical defocus values are calculated from the Zernike coefficients as given below:

$$S = -\frac{4\sqrt{3}}{r^2}C_4 + \sqrt{\left(-\frac{2\sqrt{3}}{r^2}C_3\right)^2 + \left(-\frac{2\sqrt{3}}{r^2}C_5\right)^2} \quad (3.4)$$

where  $r$  denotes the pupil radius [43].

### 3.4 Results

Spherical defocus values using the different centroiding algorithms, with and without the use of the pre-processing methods, were calculated. Table 3.1 gives the estimated spherical defocus when the different centroiding methods are used on raw images and Table 3.2 gives the estimated spherical defocus when different centroiding methods are used on pre-processed images.

Figures 3.1 shows the multiple bar diagrams of the spherical defocus results calculated using BSC, CoM, ICoG, and WCoG, respectively, without pre-processing SH images at different defocus values. Linear plots between the estimated defocus values and the actual defocus for BSC, CoM, ICoG, and WCoG are shown in Figure 3.2. The dotted line shows the expected plots between the estimated and actual defocus. The parameters of the fitted line, such as slope, y-intercept, and goodness of the fit  $R^2$  is shown in Table 3.3. Errors between the estimated defocus and actual defocus were calculated for all the centroid estimation methods (Table 3.1) and the average error was also calculated. The ICoG method shows the smallest error 0.1322D, followed by BSc= 0.1619D, WCoG =0.2885 and CoM=0.3547D.

The multiple bar diagrams of the spherical defocus values calculated using BSC, CoM, ICoG, and WCoG centroid estimation methods after applying pre-processing methods are shown in Figure 3.3. Linear plots between the estimated spherical defocus and actual defocus are shown in Figure 3.4. The dotted line shows the expected plots between the estimated and actual defocus. Table 3.4 shows the parameters of the fitted line, such as slope, y-intercept, and goodness of the fit  $R^2$ . Errors between the estimated defocus and actual defocus values

were also calculated and shown in Table 3.2. The average errors between the methods BSC, CoM, ICoG, and WCoG are comparable after removing the noises from the raw images, BSc= 0.1675 D, CoM=0.1542D, WCoG =0.1538 and ICoG=0.1538.

Table 3.1. Comparison of different centroid estimation method without the pre-processing methods. The absolute errors were calculated by subtracting the estimated defocus from the actual defocus.

Actual Defocus (D)	Results from raw images							
	BSC		CoM		WCoG		ICoG	
	Defocus	Error	Defocus	Error	Defocus	Error	Defocus	Error
-1	-0.95218	0.0478	-0.67875	0.3213	-0.65885	0.3411	-0.71955	0.2804
-0.5	-0.73624	0.2362	-0.36703	0.1330	-0.35451	0.1455	-0.52972	0.0297
0	-0.18463	0.1846	0.379915	0.3799	0.359663	0.3596	-0.14618	0.1462
0.5	0.238225	0.2618	1.158279	0.6583	0.972031	0.4720	0.670321	0.1703
1	0.920827	0.0792	1.281183	0.2812	1.124245	0.1242	1.034609	0.0346
Average Error	0.1619		0.3547		0.2885		0.1322	

Table 3.2. Comparison of different centroid estimation method with the pre-processing method. The absolute errors were calculated by subtracting the estimated defocus from the actual defocus.

Actual Defocus (D)	Results from raw images							
	BSC		CoM		WCoG		ICoG	
	Defocus	Error	Defocus	Error	Defocus	Error	Defocus	Error
-1	-1.03696	0.0370	-1.07056	0.0706	-1.0712	0.0712	-1.0607	0.0607
-0.5	-0.66854	0.1685	-0.6699	0.1699	-0.67009	0.1701	-0.66979	0.1698
0	-0.24491	0.2449	-0.22147	0.2214	-0.22093	0.2209	-0.22119	0.2211
0.5	0.251834	0.2482	0.284788	0.2152	0.284201	0.2158	0.285978	0.2140
1	0.861102	0.1389	0.906341	0.0937	0.909152	0.0908	0.89675	0.1032
Average Error	0.1675		0.1542		0.1538		0.1538	

Table 3.3. Parameters of the linear fits in figure 3.1.

Methods	Slope	y-intercept	R <sup>2</sup>
BSC	0.9441	-0.1428	0.9750
CoM	1.0890	0.3547	0.9584
WCoG	0.9785	0.2885	0.9646
ICoG	0.9417	0.0619	0.9554



Table 3.4. Parameters of the linear fits in figure 3.2.

Methods	Slope	y-intercept	R <sup>2</sup>
BSC	0.9433	-0.1675	0.9901
CoM	0.9817	-0.1542	0.9925
WCoG	0.9830	-0.1538	0.9923
ICoG	0.9741	-0.1538	0.9925

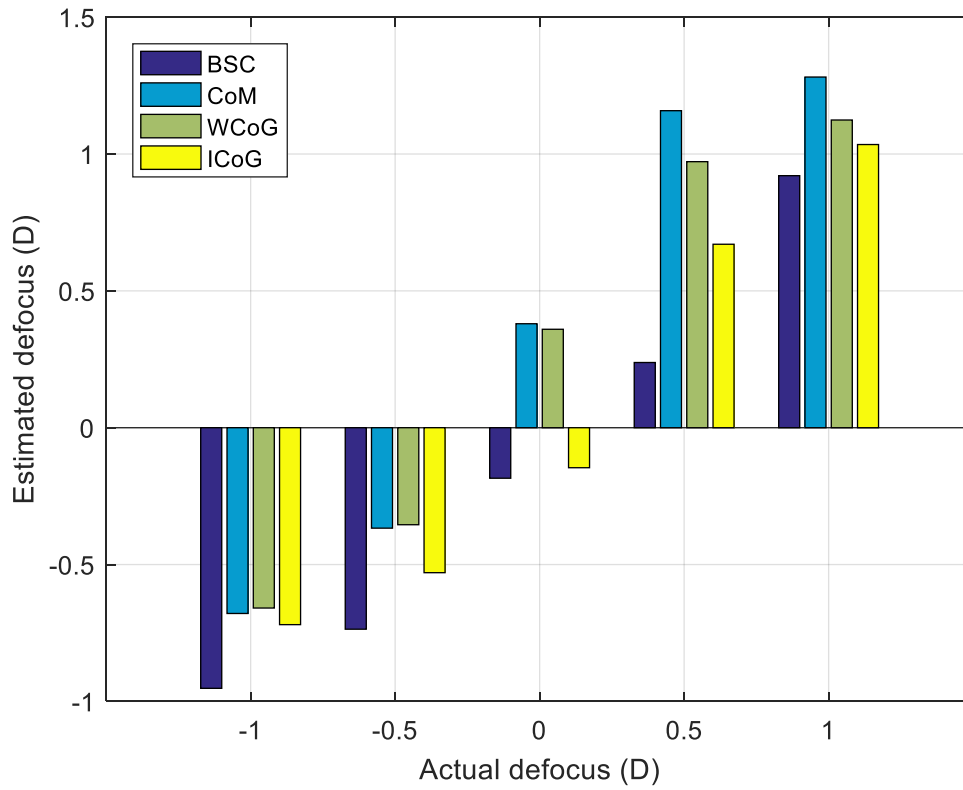


Figure 3.1: Plots of the estimated spherical defocus with respect to the actual defocus calculated by using BSC, CoM, ICoG and WCoG centroid estimation methods, respectively, on raw images without applying pre-processing steps.

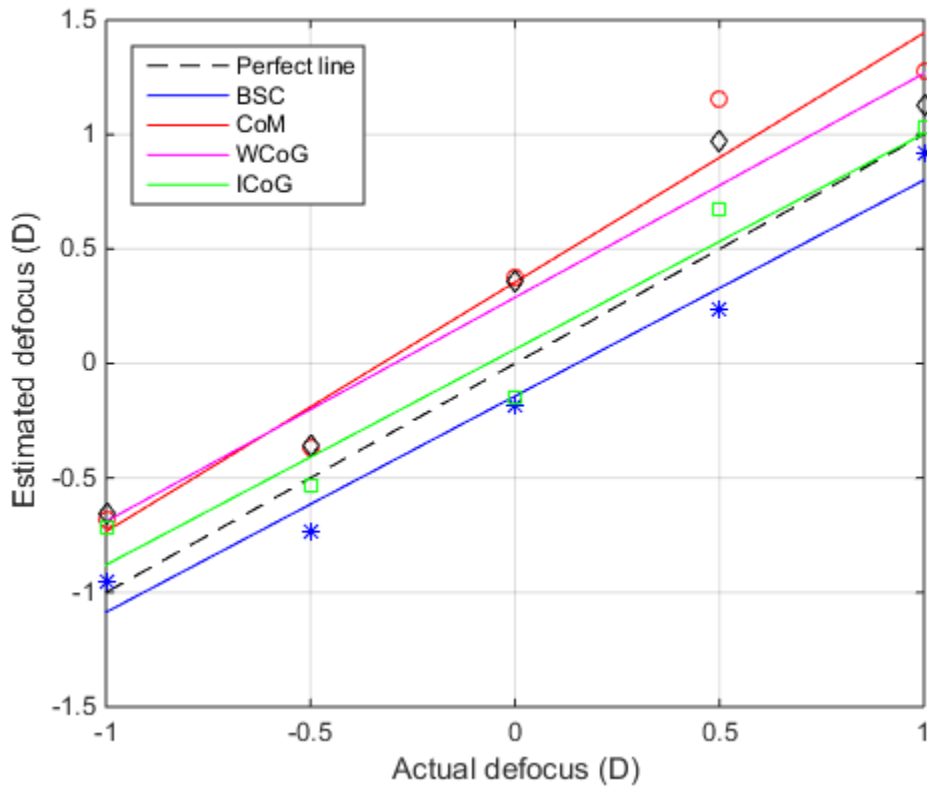


Figure 3.2. Linear plots between estimated spherical defocus and actual defocus calculated by using BSC, CoM, ICoG, and WCoG centroid estimation methods, respectively, on raw images without applying pre-processing steps. The dotted line shows the expected spherical defocus values with respect to the actual defocus values.

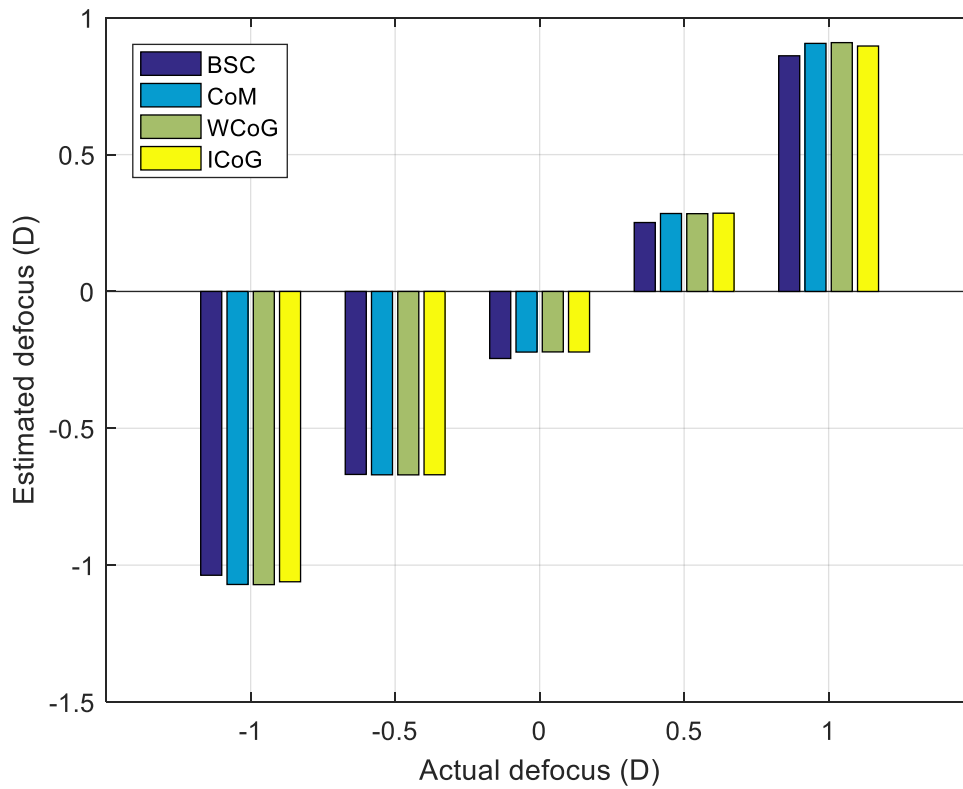


Figure 3.3. Plots of the estimated spherical defocus with respect to the actual defocus obtained from centroid estimation methods, BSC, CoM, ICoG, and WCoG, respectively, after applying pre-processing steps to raw images.

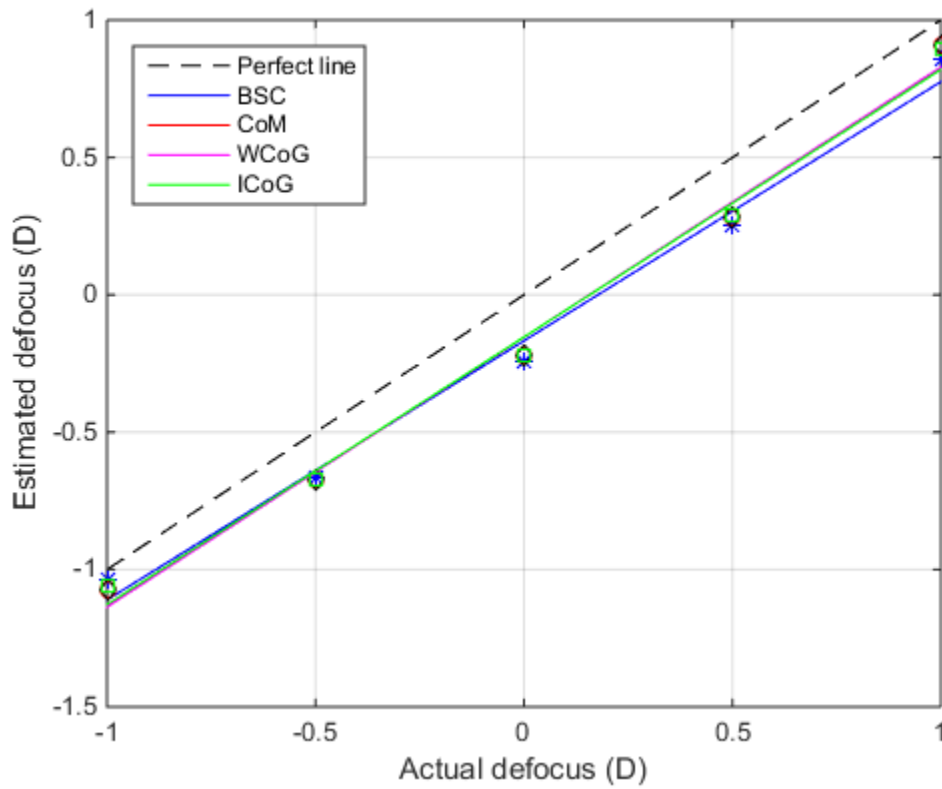


Figure 3.4. Linear plots between estimated spherical defocus and actual defocus calculated by using BSC, CoM, ICoG, and WCoG centroid estimation methods, respectively, after applying pre-processing methods to raw images. The dotted line shows the expected spherical defocus values with respect to the actual defocus.

### 3.5 Conclusions

The results show that the spherical defocus values calculated from all the centroid estimation methods are within  $\pm 0.25D$  margin of the actual defocus when the raw images were smoothed, thresholded and processed using a dynamic window. It can clearly be observed that by using these pre-processing routines the resulting outcomes from the use of different centroiding algorithms follow a close linear trend. It can also be seen that the use of the different centroiding algorithms results in similar estimation for the aberration if the images are pre-processed.

Estimated spherical defocus of raw images, for higher values of defocus were adversely affected, giving completely erroneous results for the CoM and WCoG methods. This is because higher myopic defocus values blur out spots and spread them over larger areas. Algorithms that give weight to intensity perform better than other algorithms in that case and the intensity weighted center of gravity method is more robust amongst them.

The pre-processing routine used helps improve the performance of the centroiding methods and makes the procedure more robust. The main step that results in a drastic improvement of the results is an appropriate thresholding step, making it the single most crucial pre-processing step. The adaptive windowing is to ensure that the processing area is minimized resulting up to threefold faster processing. These pre-processing steps not only make the results reliable but also help minimize the effect of external factors like reflections, scattered light, and noise. The sensitivity to external factors that affect different algorithms in different ways is minimized by use of the pre-processing routines, making it feasible to use any centroiding algorithm of choice.

In the case of ophthalmic applications, use of any simple centroiding algorithm seems to be sufficient for estimating sphere (2<sup>nd</sup> order aberrations) within the typical clinically acceptable limits of quarter Diopter margins, when the suggested pre-processing steps are used to mitigate the impact of external factors.

## Chapter 4

### Pupil scaling for the estimation of aberration in natural pupils

#### 4.1 Introduction

Most clinical aberrometers use Zernike polynomials to report the wavefront aberrations of the eye [31-32]. As mentioned in Chapter 2, the Zernike polynomials are a set of orthogonal basis functions over a circle of unit radius and are suitable for accurately describing wavefront aberration of an optical system [33].

A major issue when using Zernike polynomials is that they are pupil size dependent (since they are normalized to pupil radius), and therefore, the magnitude of Zernike coefficients changes when pupil size changes. This requires special consideration when measurements from different instruments or participants are compared [31] in order to prevent ambiguous conclusions. This is especially important when the measurements are used for clinical applications such as laser refractive surgery [49]. Normally, one determines the Zernike coefficients for a common pupil size. The algorithm employed in an aberrometer uses a large number of sensor elements for calculating the aberrations for a large pupil size and use a smaller number of sensor elements for the smaller pupil. Alternative methods to calculate the Zernike coefficients from a fixed number of sensors employing mathematical pupil size scaling techniques to estimate the Zernike coefficients at various pupil sizes have also been proposed [50-58]. Pupil scaling is a mathematical procedure by which the measured Zernike coefficients for a larger pupil size are estimated for a smaller pupil size and vice versa. Some studies [59-60] have adapted this technique for predicting wavefront aberration measurements for different pupil sizes.



Several recent studies have examined the relationship between refractive error and Zernike coefficients of HOA and have used pupil size scaling to scale the aberrations to a common pupil size, smaller than the natural pupil size [59-60]. However, their research questions did not examine the pupil scaling technique itself. The scaling approach may provide a more accurate estimation of wavefront aberration since it uses a larger set of sensor elements to extract Zernike coefficients. It has also been reported that data scaled for pupil size shows greater repeatability of the Zernike coefficients than Zernike coefficients derived only from the sensors contained within a given pupil size [49]. Since there is no validation of pupil scaling methods with clinical data, in this chapter I report the comparison of estimates of Zernike coefficients with corresponding clinical measurements obtained at different pupil sizes. Some of the results were presented in the Journal of Optometry and Vision Science [61]

## **4.2 Methods**

The study reviewed measurements taken with i.Profiler® plus aberrometer (Carl Zeiss Vision, USA) in one of a battery of tests performed at the initial screening visit of a separate clinical study, for which the pupil scaling procedure was not a research question. Ocular wavefront aberrations of 156 presbyopic subjects were reviewed for this experiment. A total of 28 subjects (mean age  $57 \pm 7$  yrs.) whose pupil size  $\geq 5$  mm were selected in order to examine the pupil size scaling method. The subjective spherical equivalents for right eyes of the participants ranged from -10.50 D to +2.38D (mean  $\pm$  SD:  $-1.43 \pm 3$  D). The maximum natural pupil sizes varied among individuals and eyes and we included only those individuals

with pupil size  $\geq 5$  mm. The mean mesopic natural pupil size of the sample was 5.39mm and ranged between 5.00mm and 6.26mm. None of the participants had measurements taken with a pupil that had been dilated using a therapeutic pharmaceutical agent (i.e. a mydriatic or cycloplegic drop). Also, none of the participants had undergone previous refractive surgery or suffered from any ocular pathology. The research followed the tenets of the Declaration of Helsinki; informed consent was obtained from the subjects after explanation of the nature and possible consequences of the study. The study, including all measurement procedures, was reviewed by and received ethics clearance through the Office of Research Ethics at the University of Waterloo.

The i.Profiler® plus aberrometer, which is based on the SH principle ( $\lambda_{Ref}=555\text{nm}$ ; Maximum number of sensors 1500), was used to measure the wavefront aberrations under mesopic conditions up to the 7<sup>th</sup> order for the maximum natural pupil diameter and the device also provides corresponding data for a 3mm pupil. It has the capability of obtaining measurements for pupil sizes of 2-7mm. The measuring range of the wavefront sensor is from -20DS to +20DS for a 3.5 mm pupil size and -15DS to +15DS for a 5.5 mm pupil size, and up to 8DC. In our study the measured data consisted of Zernike coefficients obtained from the sensors within a 3mm pupil diameter and those obtained from the sensors within the maximum mesopic natural pupil; both data sets were obtained directly from the subset of spots in the SH image and this was confirmed with the iProfiler manufacturer. (Meister D, Manager, Technical Marketing Carl Zeiss Vision, Inc. personal communication, [January 28, 2014]). All measurements were obtained with a room illumination of approximately 50 lux to allow for natural pupil dilation. During the measurement process, the participants placed their

chin on the chin rest and fixated on a target that served as an accommodative control during the measurement period. The instrument automatically aligns the participant's pupil center with the optical axis of the device before measurement acquisition. Measurements were obtained for each eye separately for all participants and the test typically took 30 seconds to complete for both eyes. However, we only used measurements from the right eyes of the participants in this study.

In general, the wavefront aberration  $W(r, \theta)$  is represented as a linear combination of Zernike polynomials:

$$W(r, \theta) = \sum_{n,m} C_n^m Z_n^m(r/r_{max}, \theta) \quad (4.1)$$

Where  $Z_n^m$  are the Zernike polynomials and  $C_n^m$  are their corresponding coefficients. The indices  $n$  and  $m$  represent the radial order and azimuthal frequency of the azimuthal component, respectively. Similarly,  $r$  and  $\theta$  are the variables of the polar coordinate system and  $r_{max}$  is the maximum radial extent of the pupil. The  $r_{max}$  of different eyes or the same eye at different conditions are different so the measurements (i.e. Zernike coefficients) with different pupil sizes cannot be directly compared [51]. Let  $a_n^m$  and  $b_n^m$  be the Zernike coefficients at pupil radius  $r_1$  and  $r_2$ , respectively for the same wavefront aberration  $W(r, \theta)$ , such that:

$$W(r, \theta) = \sum_{n,m} a_n^m Z_n^m(r/r_1, \theta) \quad (4.2)$$

$$W(r, \theta) = \sum_{n,m} b_n^m Z_n^m(r/r_2, \theta) \quad (4.3)$$

The goal of the pupil scaling technique is to calculate Zernike coefficients ( $b_n^m$ ) for a pupil diameter  $r_2$  from the measured Zernike coefficients ( $a_n^m$ ) for a pupil diameter  $r_1$ . Schwiegerling [51] solved this problem by expressing  $b_n^m$  in terms of  $a_n^m$ ,  $r_1$  and  $r_2$  using algebraic techniques.

In this study, pupil scaling as described by Schwiegerling [51] were implemented in MATLAB software version (R2010b, MathWorks, Natick, USA) using the source code published by Ginis et al. [49] Zernike coefficients were estimated for a 3mm pupil size using the measured data from the maximum natural pupil size to provide the ‘scaled down estimate’. The corresponding Zernike coefficient estimates for the maximum pupil size, using the measured data from the 3mm pupil size, provided the ‘scaled up estimate’. The estimated coefficients were then compared with the measured data. Second, third and fourth order Zernike coefficients were used for the analysis.

The data obtained directly from the aberrometer (measured) and the estimated data obtained from the pupil scaling technique were compared. The measured data was taken to be the ‘true’ value of the Zernike coefficients. A repeated measures ANOVA was used to evaluate overall differences between estimated and measured Zernike coefficients (Contrasts: Method (Measured vs Estimated) and Order (Lower vs Higher)). For all analyses,  $\alpha$  values  $\leq 0.05$  were considered statistically significant. Paired t-tests were then used to evaluate individual measured and estimated coefficients, with Holm correction for multiple comparisons. Plots of the error versus the measured coefficients were obtained for the second, third and fourth order Zernike coefficients and the limits of agreement ( $1.96 \times$  sample standard deviation) were determined. The percentage of the absolute error to the absolute mean for each

coefficient was also determined. All data analyses were carried out in the statistical program R (v. 3.0.2) [62].

### 4.3 Results

There was no significant difference between the overall estimated and measured Zernike coefficients for scaling up from the 3mm measured data to the maximum mesopic natural pupil size or for scaling down from the maximum mesopic natural pupil size to the 3mm (RM-ANOVA; both  $p > 0.5$ ). There was a significant difference in the lower and higher order coefficients (RM-ANOVA; both  $p < 0.001$ ), but this was not different between the estimated and measured methods of obtaining the coefficients (RM-ANOVA; Method\*Order; both  $p > 0.5$ ). In the pairwise comparison of each coefficient, there were no significant differences for any coefficient (corrected paired t-test; all  $p > 0.05$ ).

Pearson correlation coefficients between the estimated and measured Zernike coefficients when scaling up from a 3mm pupil size ranged between 0.979 and 0.999, 0.695 and 0.899, and 0.734 and 0.898 for the 2<sup>nd</sup>, 3<sup>rd</sup> and 4<sup>th</sup> order Zernike coefficients, respectively. When scaling down from the maximum pupil size, Pearson correlation coefficients ranged between 0.997 and 0.999, 0.962 and 0.984, and 0.720 and 0.891 for the 2<sup>nd</sup>, 3<sup>rd</sup> and 4<sup>th</sup> order Zernike coefficients, respectively.

Figure 4.1 shows the error between the estimated and measured 2<sup>nd</sup> order Zernike coefficients as a function of the magnitude of the measured coefficients. Corresponding data for the 3<sup>rd</sup> and 4<sup>th</sup> order coefficients are shown in Figures 4.2 & 4.3. For all coefficients, the mean error was centered at approximately zero for both scaling up and scaling down by the pupil scaling

procedure (Table 4.1). The widths of the limits of agreement and the absolute percentage error were larger when the coefficients were determined by scaling up from measured data of a 3mm to a larger pupil size than when scaling down from measured data of the larger pupil size to 3mm (Table 4.1).

When scaling down, the data exhibited systematically smaller Zernike coefficients irrespective of whether the coefficient was positive or negative, as illustrated by the long axis of the 95% confidence ellipse being tilted positively away from horizontal (Figures 4.1-4.3). No such clear, systematic error was observed when the estimates of the Zernike coefficients were obtained by scaling up from the measured 3mm pupil data. There was no significant correlation between the magnitude of the difference between the measured and estimated coefficient and the pupil size, irrespective of whether the estimated coefficient was scaled up or down.

Table 4.1. Mean error and limits of agreement for the difference between the estimated and measured coefficients for each pupil scaling procedure.

Coefficient	Measured 3mm Pupil	Measured Maximum Pupil
	Absolute Mean±SD (Range)	Absolute Mean±SD (Range)
$C_2^{-2}$	0.0907±0.1357 (-0.3580 to +0.4070)	0.2496±0.3962 (-1.1466 to +1.0468)
$C_2^0$	0.7935±0.9360 (-0.7960 to +2.9550)	2.6547±3.0755 (-2.4901 to +10.1160)
$C_2^2$	0.1685±0.2202 (-0.5270 to +0.3650)	0.5233±0.6634 (-1.4320 to +1.4993)
$C_3^{-3}$	0.0345±0.0423 (-0.0960 to +0.1040)	0.1439±0.1785 (-0.4969 to +0.4016)
$C_3^{-1}$	0.0268±0.0394 (-0.1300 to +0.0910)	0.1269±0.1900 (-0.7477 to +0.1964)
$C_3^1$	0.0256±0.0354 (-0.0930 to +0.0640)	0.0944±0.1142 (-0.2589 to +0.2262)
$C_3^3$	0.0261±0.0374 (-0.0950 to +0.0980)	0.0952±0.1418 (-0.3663 to +0.2895)
$C_4^{-4}$	0.0068±0.0082 (-0.0140 to +0.0170)	0.0473±0.0546 (-0.0887 to +0.1516)
$C_4^{-2}$	0.0052±0.0066 (-0.0170 to +0.0130)	0.0301±0.0379 (-0.0761 to +0.0784)
$C_4^0$	0.0136±0.0118 (-0.0140 to +0.0290)	0.1391±0.0954 (-0.0573 to +0.3115)
$C_4^2$	0.0074±0.0092 (-0.0200 to +0.0190)	0.0451±0.0595 (-0.1391 to +0.1200)
$C_4^4$	0.0077±0.0098 (-0.024 to +0.0170)	0.0583±0.0644 (-0.0979 to +0.1559)

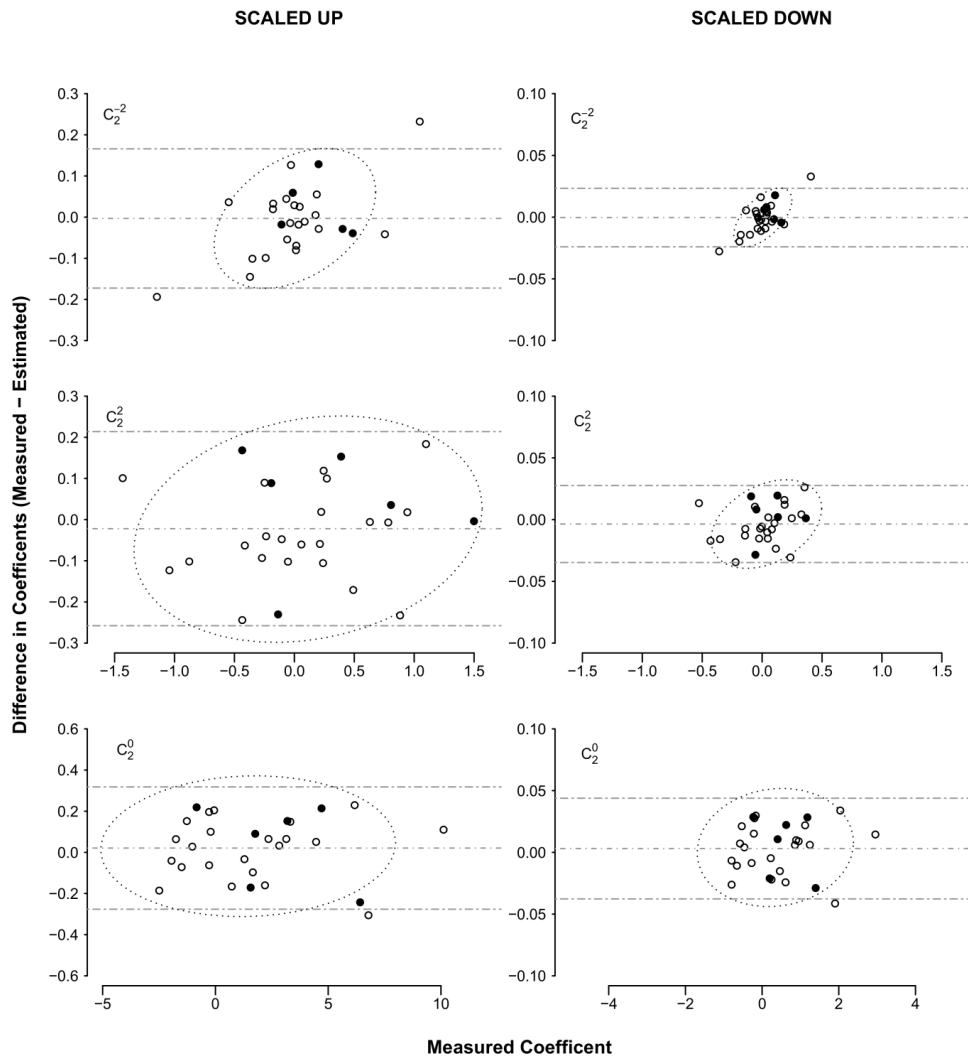


Figure 4.1. The error between the measured and estimated 2<sup>nd</sup> order Zernike coefficients  $C_2^{-2}$  (top),  $C_2^2$  (middle) and  $C_2^0$  (bottom) for the pupil scaling procedures where data were scaled up from the measured 3mm data to the maximum pupil diameter (left panel) and scaled down from the maximum pupil size data to a 3mm pupil diameter (right panel). The dotted ellipse illustrates a robust 95% confidence interval for the data. Open symbols represent maximum pupil size <5.40mm and filled symbols represent pupil sizes >5.40mm. The dotted ellipse illustrates a robust 95% confidence interval for the data. Note the different scales for the ordinate axes of each panel and the abscissa for the bottom graphs.



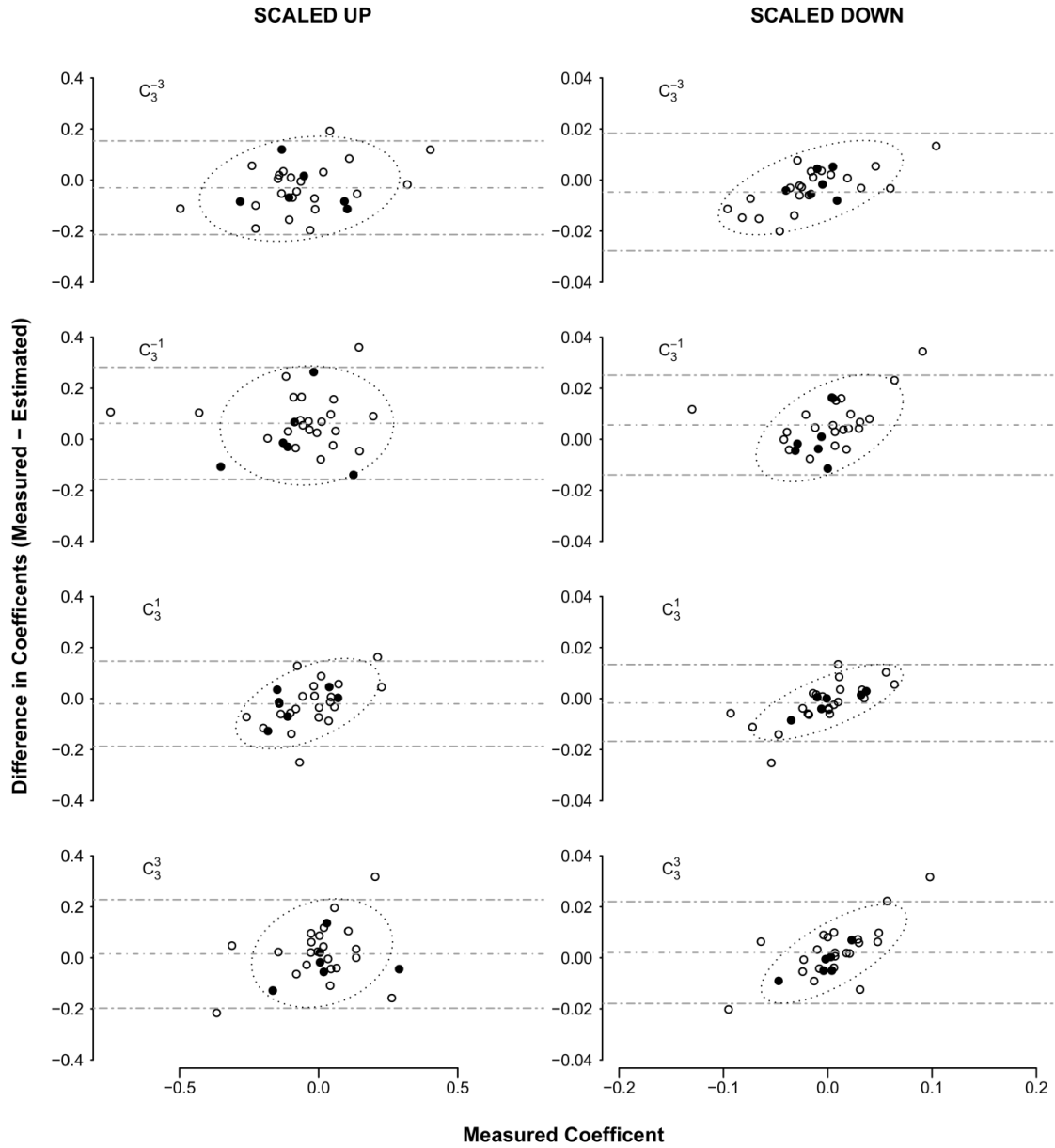


Figure 4.2. The error between the measured and estimated 3<sup>rd</sup> order Zernike coefficients  $C_3^{-3}$  (top),  $C_3^{-1}$  (upper middle),  $C_3^1$  (lower middle) and  $C_3^3$  (bottom) for the pupil scaling procedures where data were scaled up from the measured 3mm data to the maximum pupil diameter (left panel) and scaled down from the maximum pupil size data to a 3mm pupil diameter (right panel). Other details are as for Figure 4.1.

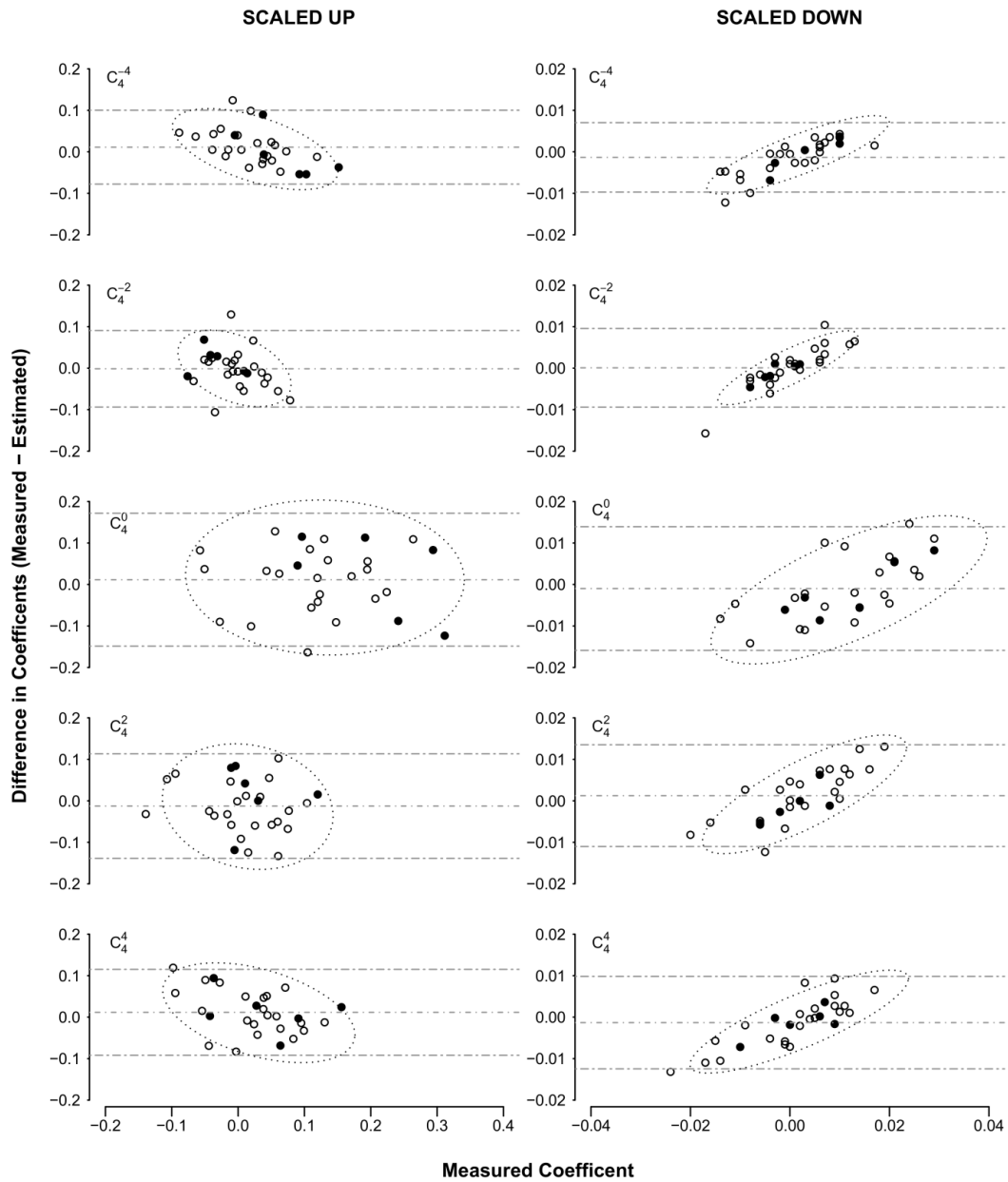


Figure 4.3. The error between the measured and estimated 4<sup>th</sup> order Zernike coefficients  $C_4^{-4}$  (top),  $C_4^{-2}$  (2<sup>nd</sup> row),  $C_4^0$  (3<sup>rd</sup> row),  $C_4^2$  (4<sup>th</sup> row) and  $C_4^4$  (bottom) for the pupil scaling procedures where data were scaled up from the measured 3mm data to the maximum pupil diameter (left panel) and scaled down from the maximum pupil size data to a 3mm pupil diameter (right panel). Other details are as for Figure 4.1.

#### **4.4 Discussion and conclusion**

This study describes a comparison of Zernike coefficients obtained directly from aberrometer and that estimated using a theoretical pupil scaling formula. There was good to the excellent correlation between the estimated and measured coefficients for all second, third and fourth order coefficients for both scaling up from a 3mm to a larger pupil and scaling down from a larger pupil to 3mm. The magnitude of the correlation generally reduced, in both scaling cases, as the coefficient order increased. Although the mean differences between the estimated and measured values for each mode were not significantly different in both the scaling up and scaling down conditions, the differences were always larger when the Zernike coefficients were scaled up from a 3mm to a larger pupil compared to the differences when scaling down to a 3mm pupil. Therefore, taking the direct measures of the Zernike coefficients as the ‘true’ estimate of the ocular aberrations, scaling down from a larger to a smaller pupil is more accurate than the converse.

Errors in pupil scaling from a smaller to a larger pupil may be a result of several factors. Since the sensors of the SH detector are in a regular, fixed spatial array the number of sensors contained within the ‘true’ 3mm pupil are far fewer than that contained within the ‘true’ maximum pupil size. Fitting the Zernike polynomials to the measured data from the 3mm pupil will, therefore, reduce the precision, and so introduce error, of the estimation of the coefficients both for 3mm and when used to scale up to a larger pupil size. In addition, the pattern of higher order coefficients shows greater variation at the margin of the scaled-up pupil size and there may not be sufficient information in the data from the central 3mm pupil to model this with precision. Our results indicate that this is the case; the scaled-up data

exhibit considerably less agreement with the measured values (Table 4.2). Indeed, Ginis et al. [49] found that repeated estimation of the Zernike coefficients for HOAs directly from the sensors within the 3mm pupil had relatively low SNR while scaling down from a larger pupil to a 3mm pupil did not. The noise may be minimized if a dynamic aberrometer is used instead of static to measure the aberrations and the coefficients are extracted by averaging multiple frames. Pupil scaling methods have been developed that deal with the scaled pupil being translated [60], rotated and non-circular [56-57] that can also contribute to inaccuracies in the estimation of Zernike coefficients, the methodology of this study assumed that there was no translation of the pupil center and was therefore unlikely to have contributed to the errors in estimation seen.

With the availability of aberrometers in a clinical setting, the findings of this study can be applied clinically, namely when clinicians need an estimation of Zernike polynomials for a fixed pupil size and the available aberrometer measures only a single, different pupil size. A previous, large study examined scaling up the pupil size from 5mm in 0.25mm increments, intending to examine the implications for error in the estimation of wavefront aberrations in the refractive surgery transition zone [63]. The study found that when making estimations from 5mm measured data for pupil sizes 5.75mm and larger, the level of RMS error was greater than the variability between repeated examinations. Similarly, Neal, Baer, and Topa [64] found a good agreement between the rescaled and measured data over a small scaling range. They also found that if the Zernike polynomials are a poor representation of the data, there will be large RMS fit error and hence large pupil scaling error [64]. Our findings, though scaled up  $\geq 2.0$ mm from the starting pupil size, show a similar trend.

Bará et al. [65] compared two pupil resizing methods: rescaling the Zernike coefficients using the measured data from the original pupil and refitting the wavefront slope measurements within the new pupil based on the measurement provided by the aberrometer. The results showed that rescaling generally provides better results when scaling down to the smaller pupil whereas the refitting works well when scaling up to the larger pupil [65]. The higher limit of agreements while scaling up the Zernike coefficients in our study is in agreement with Bará et al. [65]. The second implication of this study is in the retrospective analysis of large databases. Several studies have been published that examine the relationship between wavefront aberrations and refractive error [59-60]. In order to undertake meaningful between-subject comparisons, it is necessary to scale the data for each subject to the same pupil size and the pupil size should be large enough in order to generalize the analysis. Typically, this is achieved by excluding any datasets with pupil diameters smaller than a given, arbitrary, size. This might exclude a large percentage of a database; for example, in reference [59], 40% of a database was excluded when the pupil diameter was set to 3.5mm or larger. It would seem advantageous then to be able to scale up from smaller pupil sizes. However, our study demonstrates that although the scaling up procedure provides estimates that are not significantly different than their corresponding measured values, the estimates will have a greater amount of variability and will not exhibit a systematic error. Another approach to making between-subject comparisons is to ensure all measurements are obtained with a large pupil size by using a pharmacological agent to dilate the pupil. However, it has been shown that the average root-mean-square (RMS) of the HOAs is different in eyes using different cycloplegic drops [66].

In summary, the fact that Zernike coefficients are pupil size dependent impedes the direct comparison of coefficients measured by different instruments and laboratories or from different participants. The pupil scaling method can calculate the aberrations for a smaller pupil size based on the information from the maximum natural pupil size (scaling down), or vice versa (scaling up). The scaling down method provides a better estimate of the refractive state of the eye since it is not as impacted by large variations in the estimates, even though we found no significant difference between the measured and estimated coefficients over the range of pupils examined, irrespective of whether the estimates were made by scaling up from a small pupil or the converse.

## Chapter 5

### Wavefront aberration with missing Shack-Hartmann Spots

#### 5.1 Introduction

One problem with using SH images is that some of the spots may be absent from the acquired image. This could potentially impact the magnitude of the Zernike coefficient estimates. In a static model eye, there are several factors that may contribute to this problem: (a) alignment and calibration errors of the wavefront sensor, (b) sampling methods used to capture SH spots and, (c) uneven illumination on the lenslet array [67]. When obtaining aberration measurements for human eyes in vivo, spots may be missing from the SH images because of anomalies in the optics of the eye due to pathologies (such as cataract, optical opacities, tear film anomalies) or treatments (such as corneal shape, pseudophakia or other iatrogenic consequences of ocular surgery). In particular, missing SH spots or poor appearance of them has been noted as a likely issue when taking wavefront aberrometry measures in clinical situations [32] involving cataract or keratoconus [68].

Irrespective of why the spots are missing in an SH image, their absence may lead to the unreliable measurement of ocular aberrations. In this chapter, I took two approaches to examine the impact of missing spots on the estimates of the Zernike coefficients. First, this was tested by systematically deleting a fixed percentage/number of spots at random locations in the lenslet array from the original SH image and comparing the results with the aberration extracted from the original SH image in a model eye. In each instance, the Zernike coefficients were estimated for 0-80% deleted spots (in 10% increments) to simulate a series of abnormal SH images. Second, images were obtained with clusters of missing spots,

simulated on a plano spectacle lens, when imaging a human eye in vivo. This approach was intended to better reflect the situation where aberrometry measures are obtained from eyes with disease present that might give rise to missing spots. Some of the results were presented in the conference (Advances in Optical Sciences and Engineering New Delhi) [69].

## **5.2 Methods**

### **5.2.1 Missing spots in a model eye**

The custom-made aberrometer described in Chapter 2 was used for obtaining the images from the model eye. The SH images were subjected to pre-processing (as described in Chapter 3) including gray-level transformation followed by hard thresholding and adaptive windowing in order to reduce noise and artifacts. A minimum number of connected pixels (10 pixels in this study) were used as a threshold to distinguish between real SH spots and noise due to reflection in the dark background of the image. Zernike coefficients up to fifth order were calculated from the SH images.

Trial lenses with power ranging from -3.5 D to +3.5 D in 0.5D increments were placed in front of the model eye to simulate ametropia. The surface plots (Figure 5.1) reconstructed from the Zernike coefficients show the amount of total aberration present in the model eyes for different defocus conditions. To examine the impact on the measurement of ocular aberrations from a reduced number of spots in the SH image, 0 to 80% of SH spots were randomly deleted from each of the original images in steps of 10%. Since the Least Squares Fit method was used to reconstruct the wavefront, the number of spots required to calculate Zernike coefficients must be greater than the number of Zernike coefficients and care was



taken to ensure that the number of spots remained within these limits after deletion. The deletion was completely spatially random and was not intended to reflect any diseased eye models. The spots deletion was performed in the post-processing phase by creating a mesh which blocks a certain percentage of the spots at each time. The selection of spots was repeated 1000 times to simulate different patterns by changing the structure of the mesh for each defocus conditions. The average spherical defocus ( $\pm$  standard deviation) was calculated over a period of 1000 trials to compare with the power of the trial lens. When the spherical defocus of the missing model differed by  $\pm 0.25\text{D}$  from the power of the trial lens, we stopped further deletion of spots from the SH image. RMS of the total aberrations, RMS of HOA, Zernike coefficients, such as trefoil, coma, and spherical aberration were calculated to compare them at different missing models. The pupil size was fixed to 3mm for all calculation.

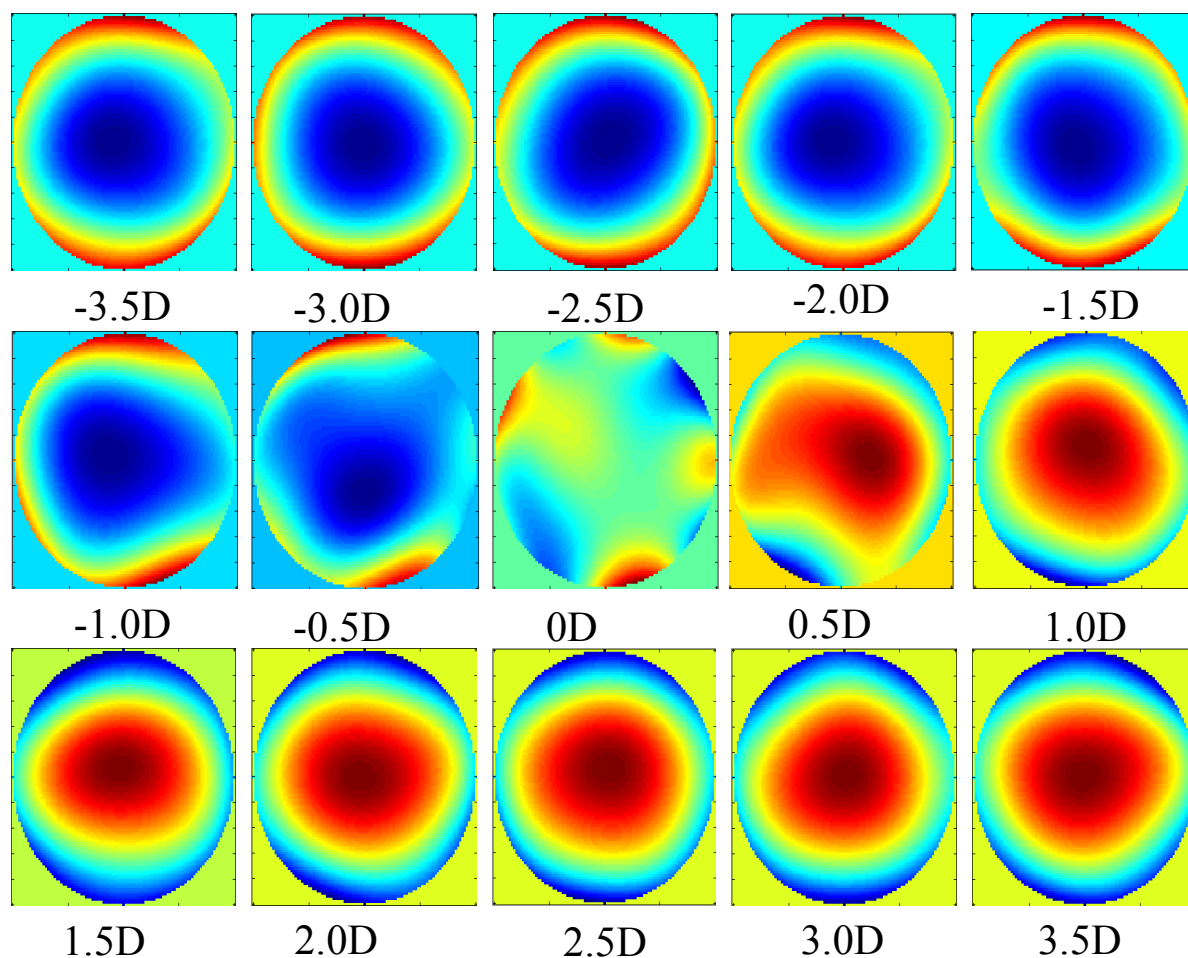


Figure 5.1. Surface plot created from the aberration of the model eye when trial lenses of power -3.5D to 3.5D in the increment of 0.5D is inserted in front of the model eye.

### 5.2.2 Ocular aberrations with a cluster of missing spots in a human eye

The right eye of the author, who has normal vision and no history of ocular disease, was used for taking the SH images. A Plano lens with small patches of transparent Sellotape<sup>TM</sup> adhered to the lens to create different missing spot disease models was worn by the subject to simulate different ocular conditions that can lead to missing spots. A representative image of the patches of the sellotape adhered to the spectacle glass is shown in Figure 5.2. The various models were created by changing the position of the tape in the glass. Table 5.1 provides a

description of the 14 models including which parts of the lens were obstructed with tape, presentation of spots deleted, and the types of condition they were intended to replicate. A schematic diagram of different visual fields of the right eye is shown in Figure 5.3. The missing models may affect one or many visual fields of the eye.



Figure 5.2. Patches of transparent Sellotape™ on the Plano glass to create disease models.

The i.Profiler Plus (Carl Zeiss Vision, Inc, USA) was used to obtain measures of wavefront aberrations at maximum natural pupil size. The SH image obtained without Sellotape is shown in Figure 5.4. The SH images for each of the fourteen models are shown in Figures 5.5-5.18. The images were taken at natural pupil conditions so the size of the SH images appeared different for different models. The number of missing spots was manually counted from each of the SH images of the missing models and the percentage of data used to generate Zernike coefficients were recorded. Since the i.Profiler Plus provides Zernike coefficients from maximum natural pupils, they were scaled down to 4.0mm pupil size to allow a comparison that was not impacted by a difference in natural pupil size between images using technique described earlier in chapter 4. To test the reliability of the missing

spot for in vivo aberration measurement, the aberration of the eye with and without missing spots were compared. HOA and different Zernike coefficients, such as coma, trefoil, and spherical aberration were compared between the SH images with and without the missing spots. Linear regression was used to find the relation between the aberrations and percentage of the data deleted from the SH image. A regression line with 95% confidence interval was plotted for the major Zernike coefficients and HOA.

Table 5.1. Fourteen disease models created by putting a tape on the glass.

<b>Missing Models #</b>	<b>Tape Position</b>	<b>% Missing</b>	<b>Disease Closeness</b>
1	Temporal	3.0	Dry eye [71-72]
2	Inferior	3.10	Dry eye [71-72]
3	Superior	3.16	Dry eye [71-72]
4	Superior	4.06	Cortical cataract [70]
5	Temporal superior	5.5	Dry eye [71-72]
6	Temporal	6.17	Cortical cataract [70]
7	Central superior	8.50	Nuclear cataract [70-71]
8	Central inferior	8.66	Cortical/Posterior subcapsular cataract [70]
9	Central temporal	9.60	Cortical cataract [70-71]
10	Superior temporal	14.90	Dry eye/ Keratoconus [70-72]
11	Temporal	16.54	Cortical/Posterior subcapsular cataract [70]
12	Central temporal	20.30	Nuclear cataract [70-71]
13	Superior temporal	23.32	Keratoconus [70]
14	Central inferior	31.50	Nuclear cataract [70-71]

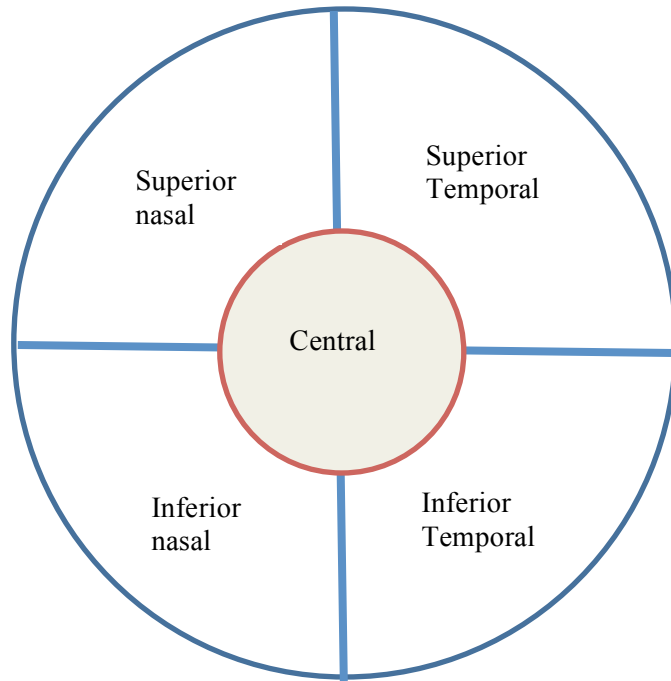


Figure 5.3. A schematic of different visual fields of the right eye.

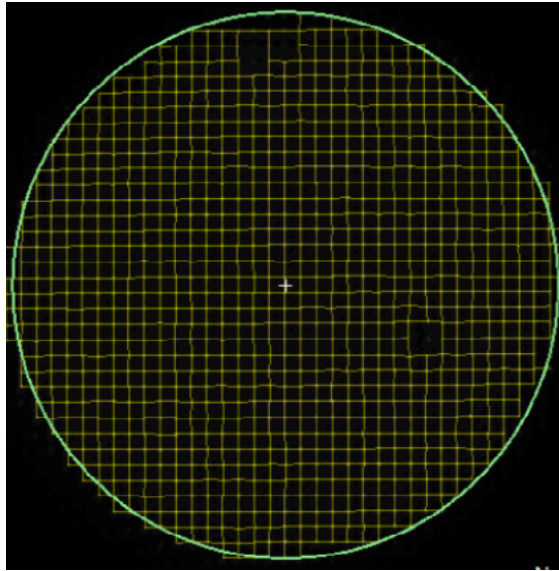


Figure 5.4. SH spot array pattern of the normal image, less than 1% of spots missing. It was taken with the spectacle glass and no tape.

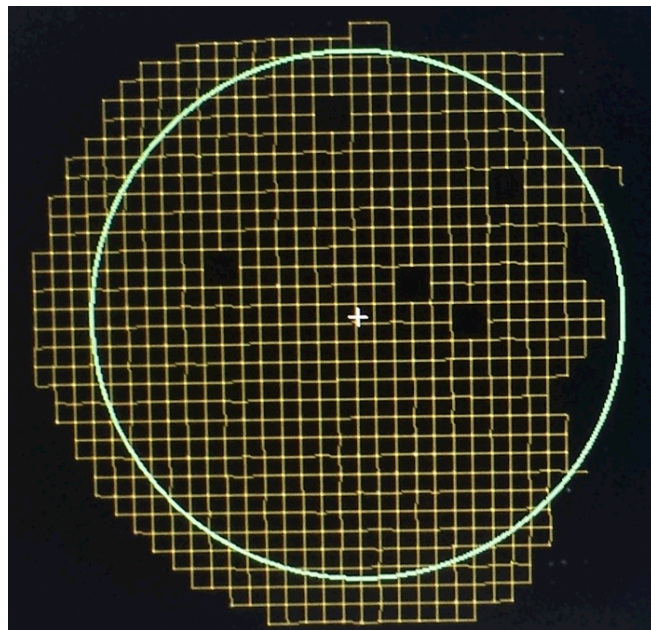


Figure 5.5. SH spot array pattern of model 1 with 3% of SH spots missing. Tape position was on the temporal side.

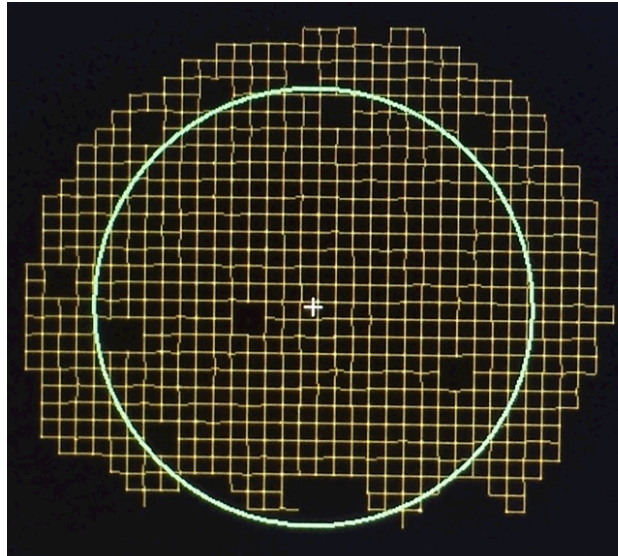


Figure 5.6. SH spot array pattern of model 2 with 3.1 % of SH spots missing. The tape was positioned on the inferior side.

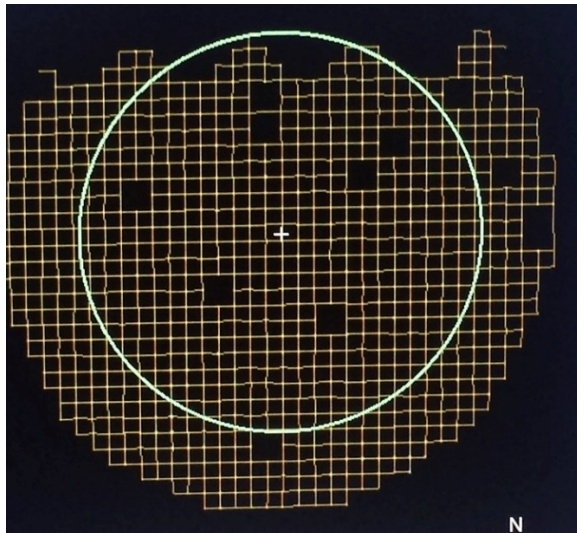


Figure 5.7. SH spot array pattern of model 3 with 3.16% of SH spots missing. The tape was positioned on the superior side.

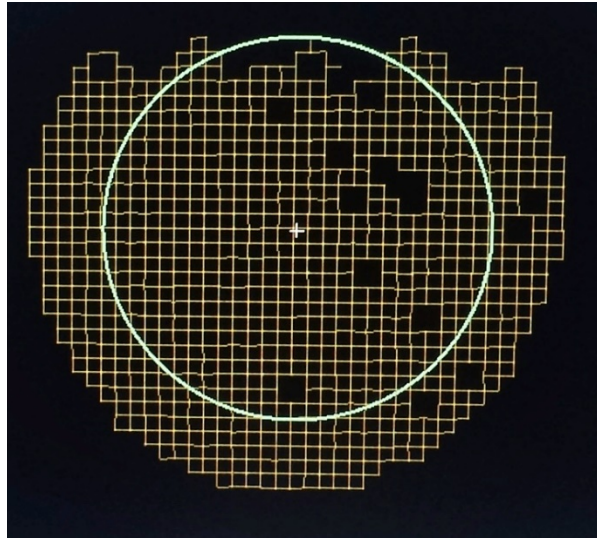


Figure 5.8. SH spot array pattern of model 4 with 4.06% of SH spots missing. The tape was positioned on the superior side.

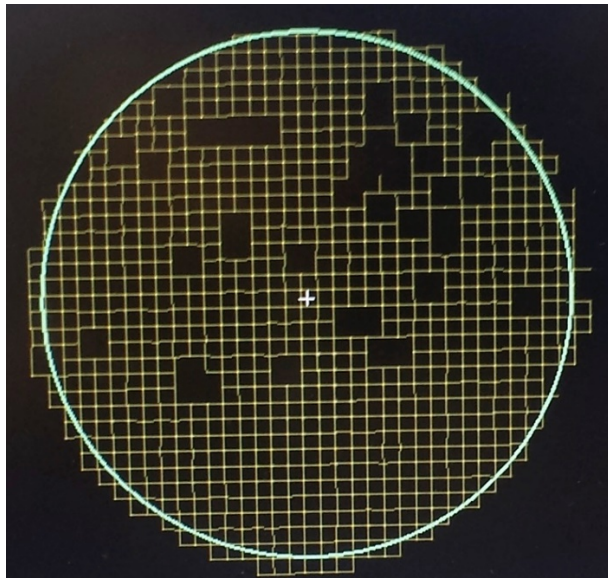


Figure 5.9. SH spot array pattern of model 5 with 5.55% of SH spots missing. The tape was positioned on the superior temporal side.



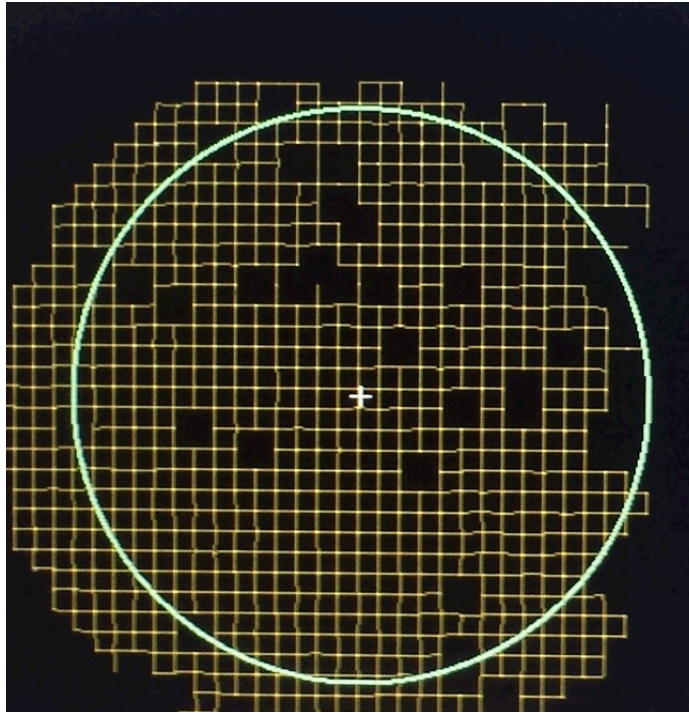


Figure 5.10. SH spot array pattern of model 6 with 6.17% of SH spots missing. The tape was positioned on the temporal side.

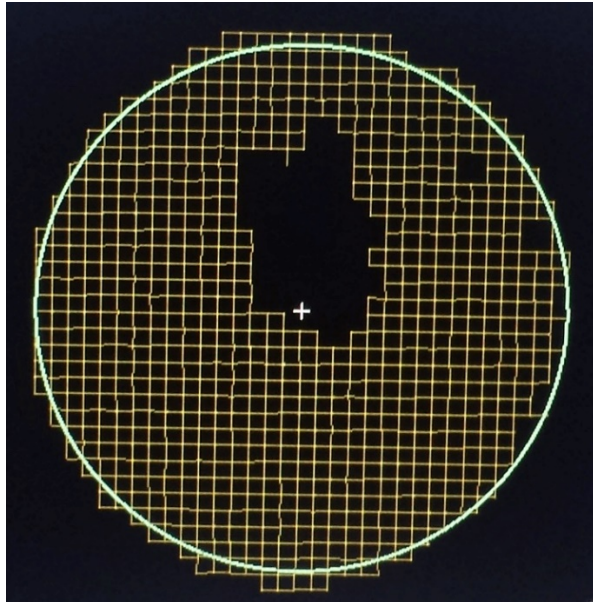


Figure 5.11. SH spot array pattern of model 7 with 8.5% of SH spots missing. The tape was positioned on the central superior side.

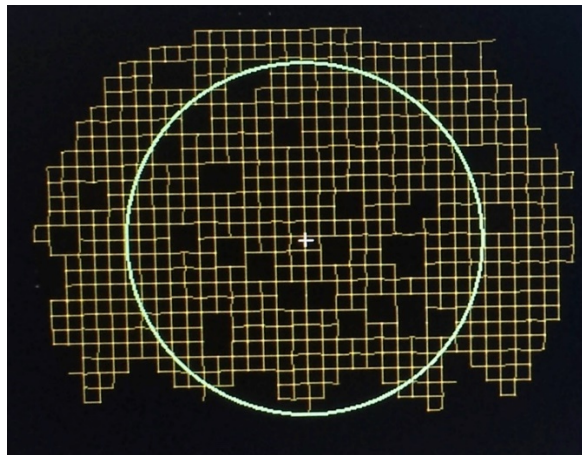


Figure 5.12. SH spot array pattern of model 8 with 8.66% of SH spots missing. The tape was positioned on the on the central inferior side.

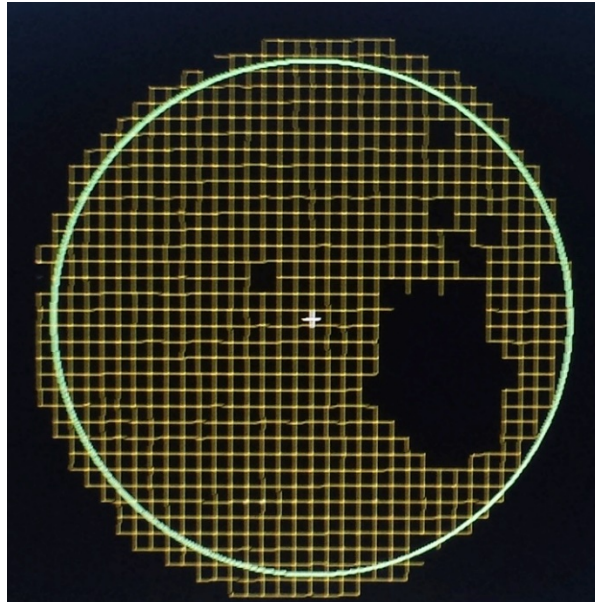


Figure 5.13. SH spot array pattern of model 9 with 9.6% of SH spots missing. The tape was positioned on the central temporal side.

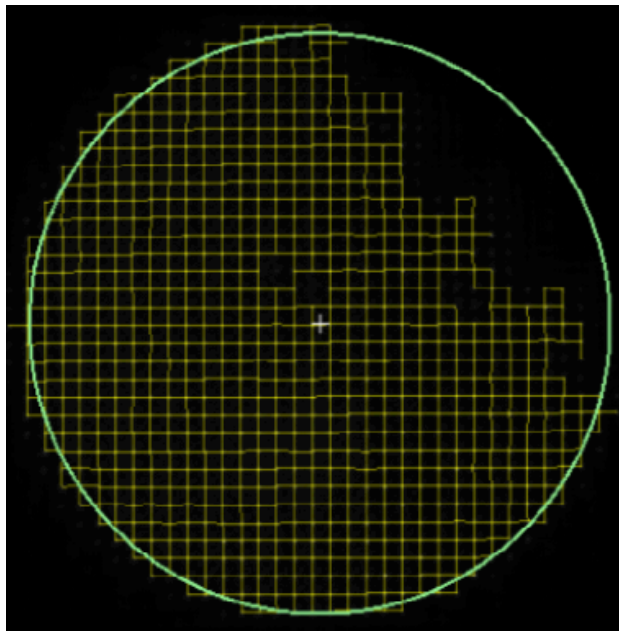


Figure 5.14. SH spot array pattern of model 10 with 14.9% of SH spots missing. The tape was positioned on the superior temporal side.

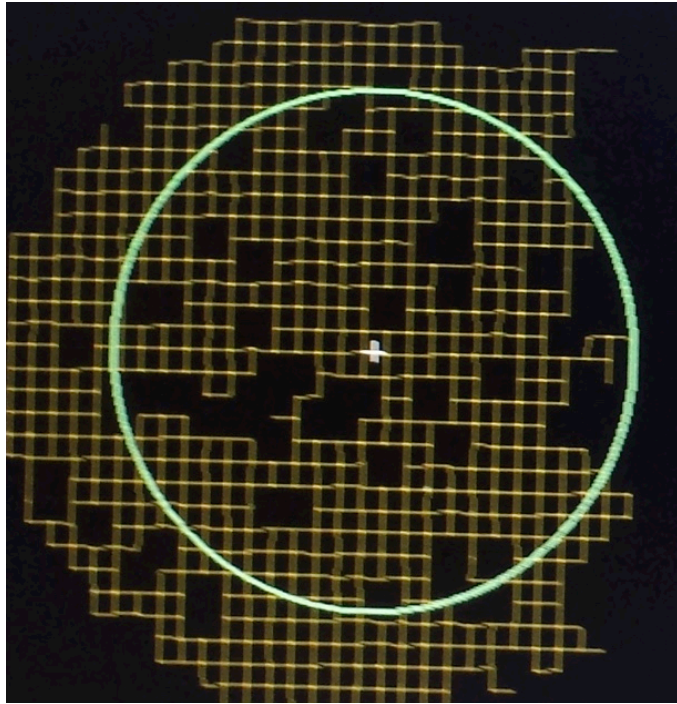


Figure 5.15. SH spot array pattern of model 11 with 16.54% of SH spots missing. The tape was positioned on the temporal side.

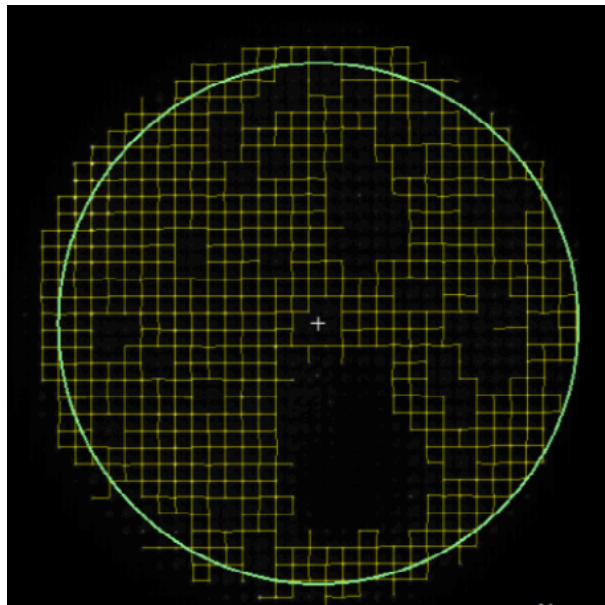


Figure 5.16. SH spot array pattern of model 12 with 20.3% of SH spots missing. The tape was positioned on the central temporal side.

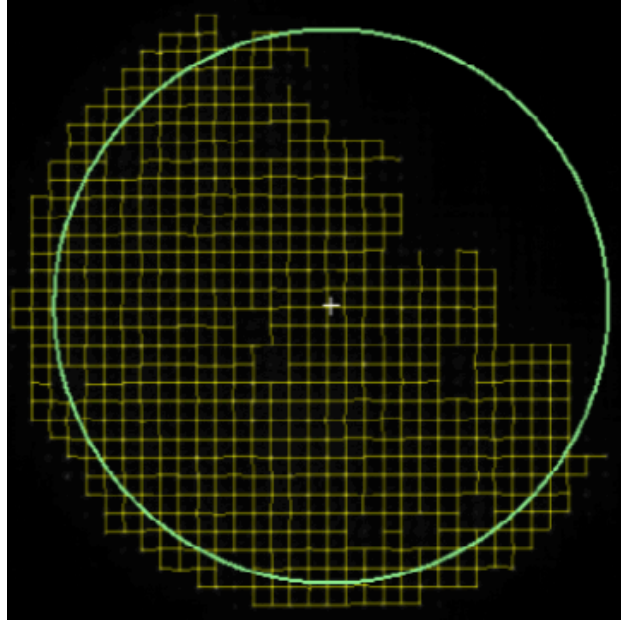


Figure 5.17. SH spot array pattern of model 13 with 23.32% of SH spots missing. The tape was positioned on the superior temporal side.

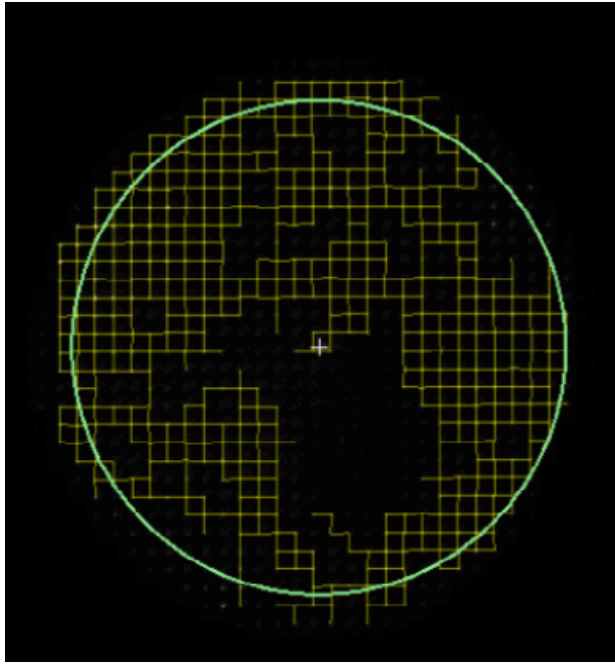


Figure 5.18. SH spot array pattern of model 14 with 31.5% of SH spots missing. The tape was positioned on the central inferior side.

## 5.3 Results

### 5.3.1 Missing spots in a model eye

Table 5.2 shows the spherical defocus (D) calculated from the Zernike coefficients with 0-80% of the SH spots deleted. The average ( $\pm$ standard deviation) of defocus in Table 5.2 indicates that there is no meaningful change in spherical power when we randomly delete SH spots from the image; however, the variation in the estimation of aberration was greater when deletions were made for higher levels of ametropia (higher standard deviation) compared to emmetropia (zero diopters of defocus) which indicates that the aberration measurement is more complicated with the ametropic condition and not as reliable as in the emmetropic condition, particularly with increasing percentage of missing spots (Table 5.2).

Table 5.2 also shows that deleting spots up to 60% gives an estimate of spherical defocus that when compared to no spot deletion is within the clinically acceptable error limit of  $\pm 0.25D$  of the sphere. Figure 5.19 shows the estimated defocus from the Zernike coefficients as a function of the actual defocus created by inserting trial lenses of different powers in front of the model eye. The plot shows that the estimated defocus is highly correlated with the actual defocus. The red solid line in Fig. 5.19 is the reference line for the estimated defocus for a specific value of the actual defocus. For more than 60% of spot deletions, the estimated defocus differed largely with the actual defocus and the standard deviation was enormously high; therefore, the 70% and 80% deletion data were not included in the figures because they were not within the clinically accepted limit of  $\pm 0.25D$ .

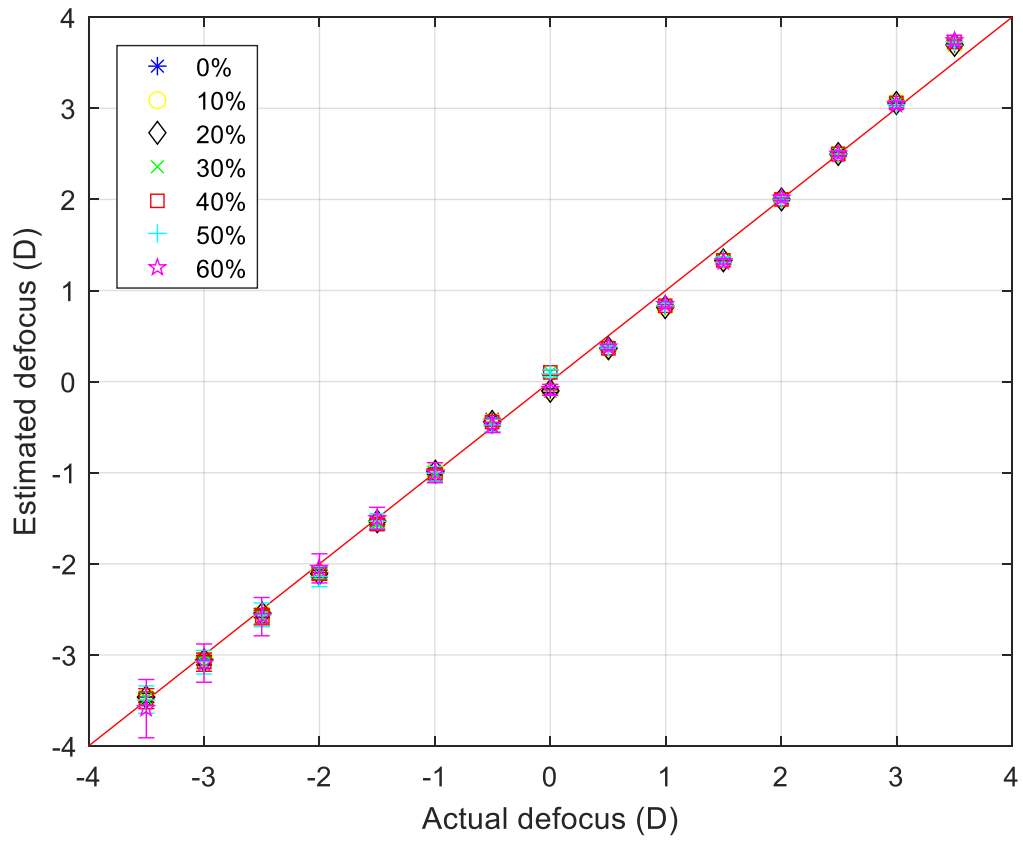


Figure 5.19. Estimated defocus vs actual defocus at different percentage of data deletions from 0 to 60%. The red solid line is the reference line for estimated defocus.



Table 5.2. Spherical defocus estimated from the SH images from 0 – 70% deletion at different defocus conditions from -3.5D to +3.5D, in 0.5D increments. The program randomly deleted the SH spots in 1000 times creating different patterns at each time. Average spherical defocus ( $\pm$  standard deviation) was calculated from the 1000 simulations.

		Percentage deletion									
Trials lens(D)	Percentage deletion										
	0%	10%	20%	30%	40%	50%	60%	70%	80%		
-3.5	-3.46	-3.46±0.02	-3.47±0.05	-3.48±0.07	-3.48±0.11	-3.49±0.15	-3.59±0.32	-19.7±443	3e15±4e16		
-3.0	-3.05	-3.05±0.03	-3.06±0.05	-3.09±0.06	-3.08±0.10	-3.08±0.13	-3.09±0.21	-3.66±9.78	2e14±7e15		
-2.5	-2.54	-2.54±0.03	-2.55±0.04	-2.59±0.07	-2.58±0.09	-2.56±0.13	-2.58±0.21	-2.8±0.75	-2e14±7e15		
-2.0	-2.10	-2.10±0.02	-2.11±0.04	-2.11±0.06	-2.11±0.7	-2.14±0.11	-2.05±0.16	-2.13±1.53	3e13±1e15		
-1.5	-1.54	-1.54±0.02	-1.54±0.03	-1.55±0.04	-1.57±0.06	-1.53±0.08	-1.5±0.12	-1.51±0.31	-3e13±15e15		
-1.0	-0.98	-0.98±0.01	-0.99±0.03	-1.0±0.04	-1.02±0.06	-1.01±0.08	-1.0±0.11	-1.01±0.22	-2e14±7e15		
-0.5	-0.42	-0.43±0.01	-0.44±0.03	-0.45±0.04	-0.45±0.04	-0.48±0.07	-0.48±0.08	-0.49±0.26	3.14±47		
0	-0.10	-0.10±0.01	-0.10±0.02	0.10±0.03	0.10±0.03	0.09±0.04	-0.09±0.06	-0.09±0.12	-0.43±1		
0.5	0.37	0.37±0.01	0.37±0.01	0.37±0.02	0.37±0.02	0.38±0.02	0.38±0.03	0.37±0.09	0.26±0.87		
1.0	0.83	0.82±0.01	0.82±0.01	0.83±0.01	0.83±0.02	0.84±0.02	0.85±0.03	0.87±0.09	0.46±5.4		
1-5	1.33	1.33±0.01	1.33±0.01	1.33±0.02	1.33±0.02	1.34±0.03	1.32±0.03	1.33±0.06	587±2e5		
2.0	2.0	2.0±0.01	2.0±0.01	2.0±0.02	2.0±0.02	2.0±0.03	2.02±0.03	2.03±0.14	1.6±2.85		
2.5	2.5	2.5±0.01	2.5±0.01	2.51±0.02	2.5±0.02	2.5±0.03	2.5±0.03	2.45±0.34	6e12±2e14		
3.0	3.07	3.07±0.02	3.06±0.01	3.06±0.02	3.06±0.02	3.05±0.03	3.04±0.04	3.01±0.10	2.6±1.8e15		
3.5	3.7	3.7±0.01	3.7±0.02	3.71±0.02	3.72±0.03	3.73±0.04	3.75±0.05	3.75±0.13	-8e11±2e13		

In addition to defocus (second-order aberrations), HOAs were also studied for the different level of spots deletions. Figures 5.20-5.23 show plots of aberrations as a function of the percentage of data deleted at different levels of defocus. While the magnitude of the HOA and Zernike coefficients were different for different values of defocus, they exhibited similar trends with the percentage of spot deleted (Figures 5.20-5.23) indicating the effect of spot deletions on ocular aberrations. Although the magnitude of the slope of the trend is not consistent across the levels of the defocus, they show a consistent pattern with respect to the percentage of spot deletions. The findings were consistent with the other studies in the literature which suggested that HOA may not be associated with or have any causative role in ametropia development [73-76].

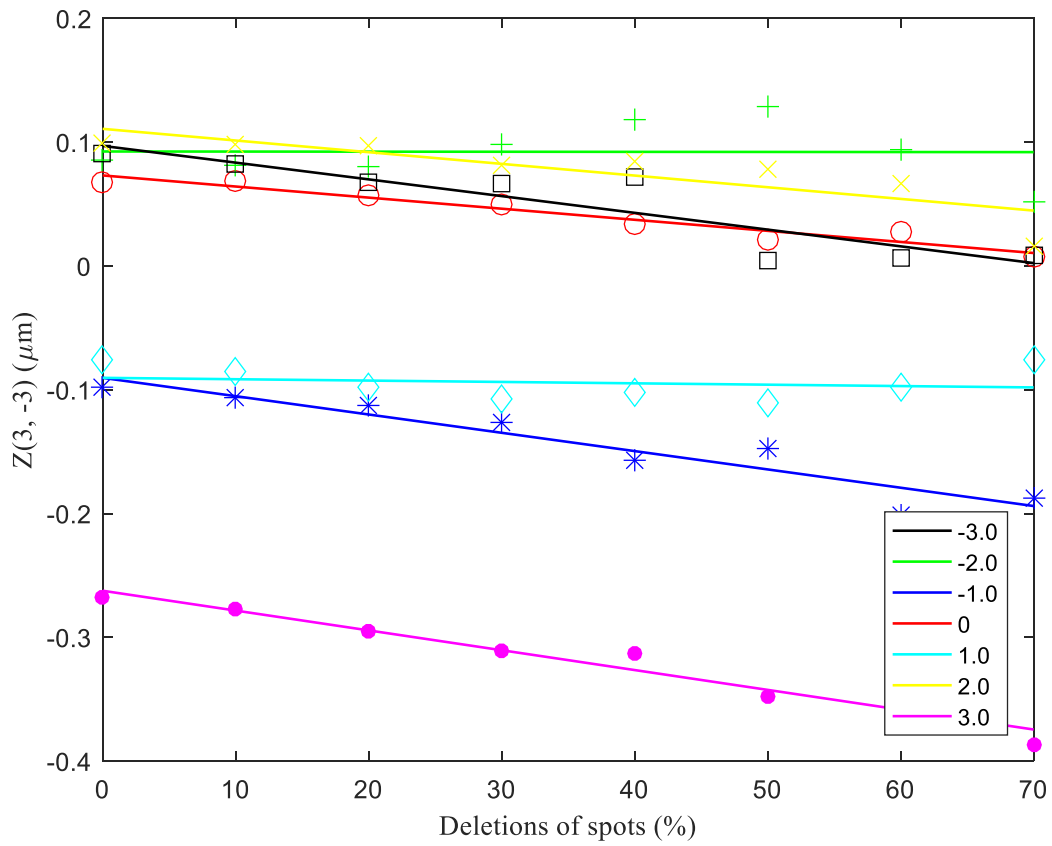


Figure 4.20. Best fit lines between Trefoil  $Z_3^{-3}$  and percentage of SH spots deleted at a different level of data deletions from -3.0 D to + 3.0D in the interval of 1.0D.

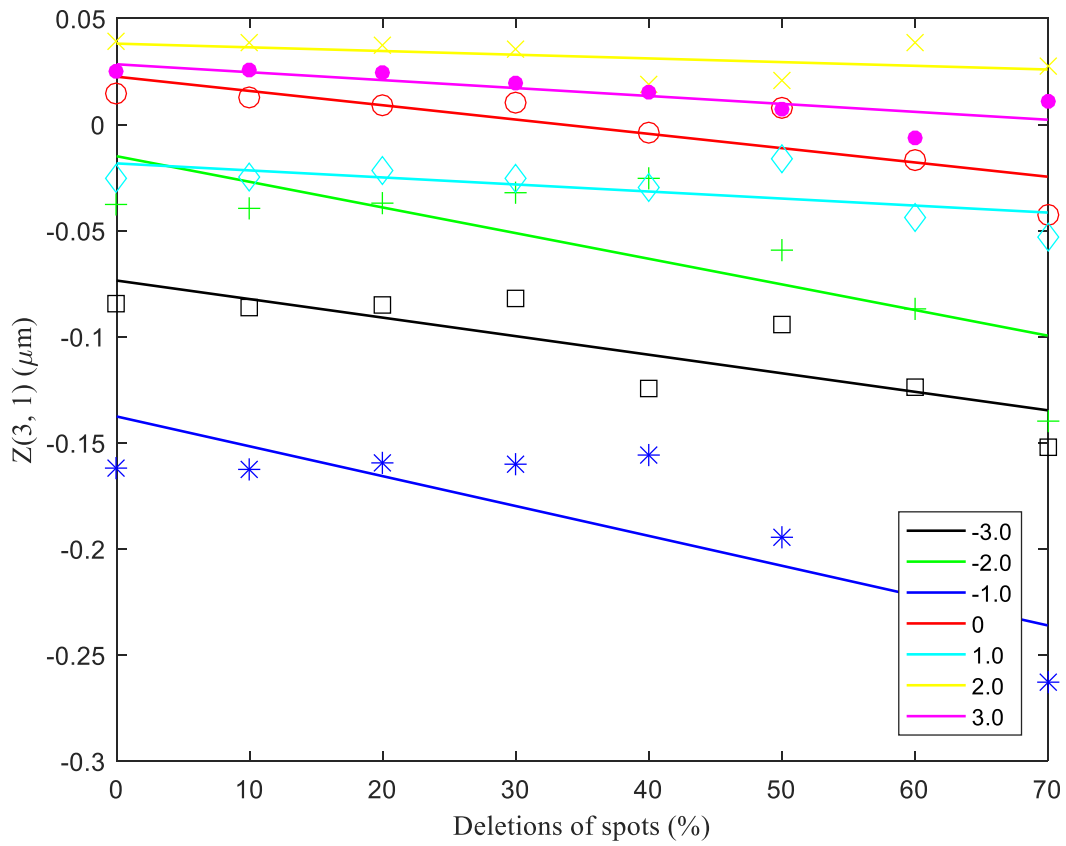


Figure 5.21. Best fit lines between Coma and percentage of SH spots deleted at a different level of data deletions from -3.0 D to +3.0D in the interval of 1.0D.

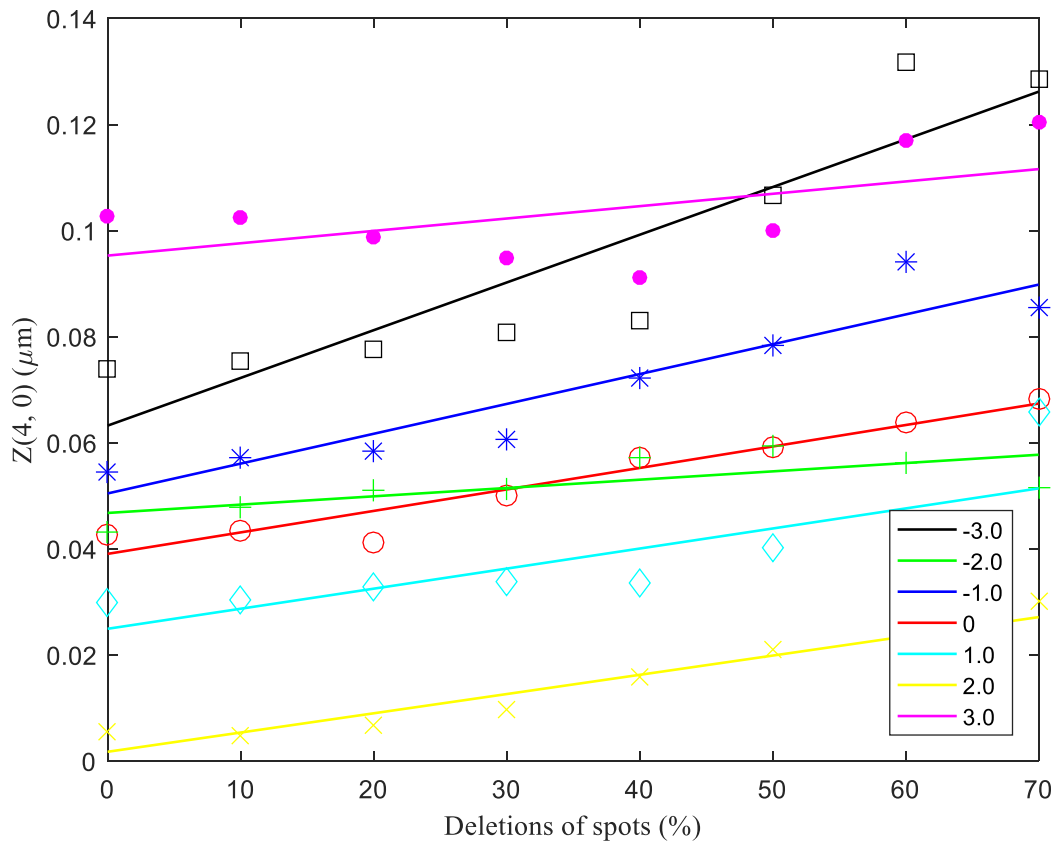


Figure 5.22. Best fit lines between Spherical aberration and percentage of SH spots deleted at a different level of data deletions from -3.0 D to + 3.0D in the interval of 1.0D.

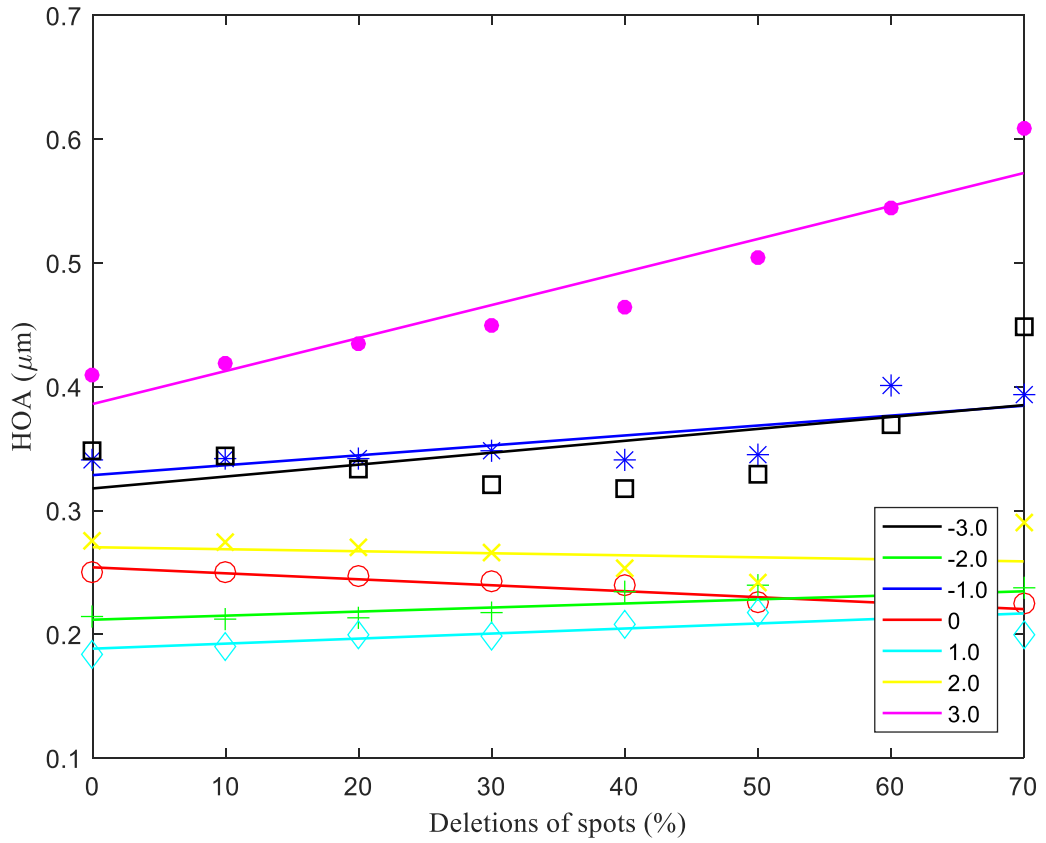


Figure 5.23. Best fit lines between higher order aberration ( $3^{\text{rd}}$  to  $5^{\text{th}}$  order) and percentage of SH spots deleted at a different level of data deletions from  $-3.0\text{ D}$  to  $+3.0\text{ D}$  in the interval of  $1.0\text{ D}$ .

### 5.3.2 Ocular aberrations with clusters of missing spots in a human eye

Tables 5.3 lists the Zernike coefficients extracted from the normal eye (without missing spots) and the various missing spots models. The Zernike coefficients were extracted up to the 5<sup>th</sup> order of aberration. Linear regression was used to describe the trend in aberration over a percentage of data deleted from the SH image. Figures 5.24-5.26 show the linear regression lines plotted between the second order aberration ( $Z_2^{-2}$ ,  $Z_2^0$  &  $Z_2^2$ ) and percentage of data deleted from the SH images. The solid line is the regression line and the dotted blue lines illustrate 95% confidence interval for the data. All the data points lie within the 95% confidence interval. The correlation (r) between  $Z_2^{-2}$  and percentage of data deleted from SH image was 0.0361. Similarly, the correlation coefficients between  $Z_2^0$ ,  $Z_2^2$  and percentage of data deletions were 0.1225 and 0.3953, respectively.



Table 5.3a. Zernike coefficients from 2<sup>nd</sup> to 5<sup>th</sup> order aberrations extracted from the SH images of normal (without missing spots) and missing spot models 1 to 7.

	Normal	Modal 1	Model 2	Model 3	Model 4	Model 5	Model 6	Model 7
% of Spot Deletion	<0.1	3.0%	3.1%	3.16%	4.06%	5.55%	6.17%	8.5%
Z(2,-2)	-0.1763	-0.1736	-0.1726	-0.1597	-0.1516	-0.1291	-0.1745	-0.1498
Z(2,0)	0.1539	0.2866	0.2458	0.01	-0.008	0.2639	0.0864	0.111
Z(2,2)	-0.0504	0.0008	0.0461	0.071	0.035	-0.054	-0.0149	-0.0209
Z(3,-3)	-0.0851	-0.0631	-0.1034	-0.067	-0.0778	-0.0673	-0.086	-0.0732
Z(3,-1)	0.0972	0.0975	0.1151	0.0126	0.048	0.0855	0.1127	0.0211
Z(3,1)	-0.0229	-0.0081	-0.0335	-0.0349	-0.0037	-0.0171	-0.0015	-0.0007
Z(3,3)	-0.0102	-0.0208	-0.0135	0.001	0.0067	-0.0162	0.0051	-0.0027
Z(4,-4)	0.0007	-0.0116	-0.012	0.0148	-0.0127	0.005	0.0037	-0.0051
Z(4,-2)	-0.0035	-0.0106	-0.0007	-0.0066	-0.0097	-0.005	-0.0005	-0.0011
Z(4,0)	0.0585	0.0482	0.0517	0.0872	0.0607	0.0557	0.0672	0.0703
Z(4,2)	-0.0091	0.0101	-0.0292	-0.0411	-0.0135	-0.0081	-0.0189	-0.0269
Z(4,4)	0.0012	0.0092	0	0.0494	0.0255	0.0056	0.021	0.0406
Z(5,-5)	-0.0044	-0.0133	-0.0139	-0.0329	-0.0139	-0.002	-0.0174	-0.007
Z(5,-3)	0.0045	0	0.0174	0.0188	0.0028	0	0.0045	-0.0094
Z(5,-1)	0.0051	-0.002	0	0.0094	0.0014	0.0051	0.004	0.0254
Z(5,1)	-0.0029	-0.0032	0.0028	0.0008	0.0028	-0.0043	-0.0058	0
Z(5,3)	-0.0019	0.0032	0.0042	-0.0055	-0.0035	0	-0.0004	-0.005
Z(5,5)	-0.0025	0.0024	0.0028	0.0165	0.0042	-0.0012	-0.0089	0.004
HOA	0.1462	0.1301	0.1715	0.1403	0.1158	0.1252	0.1609	0.1182
TA	0.2901	0.3594	0.3489	0.2243	0.1941	0.3239	0.2530	0.2217

Table 5.3b. Zernike coefficients from 2<sup>nd</sup> to 5<sup>th</sup> order aberrations extracted from the SH images of normal (without missing spots) and missing spot models 8 to 14.

	Normal	Model 8	Model 9	Model 10	Model 11	Model 12	Model 13	Model 14
% of Spot Deletion	<0.1%	8.66%	9.6%	14.9%	16.54%	20.3%	23.32%	31.5%
Z(2,-2)	-0.1763	-0.2093	-0.1397	-0.1863	-0.1664	-0.1854	-0.1128	-0.188
Z(2,0)	0.1539	0.1133	0.0499	0.136	0.1947	0.1451	0.1763	0.1788
Z(2,2)	-0.0504	-0.0731	-0.023	-0.041	-0.0206	-0.033	-0.0077	-0.0603
Z(3,-3)	-0.0851	-0.0868	-0.0822	-0.0859	-0.0838	-0.097	-0.0957	-0.0609
Z(3,-1)	0.0972	0.1142	0.0596	0.0843	0.0964	0.0364	0.098	0.0722
Z(3,1)	-0.0229	-0.0146	-0.0017	-0.0452	-0.0216	-0.0291	-0.0192	-0.0367
Z(3,3)	-0.0102	0.017	-0.0235	-0.0064	0.009	-0.0287	-0.0978	-0.0259
Z(4,-4)	0.0007	-0.0177	0.0019	0.0157	-0.0299	-0.0025	-0.0451	0
Z(4,-2)	-0.0035	-0.0055	-0.0032	0.0244	0.0044	0.0081	0.0127	-0.0031
Z(4,0)	0.0585	0.0586	0.0629	0.081	0.0387	0.0655	0.0713	0.0472
Z(4,2)	-0.0091	-0.052	-0.0169	0.0003	-0.0144	-0.0249	-0.0291	-0.0131
Z(4,4)	0.0012	0.0177	0.0019	-0.0211	0.0144	0.0063	-0.0393	0.0026
Z(5,-5)	-0.0044	0.0034	-0.01	-0.0054	-0.0125	-0.0057	-0.0492	-0.008
Z(5,-3)	0.0045	0.0068	0.0005	0.0172	0.0102	0.007	0.0056	0.0022
Z(5,-1)	0.0051	0.0216	0.0054	0.0123	0.0238	0.0094	0.0102	-0.0027
Z(5,1)	-0.0029	0.0023	0.0002	0.0107	0.0045	0.0016	-0.0062	0.0058
Z(5,3)	-0.0019	-0.0102	-0.0007	-0.0076	0.0148	-0.0016	-0.0111	0.0013
Z(5,5)	-0.0025	0.0068	0.0005	-0.019	-0.017	-0.0075	-0.0023	-0.0085
HOA	0.1462	0.1689	0.1235	0.1594	0.1450	0.1328	0.2027	0.1163
TA	0.2901	0.3008	0.1943	0.2833	0.2950	0.2723	0.2914	0.2906

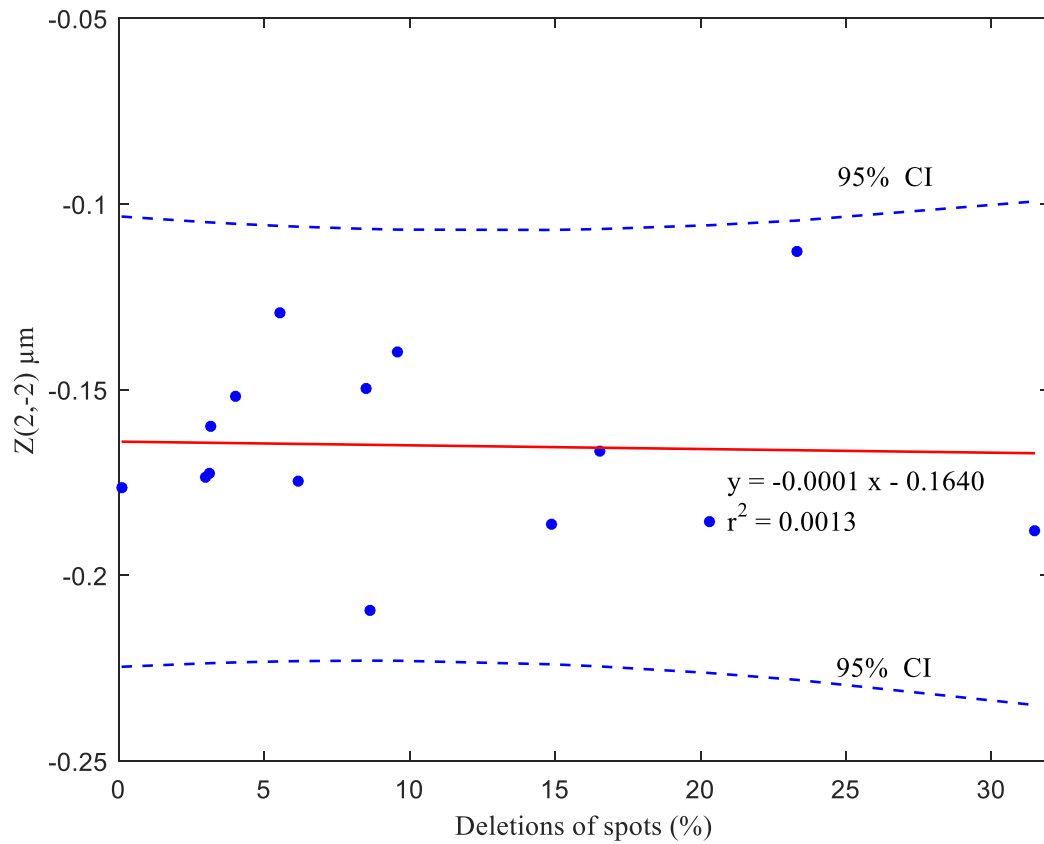


Figure 5.24. Linear regression (red line) between the 2<sup>nd</sup> order Zernike coefficients  $Z_2^{-2}$  and percentage of SH spots deleted. The dotted blue lines illustrate 95% confidence interval for the data.

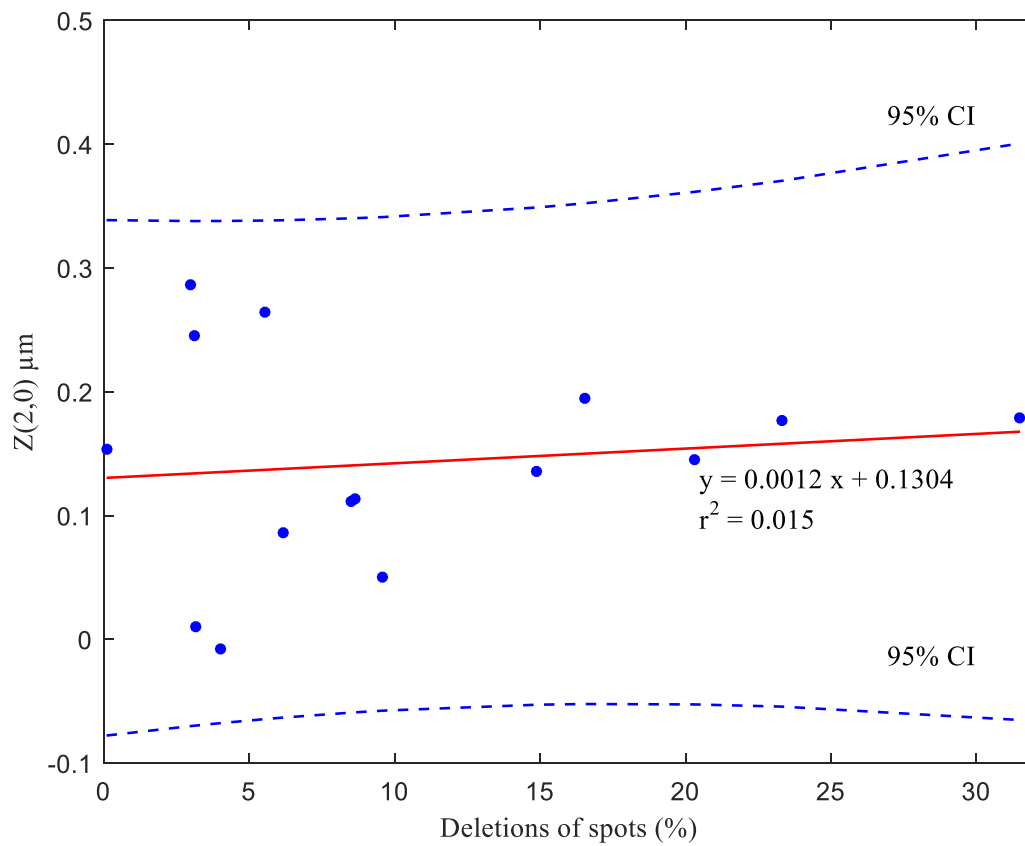


Figure 5.25. Linear regression (red line) between the 2<sup>nd</sup> order Zernike coefficients  $Z_2^0$  and percentage of SH spots deleted. The dotted blue lines illustrate 95% confidence interval for the data.

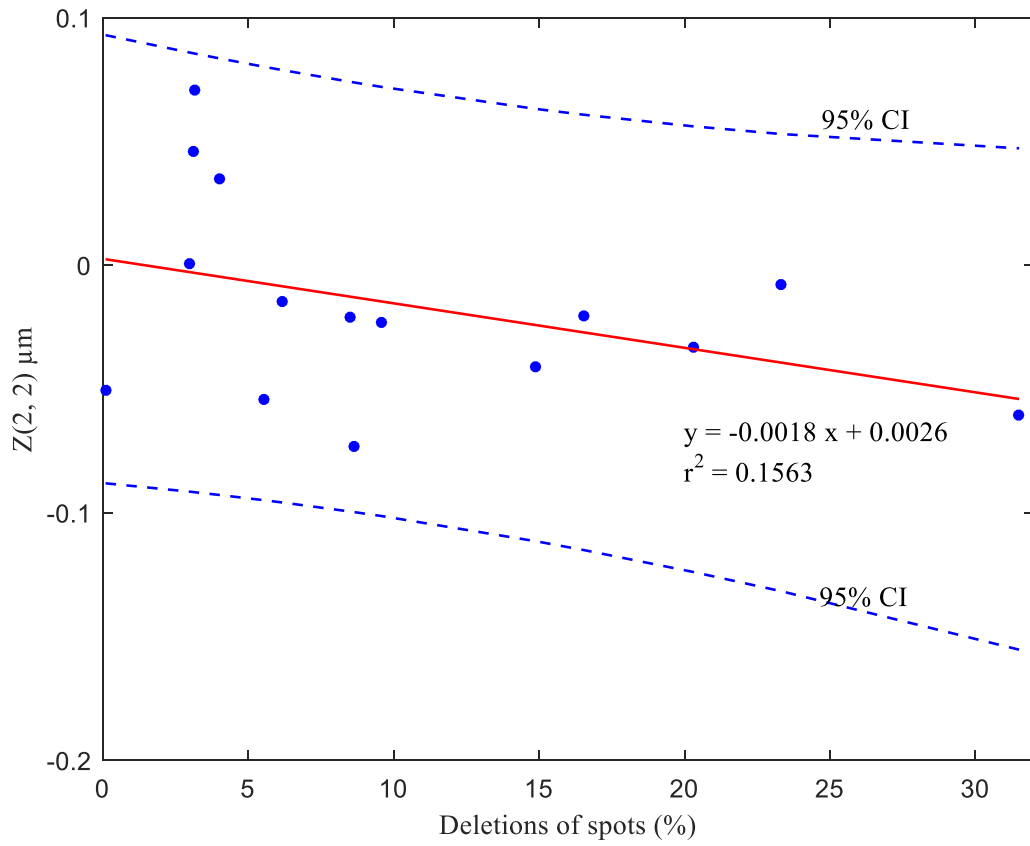


Figure 5.26. Linear regression (red line) between the 2<sup>nd</sup> order Zernike coefficients  $Z_2^2$  and percentage of SH spots deleted. The dotted blue lines illustrate 95% confidence interval for the data.

The linear regression line between the 3<sup>rd</sup> order Zernike coefficients,  $(Z_3^{-3}, Z_3^3)$  and the percentage of data deleted is shown in Figure 5.27 and 5.28, respectively. No significant relationship ( $r = 0.0387$ ) was detected between the vertical trefoil ( $Z_3^{-3}$ ) and the percentage of data deleted; however, a moderate correlation ( $r = 0.4942$ ) was observed between horizontal trefoil ( $Z_3^3$ ) and percentage of spot deletions. All the data lie within the 95% confidence band.

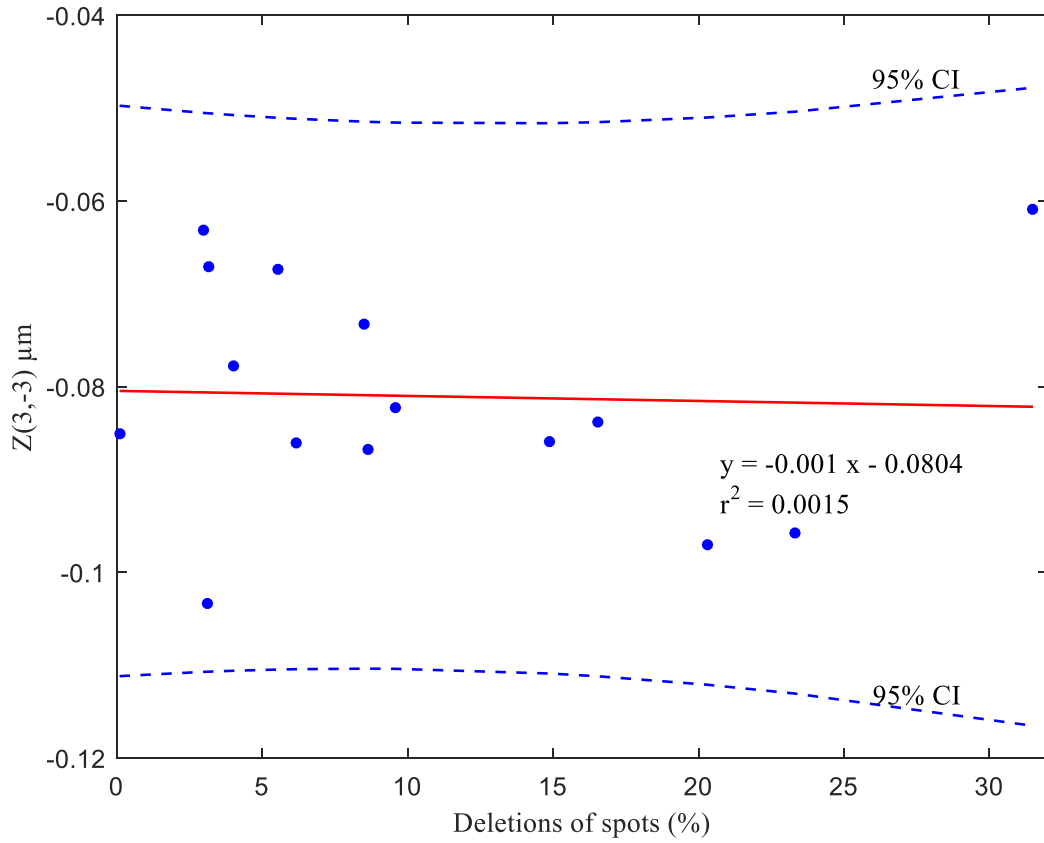


Figure 5.27. Linear regression (red line) between the 3<sup>rd</sup> order Zernike coefficients  $Z_3^{-3}$  (vertical trefoil) and percentage of SH spots deleted. The dotted blue lines illustrate 95% confidence interval for the data.

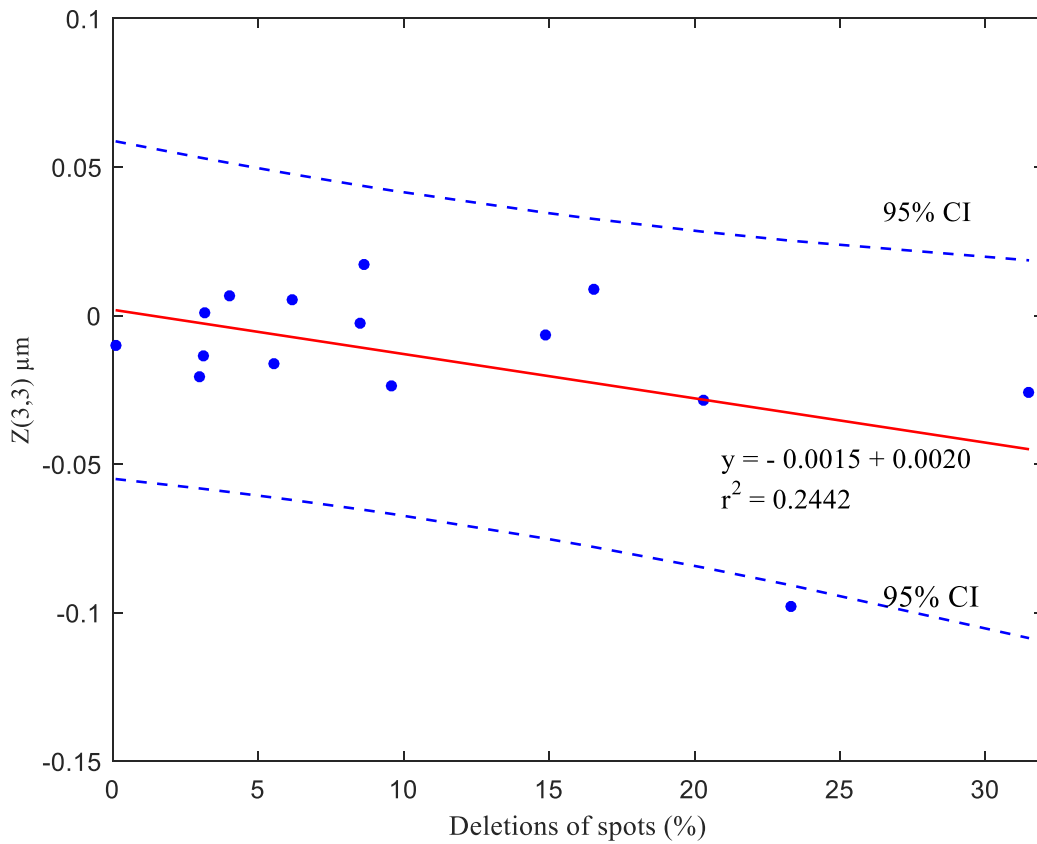


Figure 5.28. Linear regression (red line) between the 3<sup>rd</sup> order Zernike coefficients  $Z_3^3$  (horizontal trefoil) and percentage of SH spots deleted. The dotted blue lines illustrate 95% confidence interval for the data.

Figures 5.29 and 5.30 shows the linear regression lines plotted between the 3<sup>rd</sup> order Zernike coefficients,  $(Z_3^{-1}, Z_3^1)$  and the percentage of data deleted from the SH images. The regression analysis showed that there was a weak relationship ( $r=0.0480$ ) between the vertical



coma ( $Z_3^{-1}$ ) and the percentage of data deleted; however, a moderate relationship ( $r=0.3696$ ) was observed between the horizontal coma ( $Z_3^1$ ) and the percentage of data deleted from the SH images. The horizontal coma increased when more data were deleted from the SH images. All the data lie within the 95% confidence band.

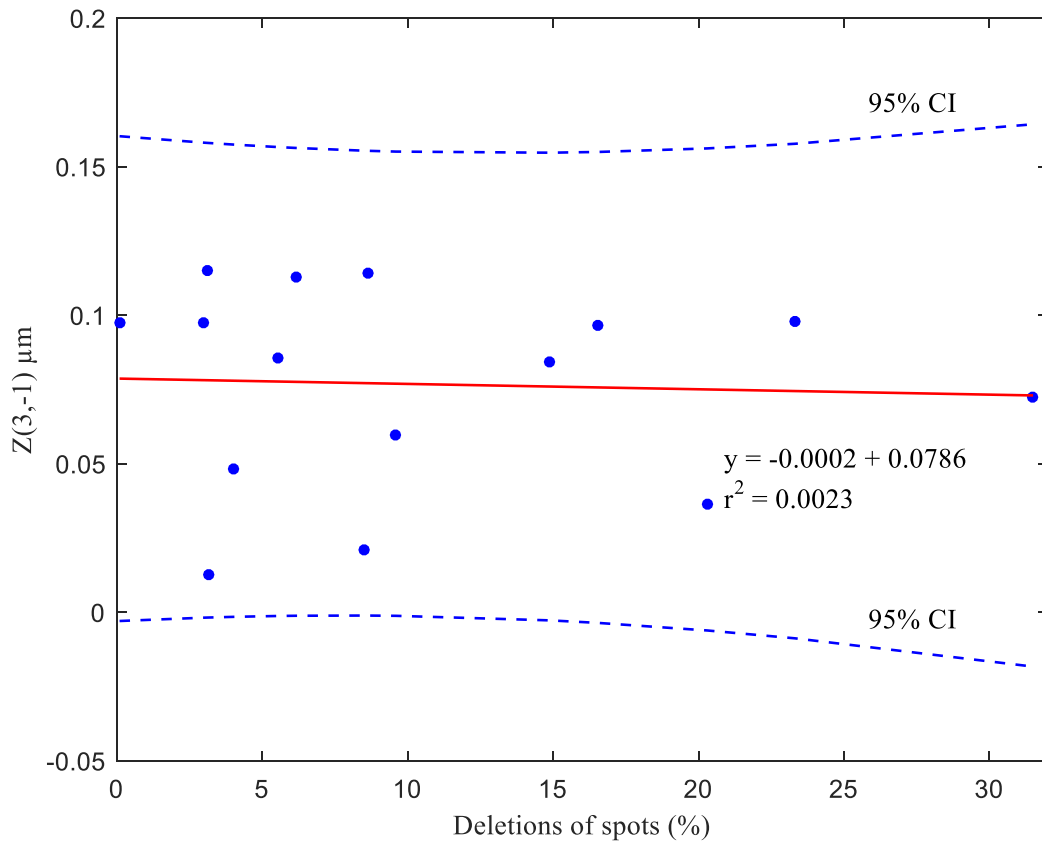


Figure 5.29. Linear regression (red line) between the 3<sup>rd</sup> order Zernike coefficients  $Z_3^{-1}$  (vertical coma) and percentage of SH spots deleted. The dotted blue lines illustrate 95% confidence interval for the data.

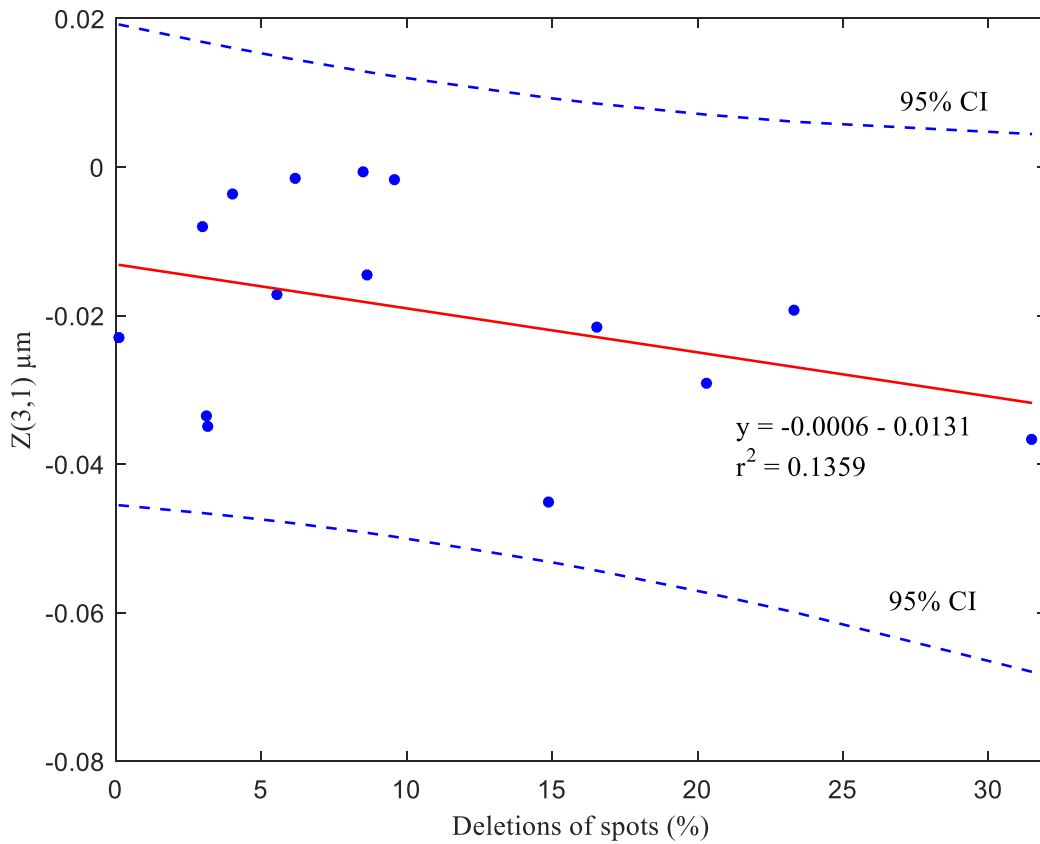


Figure 5.30. Linear regression (red line) between the 3<sup>rd</sup> order Zernike coefficients  $Z_3^1$  (horizontal coma) and percentage of SH spots deleted. The dotted blue lines illustrate 95% confidence interval for the data.

Figure 5.31 shows the linear regression line plotted between the spherical aberration ( $Z_4^0$ ) and the percentage of data deleted from the SH images. The regression analysis showed that

there was a weak linear relationship ( $r=0.1100$ ) between the spherical aberration and the percentage of data deleted from SH images.

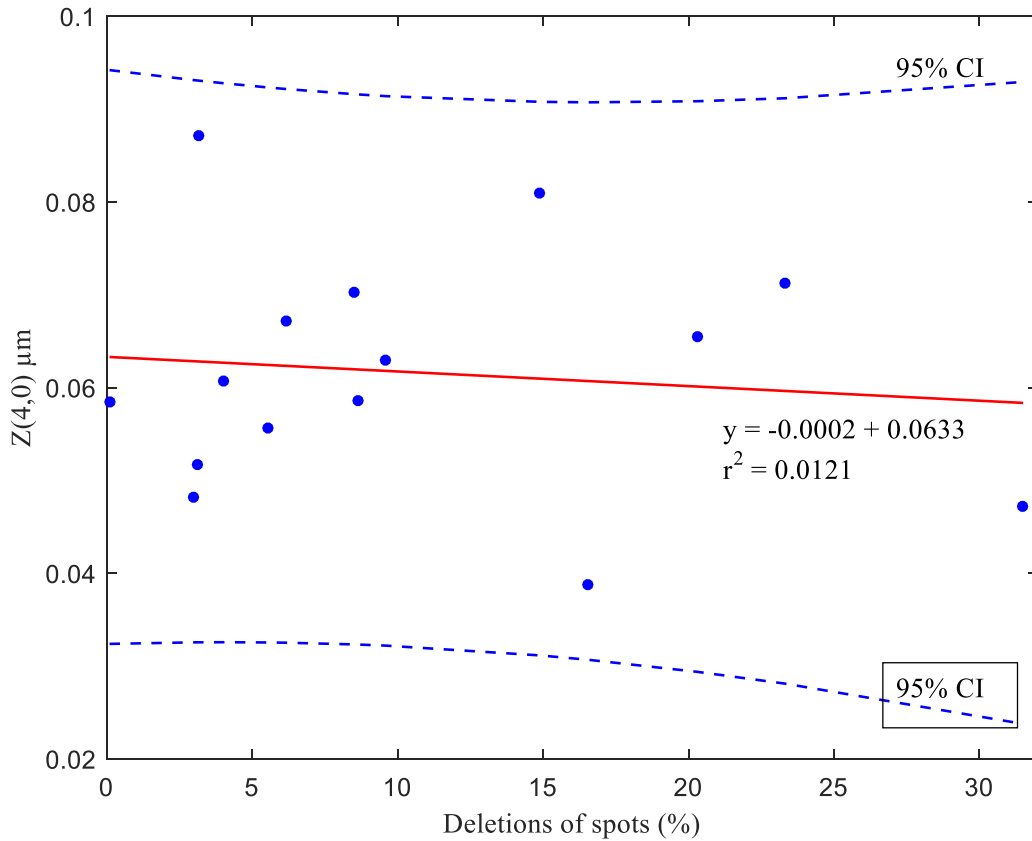


Figure 5.31. Linear regression (red line) between the 4<sup>th</sup> order Zernike coefficients  $Z_4^0$  (spherical aberration) and percentage of SH spots deleted. The dotted blue lines illustrate 95% confidence interval for the data.

Similarly, I examined the linear regression between the HOA (from 3<sup>rd</sup> to 5<sup>th</sup> order) and the percentage of spots deleted from the SH images (Figure 5.32). No significant relationship ( $r=0.0854$ ) occurred between the HOA and the percentage of data deleted from the SH

images. Although the correlation was not strong, the magnitude of HOA increased when more data were deleted from the SH images. All the data lie within the 95% confidence band.

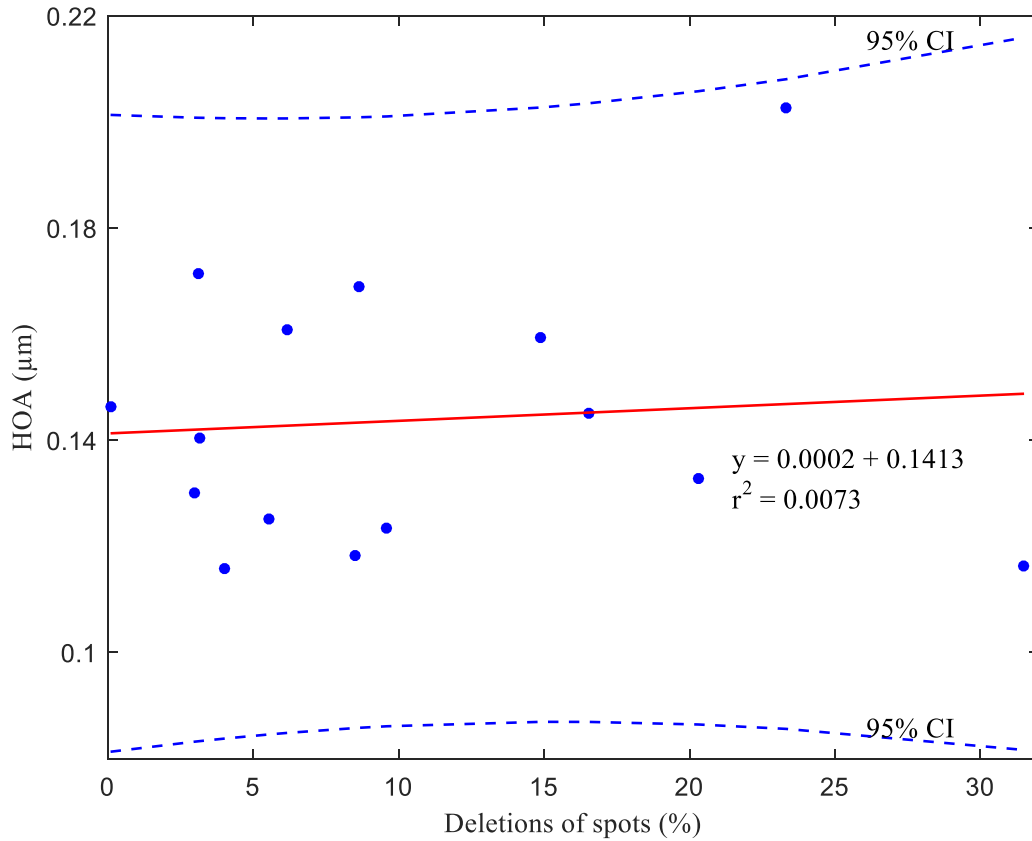


Figure 5.32. Linear regression (red line) between the higher order aberration (HOA) from 3<sup>rd</sup> to 5<sup>th</sup> order and percentage of SH spots deleted. The dotted blue lines illustrate 95% confidence interval for the data.

Linear regression between the total aberration (TA) from 2<sup>nd</sup> to 5<sup>th</sup> order and percentage of SH spots deleted was also studied. Like HOA, the TA was also increased when more data

were deleted from the SH images; however, the correlation between the TA and the percentage of data deleted was weak ( $r=0.0332$ ).

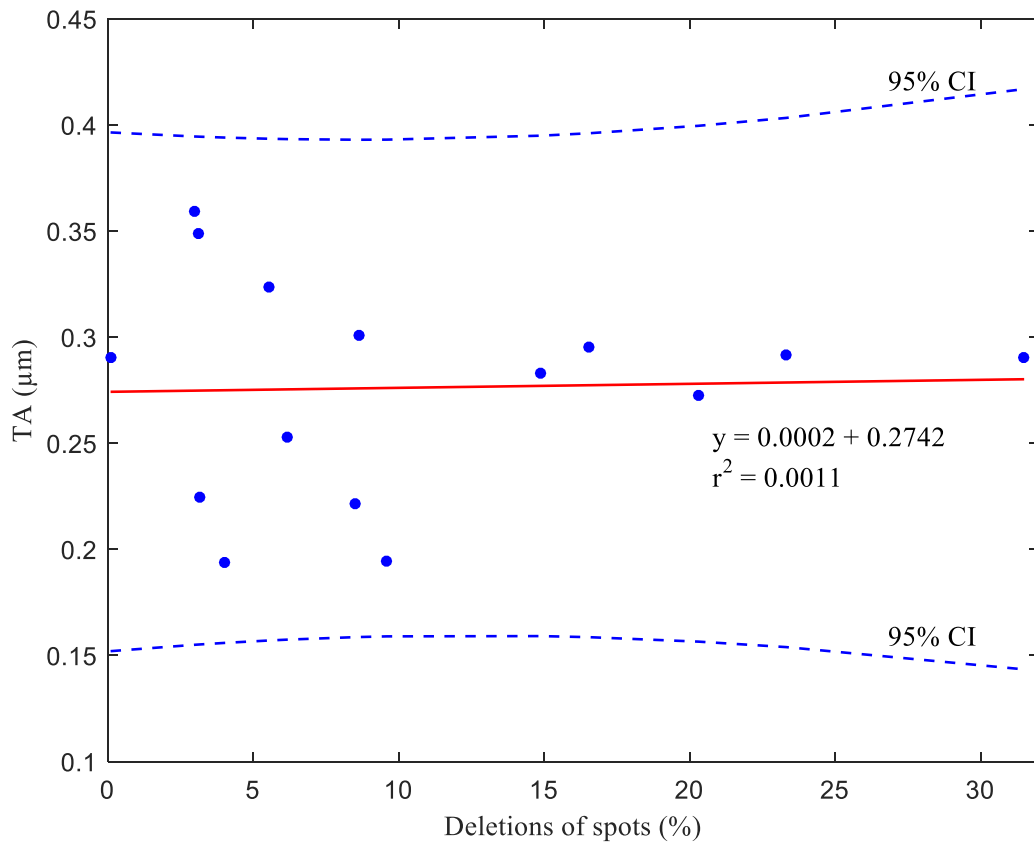


Figure 5.33. Linear regression (red line) between the total aberration (TA) from 2<sup>nd</sup> to 5<sup>th</sup> order and percentage of SH spots deleted. The dotted blue lines illustrate 95% confidence interval for the data.

## 5.4 Conclusion

In this Chapter, two strategies were used to create missing spots on the SH images. First, spots were randomly deleted from the SH images in the post-processing phase using computer programming. Second, small pieces of tape were used in different parts of the glass

and images were taken wearing those glasses from the human participants that created SH images with a cluster of missing spots. The former is basically an experiment that looks at the how many spots can be missing, regardless of their clustering whereas the latter is a look at the impact of clustering. As might be expected, the impact of clustering is greater on the aberration measurement compared to the random spatial location of the missing spots.

In the first part of this chapter, I demonstrated the impact on ocular aberration measurement from SH images with a less than maximal/optimal number of SH spots, by artificially simulating random patterns by deleting 0% to 80% of spots. I have shown that the aberration measurements gave clinically acceptable measures ( $\pm 0.25D$ ) up to 60% deletion. Moreover, the HOA generated with or without missing spots were comparable.

In the second part of the experiment, ocular aberrations were measured in vivo from SH images of a normal eye without artificial obstructions and with several models of missing spots. It was found that the Zernike coefficients were not appreciably different between the normal and missing spots models. Linear regression plots described the trend in the aberration measurements over the percentage of spots deleted from the SH images. The plots showed that the relationship between the Zernike coefficients and percentage of spots deleted were not strong for all the models compared.

The measurement of ocular aberration from abnormal eyes that suffer from anomalies of the tear film, corneal disease, corneal shape, corneal refractive surgery, and lenticular cataract can be limited by a reduced number of SH spots in the images. In particular, for conditions, such as cataract and keratoconus [68], the use of wavefront aberrometry is an issue because

of missing or poor appearance of the SH spots [32]. It is crucial to determine the reliability of ocular aberration measurements in the real human eye, particularly in certain pathologies. In this chapter, I have examined the reliability of aberrations when a cluster of spots are missing using Sellotape<sup>TM</sup> to generate simple models to simulate the kinds of clusters of missing spots that might be present in different diseases. Although this methodological approach controls other factors that might impact the results, such as comorbidity of another ocular disease, for example, the results give an indication of the likely impact of missing spots with the chosen spatial clusters. In reality, the same conditions can present with a variety of different spatial clustering of missing spots and may coexist with other factors that impact the number of spots present in the image and/or the quality of those spots. In addition, each piece of tape has a consistent optical density, which, in itself, does not provide a fully realistic model for the disease conditions that might result in missing spots in the image. Nevertheless, the model does give us an insight on the impact of spatially clustered missing spots

Also, in contrast to the custom-made aberrometer, the clinical iProfiler plus was unable to obtain image data when a large number of spots (>50%) were missing from the image. Therefore, we were unable to report the impact of >50% missing spots in the SH image on in vivo measurements of aberrations. However, the results described in the first part of the study indicate that the outcome would likely be an increase in the error and greater variability in the measurements. The literature reports that the number of SH spots are variable due to specific conditions such as opacities or diseases [67], such as cataract. In reality, the artificial models created only represent one version of the type of presentation that we might see in a

particular condition. For example, a triangular section might indicate the kind of cluster of locations affected by a cortical cataract. Therefore, this study may provide valuable foundational information for wavefront aberration measurements from similarly affected cataractous eyes. A more rigorous analysis is needed to understand the effect of missing spots on the reliability of the ocular aberration measurements from the diseased eye which results in missing spots.



## Chapter 6

### Conclusion and future direction

#### 6.1 Summary of the dissertation

In this dissertation, I have discussed the assessment of ocular wavefront aberrations in specific two cases: (1) variation of pupil size (pupil scaling) and (2) suboptimal measurement (reduced number of SH lenslets). The dissertation began with an introduction to ocular aberrations and the various factors that affect reliable estimation of wavefront aberration. A raw SH image taken with a sensor usually undergoes a pre-processing stage. The pre-processing algorithms improve the image quality so that the light distribution centroid estimation is precise. From the centroid data, the slope of the local wavefront is calculated from which the entire wavefront is reconstructed. The wavefront reconstruction is influenced by many factors such as centroid measurement technique, pupil size, number of SH spots. In this thesis, I examined some challenges and issues in the assessment of ocular aberration so that it can be applied in clinical settings.

First, I developed a SH wavefront aberrometer that is similar to a commercially available aberrometer except that it consists of a window, which allows a visual stimulus that can be freely viewed binocularly during data collection. This better replicates natural viewing conditions (unlike in most commercial instruments), hence giving a more realistic estimation of the state of ocular aberrations. This SH system records video at a frame rate of 24 frames/second for 5 to 10 seconds, providing at least 120 frames for integration and produces a reliable estimate of the average aberrations from each eye. This procedure minimizes the

random Markovian fluctuations of the aberrations. The aberrometer that was developed operated within acceptable measurement and safety limits.

Centroid estimation is a crucial step for wavefront aberration measurement. The accuracy of optical aberration measurement is intimately related to the centroid estimation accuracy. Furthermore, the centroid estimation is sensitive to the influence of stray light reflections, scattered light, and noise. In Chapter 3 of this thesis, I compared the performance of four different commonly used centroid estimation methods, with and without the use of some pre-processing steps (thresholding, Gaussian smoothing, and adaptive windowing in the SH image). An eye model was used for data collection. Ametropia was simulated by inserting trial lenses of values up to  $\pm 1.0$  Diopters. The results show that there was not a significant difference between the four different centroid estimation methods and any currently available centroiding algorithm is sufficient for applications in the ophthalmic clinic for estimating aberrations within the typical clinically acceptable limits of a quarter diopter boundaries. This of course requires that the designated pre-processing steps are used to reduce the impact of external factors.

In Chapter 4, I evaluated the assessments of ocular aberrations for scaled pupil size. Recently, a number of mathematical techniques for predicting wavefront aberration measurements for different pupil sizes have been published; however, the published data is not validated with clinical data. In this thesis, I have validated the mathematical Zernike pupil size scaling from small pupils to large pupils, and vice versa, by comparing the estimates of the Zernike coefficients with corresponding clinical measurements obtained at different pupil sizes. In the scaled down condition Zernike coefficients were estimated for a

3mm pupil size from the measured data of the maximum natural pupil size. Similarly, for the scaled-up condition, Zernike coefficients for the maximum pupil size were estimated from the measured data of the 3mm pupil. The differences between the estimated and measured values were not significantly different over the range of pupil sizes examined, irrespective of whether the estimates were made by scaling up from a small pupil or scaling down from a large pupil. However, the difference between the measured and estimated coefficients was more variable and less systematic when scaling up to a larger pupil size when compared to scaling down to a smaller pupil size. These findings have implications for pupil scaling on an individual basis, such as in cases of refractive surgery or when using pupil scaling to examine a clinical cohort.

In Chapter 5, I assessed the wavefront aberration for a smaller number of SH lenslet numbers – i.e. reduced number of lenslets in the sensor. More specifically, the impact of the missing spots of the SH sensor output on the estimation of ocular aberrations was investigated. In the first part of Chapter 5, I examined the number of SH spots that can be deleted from the SH image without significantly impairing the prediction of the defocus of the computed Zernike polynomials wavefront representation. The spots were computationally deleted from the SH images to make the missing spots model. To test the resulting aberration from the missing spots, the spot number was reduced from zero to 80% of the total number available in the sensor. The deletion of the SH spots was randomized such that there was no control exerted over the spatial location of the deleted spots. The experiment was performed on data acquired through the previously described aberrometer utilizing a model eye with different powers of the trial lenses in front of the model eye to simulate refractive

errors (defocus between  $\sim\pm 3.50\text{D}$ ). Estimates of defocus were made from each of 1000 runs at each trial lens power. I reported the standard deviation of error and mean error for 1000 trials. The results indicate that as high as 60% of the SH spots can be deleted without affecting the estimation of spherical defocus, within typical clinically acceptable limits of  $\pm 0.25\text{D}$ . A study conducted by Bennett et. al. [77] show that there is a certain level of variability in refractive assessment by wavefront aberrometry, autorefraction, and subjective refraction. In the comparison between autorefraction and subjective refraction, 94.2% of measurements were within  $\pm 0.50\text{D}$ , approximately 80% were within  $\pm 0.25\text{D}$ , and 7 measurements differed by more than  $\pm 0.50\text{D}$ . In the comparison between wavefront aberrometry and subjective refraction, 90% of measurements were within  $\pm 0.50\text{D}$ , 73% were within  $\pm 0.25\text{D}$ , and 12 measurements differed by more than  $\pm 0.50\text{D}$ . This indicates that the difference in spherical defocus within a standard deviation of  $\pm 0.250\text{D}$  obtained in our study is considered an acceptable limit. The second part of Chapter 5, reports data from an in vivo measure of aberration. Inserting a plano lens with different spatially located simulated opacities in the optical pathway was used to create clustered missing spots. Fourteen different missing models were created, and regression analysis between the aberrations and percentage of spots delated was conducted. The aberrations of the missing models were within the acceptable level (95 % confidence interval) even when a large number of spots were missed from the SH images; however, no specific trend was observed with increasing number of missing spots.

## 6.2 Future directions

An assessment of ocular aberrations at scaled pupil size and reduced SH number was studied in this thesis. I anticipate that the following research questions that have evolved from this thesis.

In chapter 3, I compared the performance of several standard centroid methods in a model eye. This can be further evaluated by including other centroid measurement methods and considering them in the conjunction with other factors that may influence the performance of the centroid method but were controlled in my thesis work. Similarly, comparative performance of these centroid measurement methods in vivo would allow correlation between theoretical models and clinical measurements. It will be interesting to see if a centroid measurement method provides a consistent result with the model eye, normal human eye and diseased eyes or one particular method is better with the model eye while another technique is more suitable for the human eye.

It was noticed that the pupil size scaling formula worked well for the scaled down conditions but for scaled-up conditions, it was not consistent when the difference between the measured and estimated pupil size was large. Instead of the commercial wavefront sensor, we can use a custom made wavefront sensor and examine the pupil size scaling algorithm (described in Chapter 4) for every 0.25mm pupil size increment and examine the correlation between the Zernike coefficients of scaled pupil size and experimentally measured values. This will provide us with a threshold pupil size after which the pupil size scaling techniques do not work as accurately. The custom-made aberrometer provides the flexibility to select pupil size

and hence, has many potentials advantages for such a study. In addition to this, the pupil size scaling techniques can be extended to examine different diseases at different stages.

In chapter 5, the same participant was used for creating all the missing models and aberrations. In the future, different participants can be recruited to examine the intra-subject repeatability and variability. In addition, we can expand this study by recruiting subjects with a manifest disease that affects the optical quality of the eye, such as keratoconus. Also, it would be interesting to look systematically at particular patterns with increasing density and spatial extent as in cataract development. Perhaps, for example, modeling the opacity on a validated grading scale, such as the Lens Opacities Classification System (LOCS) [78].

Further experimental studies are needed to verify whether the missing spot models work with normal and diseased human eyes. If this technique validated there is a huge potential to further develop the SH wavefront sensor with fewer lenslets. This would result in low-cost development of the wavefront analyzer, which can benefit patients in rural/underserved areas and in developing countries to enable collection of aberrometry measurements and potentially impact healthcare access disparities.

## Appendix

### Copyright Permissions

#### 1. Copyright: Permission to use images

From: Helga Kolb <[Helga.kolb@hsc.utah.edu](mailto:Helga.kolb@hsc.utah.edu)>  
Sent: Monday, October 1, 2018 8:03:26 AM  
To: Abbas Ommani  
Cc: Hospital Webvision; Abbas Ommani  
Subject: Re: permission for images

You are very welcome to use the images you request from webvision.

Best wishes,  
Helga Kolb

Helga Kolb  
Professor Emeritus  
Moran Eye Center  
435-658-1732  
[Helga.Kolb@hsc.utah.edu](mailto:Helga.Kolb@hsc.utah.edu)  
visit webvision  
[www.webvision.med.utah.edu](http://www.webvision.med.utah.edu)

On Oct 1, 2018, at 4:04 AM, Abbas Ommani <[a2ommani@uwaterloo.ca](mailto:a2ommani@uwaterloo.ca)> wrote:

Dear Dr. Helga Kolb,

I'm a PhD candidate at the School of Optometry and Vision Science, University of Waterloo. I'm in the process of preparing my dissertation and am seeking the permission to reproduce Figure 1.1 and Figure 2 of "WEBVISION" chapter: "Simple anatomy of the retina" from the following link:

<http://webvision.med.utah.edu/book/part-i-foundations/simple-anatomy-of-the-retina/>

A credit line acknowledging the original source will be included in my dissertation. If you need any further information to help process this request, then I would appreciate it if you could let me know.

Thank you very much for your consideration.

Best Regards  
Abbas Ommani

## 2. Copyright: Permission to use images

**From:** Karla Moeller <[Karla.Moeller@asu.edu](mailto:Karla.Moeller@asu.edu)>

**Sent:** Monday, October 1, 2018 4:16:23 PM

**To:** Abbas Ommani

**Subject:** Re: Form submission from: Permissions

Dear Abbas,

All of our materials are licensed under CC-BY-NC-SA, a "share-alike" license. This means that you are free to use our image in your dissertation, with proper attribution, as I assume that you are not intending to sell your dissertation for profit.

Keep in mind though, if you should ever publish your dissertation as a book, which some researchers do, you would not be able to use the image. Additionally, if you publish the chapter in which the image appears, it would need to be in an open access journal so the resource is not locked behind a paywall. In each of these cases, if the publication was profiting someone, you would either need to find another image or would have to make other arrangements with us for use of the image in those situations.

Hopefully the available version is of a high enough resolution for your dissertation, but let me know if you need a higher res version.

And good luck with your dissertation!

All the best,

Karla

\*\*\*

Karla Moeller, PhD

[about.me/karla.moeller](http://about.me/karla.moeller)

Educational Outreach Executive Coordinator

Office of the University Provost

Arizona State University



**From:** [solsvl@asu.edu](mailto:solsvl@asu.edu) <[solsvl@asu.edu](mailto:solsvl@asu.edu)> on behalf of Abbas via Ask A Biologist  
<[solsvl@asu.edu](mailto:solsvl@asu.edu)>

**Sent:** Sunday, September 30, 2018 8:55:09 PM

**To:** Karla Moeller

**Subject:** Form submission from: Permissions

Submitted on Sunday, September 30, 2018 - 8:55pm

Submitted by anonymous user: (unknown)

Submitted values are:

First name: Abbas

Last name: Ommani

Email: [a2ommani@uwaterloo.ca](mailto:a2ommani@uwaterloo.ca)

Retype email: [a2ommani@uwaterloo.ca](mailto:a2ommani@uwaterloo.ca)

Grade you teach: 13+

Institution: university of waterloo

Country : Canada

Yearly number of students/people this will impact? (Best guess): 100

What content will you be using? :

Reproduce an image (Retinal response vs wavelength of light) from the URL

[https://urldefense.proofpoint.com/v2/url?u=https-3A\\_\\_askabiologist.asu.edu\\_rods-2Dand-2Dcones&d=DwIFaQ&c=l45AxH-kUV29SRQusp9vYR0n1GycN4\\_2jInuKy6zbqQ&r=Zr3OMO8LEoc883-W0YVkcscGXU7lvpLhj6FgCR0pQdQ&m=EgOc1nTjdgTNTuTomQ71Zn4pIm6TYE4SBXbxfgKfk9o&s=avaHAXhGHjrtHsodPo36eMoSL5b\\_8G4uaL\\_w4xTB7wE&e=](https://urldefense.proofpoint.com/v2/url?u=https-3A__askabiologist.asu.edu_rods-2Dand-2Dcones&d=DwIFaQ&c=l45AxH-kUV29SRQusp9vYR0n1GycN4_2jInuKy6zbqQ&r=Zr3OMO8LEoc883-W0YVkcscGXU7lvpLhj6FgCR0pQdQ&m=EgOc1nTjdgTNTuTomQ71Zn4pIm6TYE4SBXbxfgKfk9o&s=avaHAXhGHjrtHsodPo36eMoSL5b_8G4uaL_w4xTB7wE&e=)

Please describe how you will be using the materials:

I'm in the process of preparing my dissertation and am seeking permission to include an image (Retinal response vs wavelength of light ). A credit line acknowledging the original source will be included in my dissertation. Thank you very much for your consideration.

### 3. Copyright: Permission to use images

#### Permission to Publish and Use COMSOL Multiphysics Images

Bernt Nilsson  
Senior VP of Marketing  
COMSOL, Inc.  
100 District Avenue  
Burlington, MA 01803 USA  
Email: [phil@comsol.com](mailto:phil@comsol.com)  
Tel: +1 781-273-3322  
Fax: +1 781-273-6603

COMSOL hereby grants you permission to reproduce, publish and distribute the image listed in Exhibit A, in your **Academic Thesis Paper ("Paper")** as well as in subsequent editions of your Paper in all media of expression now known or later developed and in all foreign language translations, for distribution throughout the world subject to your compliance with the following terms and conditions:

1. You shall comply with COMSOL's Trademark Guidelines set forth at: <http://www.comsol.com/company/trademarks/>.
2. You insert the phrase "Image credit: COMSOL." underneath the image in the Paper.
3. You acknowledge that you are receiving the COMSOL Materials "As Is" without any representations or warranties of any kind including, but not limited to any implied warranties of merchantability, fitness for a particular purpose or non-infringement.

This permission shall last until you receive a written request from COMSOL to terminate this permission, except that no such termination shall operate to revoke permission granted with respect to instances in which the images and/or descriptions have already been placed in circulation. I understand and acknowledge the above requirements,

Signed: 

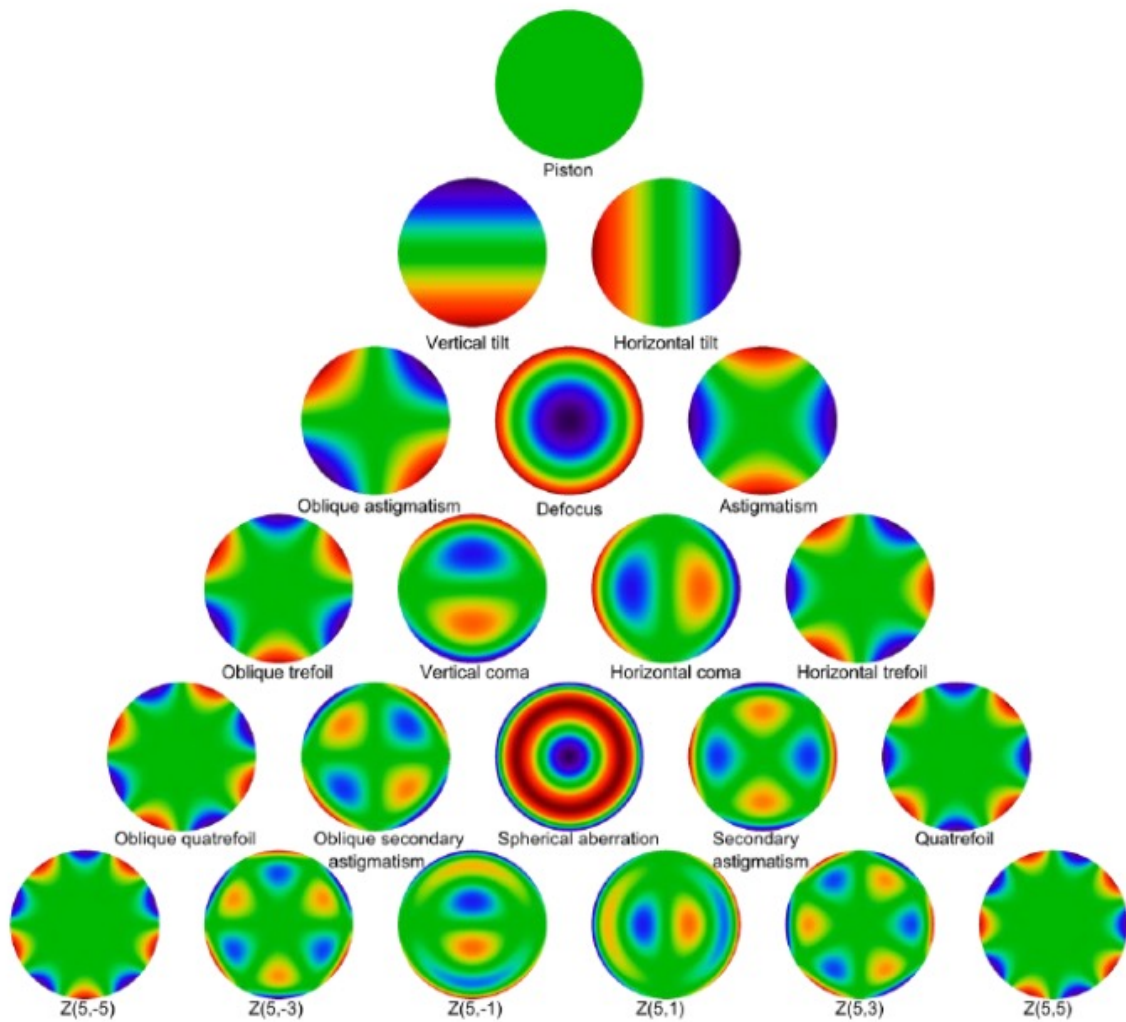
Name: Abbas Ommani

Date: 2018-11-05

Company/Institution: University of Waterloo

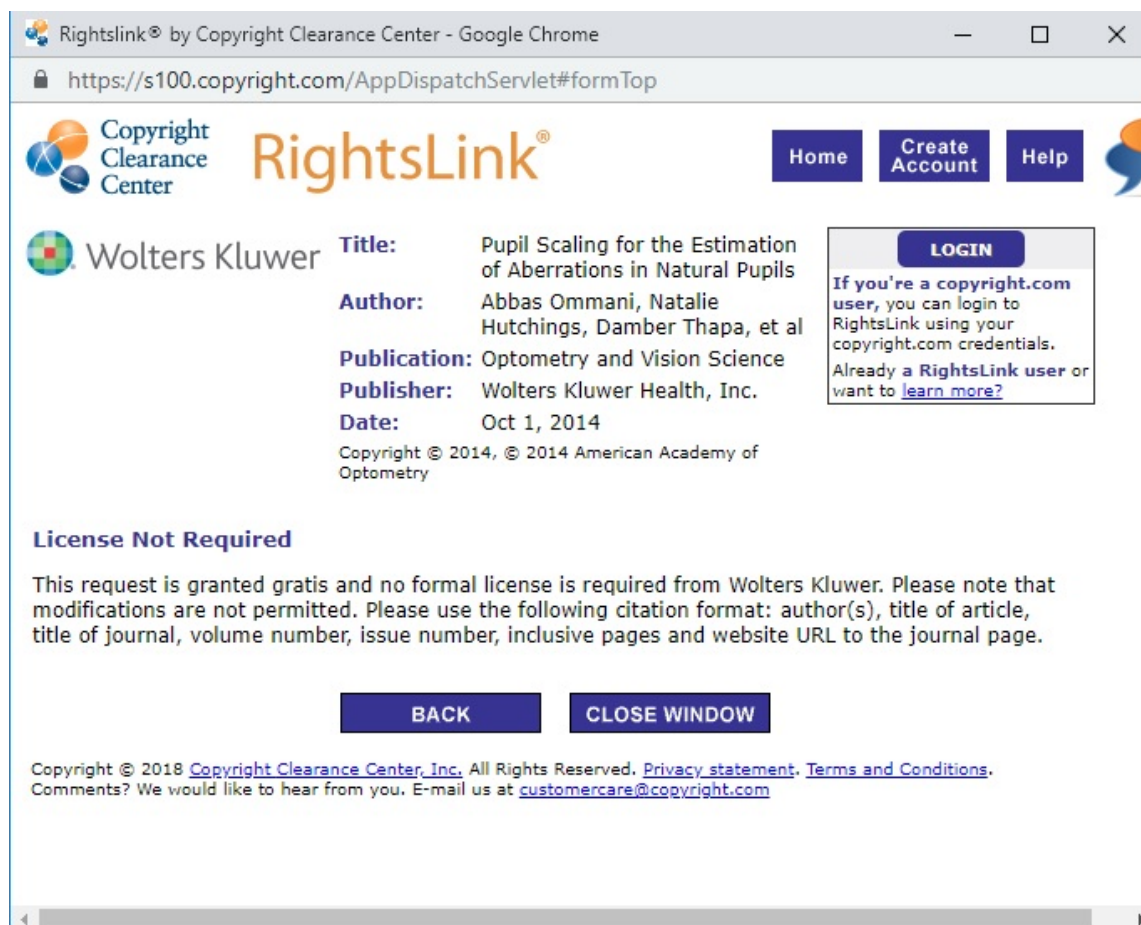
## SCHEDULE A

<https://www.comsol.com/release/5.2a/ray-optics-module>



*Zernike polynomials up to the fifth order, plotted on a unit circle.*

## 4. Copyright: Permission to reproduce the material



The screenshot shows a web browser window with the following content:

- Browser Title:** Rightslink® by Copyright Clearance Center - Google Chrome
- URL:** https://s100.copyright.com/AppDispatchServlet#formTop
- Page Header:** Copyright Clearance Center logo, RightsLink® logo, and navigation buttons: Home, Create Account, Help.
- Wolters Kluwer Logo:** A green and red logo.
- Article Information:**
  - Title:** Pupil Scaling for the Estimation of Aberrations in Natural Pupils
  - Author:** Abbas Ommani, Natalie Hutchings, Damber Thapa, et al
  - Publication:** Optometry and Vision Science
  - Publisher:** Wolters Kluwer Health, Inc.
  - Date:** Oct 1, 2014
- Copyright Notice:** Copyright © 2014, © 2014 American Academy of Optometry
- Login Box:** A box with a "LOGIN" button and text: "If you're a copyright.com user, you can login to RightsLink using your copyright.com credentials. Already a RightsLink user or want to [learn more?](#)"
- License Section:**
  - License Not Required**
  - Text:** This request is granted gratis and no formal license is required from Wolters Kluwer. Please note that modifications are not permitted. Please use the following citation format: author(s), title of article, title of journal, volume number, issue number, inclusive pages and website URL to the journal page.
- Buttons:** Two buttons labeled "BACK" and "CLOSE WINDOW".
- Footer:** Copyright © 2018 Copyright Clearance Center, Inc. All Rights Reserved. [Privacy statement](#). [Terms and Conditions](#). Comments? We would like to hear from you. E-mail us at [customercare@copyright.com](mailto:customercare@copyright.com)

## Bibliography

1. Barkana, Y., Gerber, Y., Elbaz, U., Schwartz, S., Ken-Dror, G., Avni, I., & Zadok, D. Central corneal thickness measurement with the Pentacam Scheimpflug system, optical low-coherence reflectometry pachymeter, and ultrasound pachymetry. *Journal of Cataract & Refractive Surgery*, 2005, 31(9), 1729-1735.
2. Atchison, D. A., Smith, G., & Smith, G. *Optics of the Human Eye*. Butterworth-Heinemann, 2000.
3. Edelhauser, H. F., & Ubels, J. L. The cornea and the sclera. *Adler's Physiology of the Eye: Clinical Applications*. 10th ed. Mosby, Inc.: 47- 114, 2003.
4. Dursun, D., Monroy, D., Knighton, R., Tervo, T., Vesaluoma, M., Carraway, K., ... & Pflugfelder, S. C. The effects of experimental tear film removal on corneal surface regularity and barrier function. *Ophthalmology*, 2000, 107(9), 1754-1760.
5. Montés-Micó, R., Alió, J. L., & Charman, W. N. Dynamic changes in the tear film in dry eyes. *Investigative Ophthalmology & Visual Science*, 2005, 46(5), 1615-1619.
6. Barbero, S. Refractive power of a multilayer rotationally symmetric model of the human cornea and tear film. *Journal of the Optical Society of America A*, 2006, 23(7), 1578-1585.
7. Charman, W. N. Optics of the human eye. *Visual optics and instrumentation*, 1991, 1, 1-26
8. Bennett, A. G., & Rabbetts, R. B. *Bennett and Rabbetts' Clinical Visual Optics*. Elsevier Health Sciences, 1998.
9. Thal, E., Miller, K., Rosenthal, P., Schechter, R., Steiner, R., & Beardsley, T. Optics, Refraction and Contact Lenses; Basic and Clinical Science Course 1988–1999. *San Francisco, CA, American Academy of Ophthalmology*, 1999.
10. Loewenfeld, I. E., & Lowenstein, O. *The Pupil: Anatomy, physiology, and clinical applications* (Vol. 2). Wiley-Blackwell, 1993.
11. Westheimer, G. Diffraction theory and visual hyperacuity. *American Journal of Optometry and Physiological Optics*, 1976, 53(7), 362-364.
12. Oculomotor Functions & Neurology CD-ROM, Indiana University School of Optometry, Chapter 16, [http://www.opt.indiana.edu/v665/CD/CD\\_Version/CH16/CH16.HTM](http://www.opt.indiana.edu/v665/CD/CD_Version/CH16/CH16.HTM), 2004, accessed May 6, 2018.
13. Atchison, D. A., Markwell, E. L., Kasthurirangan, S., Pope, J. M., Smith, G., & Swann, P. G. Age-related changes in optical and biometric characteristics of emmetropic eyes. *Journal of Vision*, 2008, 8(4), 29-29.

14. Chan, D. Y., Ennis, J. P., Pierscionek, B. K., & Smith, G. Determination and modeling of the 3-D gradient refractive indices in crystalline lenses. *Applied Optics*, 1988, 27(5), 926-931
15. Jones, C. E., Atchison, D. A., Meder, R., & Pope, J. M. Refractive index distribution and optical properties of the isolated human lens measured using magnetic resonance imaging (MRI). *Vision Research*, 2005, 45(18), 2352-2366.
16. Kasthurirangan, S., Markwell, E. L., Atchison, D. A., & Pope, J. M. In vivo study of changes in refractive index distribution in the human crystalline lens with age and accommodation. *Investigative Ophthalmology & Visual Science*, 2008, 49(6), 2531-2540.
17. Vilupuru, A. S., Roorda, A., & Glasser, A. Spatially variant changes in lens power during ocular accommodation in a rhesus monkey eye. *Journal of Vision*, 2004, 4(4), 6-6.
18. Roorda, A., & Williams, D. R. Optical fiber properties of individual human cones. *Journal of Vision*, 2002, 2(5), 4-4.
19. Glasser, A., & Campbell, M. C. Presbyopia and the optical changes in the human crystalline lens with age. *Vision Research*, 1998, 38(2), 209-229.
20. Helga Kolb, Simple anatomy of the retina, Webvision, <http://webvision.med.utah.edu/book/part-i-foundations/simple-anatomy-of-the-retina/>, Assessed on May 6, 2018
21. Hecht, S. Rods, cones, and the chemical basis of vision. *Physiological Reviews*, 1937, 17(2), 239-290.
22. Dr. Biology. "Rods and Cones". ASU - Ask A Biologist. 06 Jan 2010. ASU - Ask A Biologist, Web. 21 Sep 2018. <https://askabiologist.asu.edu/rods-and-cones>
23. H. Gross (Eds.). Handbook of Optical Systems. Wiley-VCH (2005).
24. Charman, W. N. Wavefront technology: past, present, and future. *Contact Lens and Anterior Eye*, 2005, 28(2), 75-92.
25. Parthasarathy, M. K., & Lakshminarayanan, V. A Brief History of Aberrometry Applications in Ophthalmology and Vision Science. In *Advances in Optical Science and Engineering*. Springer, Singapore, 2017, 31-39.
26. Thapa, D., Fleck, A., Lakshminarayanan, V., & Bobier, W. R. Ocular wavefront aberration and refractive error in pre-school children. *Journal of Modern Optics*, 2011, 58(19-20), 1681-1689.
27. Campbell, F. W., & Gubisch, R. W. Optical quality of the human eye. *The Journal of Physiology*, 1966, 186(3), 558-578.

28. Campbell, F. W., & Green, D. G. Optical and retinal factors affecting visual resolution. *The Journal of Physiology*, 1965, 181(3), 576-593.
29. Liang, J., & Williams, D. R. Aberrations and retinal image quality of the normal human eye. *Journal of the Optical Society of America A*, 1997, 14(11), 2873-2883.
30. Liang, J., Grimm, B., Goelz, S., & Bille, J. F. Objective measurement of wave aberrations of the human eye with the use of a Hartmann–Shack wave-front sensor. *Journal of the Optical Society of America A.*, 1994, 11(7), 1949-1957.
31. Cerviño, A., Hosking, S. L., Montes-Mico, R., & Bates, K. Clinical ocular wavefront analyzers. *Journal of Refractive Surgery*, 2007, 23(6), 603-616.
32. Thibos, L. N., & Hong, X. Clinical applications of the Shack-Hartmann aberrometer. *Optometry and Vision Science*, 1999, 76(12), 817-825.
33. Lakshminarayanan, V., & Fleck, A. Zernike polynomials: a guide. *Journal of Modern Optics*, 2011, 58(7), 545-561.
34. International Organization for Standardization (ISO), Ophthalmic optics and instruments- Reporting aberrations of the human eye. Geneva, Switzerland, ISO, 2008 (ISO 24157:2008).
35. P.Y. Maeda. Zernike polynomials and their use in describing the wavefront aberrations of the human eye.; Stanford University. 2003. Available at <ftp://bioeng118.bioeng.auckland.ac.nz/jtur044/references/introductory/zernike-wavefront-aberrations.pdf>. Accessed on October 2, 2017.
36. COMSOL. Ray optics module. Available at <https://www.comsol.com/release/5.2a/ray-optics-module>, accessed on October 2, 2017.
37. Diaz-Santana, L., Guériaux, V., Arden, G., & Gruppeta, S. New methodology to measure the dynamics of ocular wavefront aberrations during small amplitude changes of accommodation. *Optics Express*, 2007, 15(9), 5649-5663.
38. Diaz-Santana, L., Walker, G., & Bará, S. X. Sampling geometries for ocular aberrometry: A model for evaluation of performance. *Optics Express*, 2005, 13(22), 8801-8818.
39. Code of Federal Regulations Title 21 Food and Drugs Part 1040 Performance Standards for Light-Emitting Products Section 1040.10 Laser Products (US 21 CFR 1040.10), revised April 1, 2012.
40. American National Standards Institute, American National Standard for the Safe Use of Lasers: ANSI Z136.1-2014.

41. Davies, N., Diaz-Santana, L., & Lara-Saucedo, D. Repeatability of ocular wavefront measurement. *Optometry and Vision Science*, 2003, 80(2), 142-150.
42. Valdivieso-González, L. G., Zavaleta, G. R., Olazagasti, E. L., Balderas-Mata, S. E., & Rodríguez, E. T. (2014, August). Construction and validation of a Shack-Hartmann type aberrometer. In *Second International Conference on Applications of Optics and Photonics*. SPIE: International Society for Optics and Photonics, 9286, 92861S (2014).
43. Thibos, L. N., & Horner, D. Power vector analysis of the optical outcome of refractive surgery. *Journal of Cataract & Refractive Surgery*, 2001, 27(1), 80-85.
44. Ocean Optics, Irradiance. Available at <https://oceanoptics.com/measurementtechnique/irradiance/>. Accessed on Feb 10, 2019.
45. Diaz-Santana, H. L. *Wavefront sensing in the human eye with a Shack-Hartmann sensor. 2000* (Doctoral dissertation, Ph.D. Thesis. London: Imperial College of Science Technology and Medicine).
46. Thatiparthi, C., Ommani, A., Burman, R., Thapa, D., Hutchings, N., & Lakshminarayanan, V. Comparison of performance of some common Hartmann-Shack centroid estimation methods. In *Ophthalmic Technologies XXVI*, International Society for Optics and Photonics, 2016, 9693, 969321.
47. Xia, A. L., & Ma, C. W. An improved centroid detection method based on higher moment for Shack-Hartmann wavefront sensor. In *Optoelectronic Imaging and Multimedia Technology*. International Society for Optics and Photonics, 2010, 7850, 78501Q.
48. Baik, S. H., Park, S. K., Kim, C. J., & Cha, B. A center detection algorithm for Shack-Hartmann wavefront sensor. *Optics & Laser Technology*, 2007, 39(2), 262-267.
49. Ginis, H. S., Plainis, S., & Pallikaris, A. Variability of wavefront aberration measurements in small pupil sizes using a clinical Shack-Hartmann aberrometer. *BMC Ophthalmology*, 2004, 4(1), 1-8.
50. Campbell, C. E. Matrix method to find a new set of Zernike coefficients from an original set when the aperture radius is changed, *Journal of the Optical Society of America A.*, 2003, 20(2), 209-217.
51. Schwiegerling, J. Scaling Zernike expansion coefficients to different pupil sizes. *Journal of the Optical Society of America A.*, 2002, 19(10), 1937-1945.



52. Lundström, L., & Unsbo, P. Transformation of Zernike coefficients: scaled, translated, and rotated wavefronts with circular and elliptical pupils. *Journal of the Optical Society of America A.*, 2007, 24(3), 569-577.
53. Mahajan, V. N. Zernike coefficients of a scaled pupil. *Applied Optics*, 2010, 49(28), 5374-5377.
54. Dai, G. M. Scaling Zernike expansion coefficients to smaller pupil sizes: a simpler formula, *Journal of the Optical Society of America A.*, 2006, 23(3), 539-543.
55. Janssen, A. J., & Dirksen, P. Concise formula for the Zernike coefficients of scaled pupils. *Journal of Micro/Nanolithography, MEMS, and MOEMS*, 2006, 5(3), 030501.
56. Bara, S., Arines, J., Ares, J., & Prado, P. Direct transformation of Zernike eye aberration coefficients between scaled, rotated, and/or displaced pupils. *Journal of the Optical Society of America A.*, 2006, 23(9), 2061-2066.
57. Comastri, S. A., Perez, L. I., Pérez, G. D., Martin, G., & Bastida, K. Zernike expansion coefficients: rescaling and decentring for different pupils and evaluation of corneal aberrations. *Journal of Optics A: Pure and Applied Optics*, 2007, 9(3), 209.
58. Díaz, J. A., Fernández-Dorado, J., Pizarro, C., & Arasa, J. Zernike coefficients for concentric, circular scaled pupils: an equivalent expression. *Journal of Modern Optics*, 2009, 56(1), 131-137.
59. Hartwig, A., & Atchison, D. A. Analysis of higher-order aberrations in a large clinical population. *Investigative Ophthalmology & Visual Science*, 2012, 53(12), 7862-7870.
60. Hartwig, A., Atchison, D. A., & Radhakrishnan, H. Higher-order aberrations and anisometropia. *Current Eye Research*, 2013, 38(1), 215-219.
61. Ommani, A., Hutchings, N., Thapa, D., & Lakshminarayanan, V. Pupil scaling for the estimation of aberrations in natural pupils. *Optometry and Vision Science*, 2014, 91(10), 1175-1182.
62. A language and environment for statistical computing. R. foundation for Statistical Computing (R version 3.0.2) 2013. Available at: <http://www.r-project.org/>. Accessed February 15, 2013.
63. ming Dai, G. Validity of scaling Zernike coefficients to a larger diameter for refractive surgery. *Journal of Refractive Surgery*, 2011, 27(11), 837-841.
64. Neal, D. R., Baer, C. D., & Topa, D. M. Errors in Zernike transformations and non-modal reconstruction methods. *Journal of Refractive Surgery*, 2005, 21(5), S558-S562.

65. Bará, S., Pailos, E., Arines, J., López-Gil, N., & Thibos, L. Estimating the eye aberration coefficients in resized pupils: is it better to refit or to rescale?. *Journal of the Optical Society of America A.*, 2014, 31(1), 114-123.
66. Carkeet, A., Velaedan, S., Tan, Y. K., Lee, D. Y. J., & Tan, D. T. Higher order ocular aberrations after cycloplegic and non-cycloplegic pupil dilation. *Journal of Refractive Surgery*, 2003, 19(3), 316-322.
67. Seifert, L., Tiziani, H. J., & Osten, W. Wavefront reconstruction with the adaptive Shack–Hartmann sensor. *Optics Communications*, 2005, 245(1-6), 255-269.
68. Llorente, L., Marcos, S., Dorronsoro, C., & Burns, S. A. Effect of sampling on real ocular aberration measurements. *Journal of the Optical Society of America A.*, 2007, 24(9), 2783-2796.
69. Burman, R., Ommani, A., Thapa, D., Raahemifar, K., Hutchings, N., & Lakshminarayanan, V. A Method for Estimating the Wavefront Aberrations with Missing Spot Data in a Hartmann-Shack Aberrometer. In *Advances in Optical Science and Engineering*, 2015, 319-325). Springer, New Delhi.
70. Kuroda, T., Fujikado, T., Maeda, N., Oshika, T., Hirohara, Y., & Mihashi, T. Wavefront analysis in eyes with nuclear or cortical cataract. *American Journal of Ophthalmology*, 2002, 134(1), 1-9.
71. Maeda, N. Clinical applications of wavefront aberrometry—a review. *Clinical & Experimental Ophthalmology*, 2009, 37(1), 118-129.
72. Montés-Micó, R., Cáliz, A., & Alió, J. L. Wavefront analysis of higher order aberrations in dry eye patients. *Journal of Refractive Surgery*, 2004, 20(3), 243-247.
73. Wei, R. H., Lim, L., Chan, W. K., & Tan, D. T. Higher order ocular aberrations in eyes with myopia in a Chinese population. *Journal of Refractive Surgery*, 2006, 22(7), 695-702.
74. Carkeet, A., Luo, H. D., Tong, L., Saw, S. M., & Tan, D. T. Refractive error and monochromatic aberrations in Singaporean children. *Vision Research*, 2002, 42(14), 1809-1824.
75. Zadok, D., Levy, Y., Segal, O., Barkana, Y., Morad, Y., & Avni, I. Ocular higher-order aberrations in myopia and skiascopic wavefront repeatability. *Journal of Cataract & Refractive Surgery*, 2005, 31(6), 1128-1132.

76. Kim, M., Lee, Y. G., Seo, K. R., Kim, E. K., & Lee, H. K. Comparison of higher-order aberrations between eyes with natural supervision and highly myopic eyes in Koreans. *Korean Journal of Ophthalmology*, 2007, 21(2), 79-84.
77. Bennett, J. R., Stalboerger, G. M., Hodge, D. O., & Schornack, M. M. Comparison of refractive assessment by wavefront aberrometry, autorefraction, and subjective refraction. *Journal of Optometry*, 8(2), 109-115 (2015).
78. Barraquer, R. I., Cortés, L. P., Allende, M. J., Montenegro, G. A., Ivankovic, B., D'Antin, J. C., Martinez Osario, H., & Michael, R. Validation of the nuclear cataract grading system BCN 10. *Ophthalmic Research*, 2017, 57(4), 247-251.